



AFRL-RQ-WP-TR-2014-0051

ENERGY-BASED DESIGN OF RECONFIGURABLE MICRO AIR VEHICLE (MAV) FLIGHT STRUCTURES

James J. Joo and Gregory W. Reich

**Design and Analysis Branch
Aerospace Vehicles Division**

Richard V. Beblo

University of Dayton Research Institute

FEBRUARY 2014

Final Report

Approved for public release; distribution unlimited

**AIR FORCE RESEARCH LABORATORY
AEROSPACE SYSTEMS DIRECTORATE
WRIGHT-PATTERSON AIR FORCE BASE, OH 45433-7542
AIR FORCE MATERIEL COMMAND
UNITED STATES AIR FORCE**

NOTICE AND SIGNATURE PAGE

Using Government drawings, specifications, or other data included in this document for any purpose other than Government procurement does not in any way obligate the U.S. Government. The fact that the Government formulated or supplied the drawings, specifications, or other data does not license the holder or any other person or corporation; or convey any rights or permission to manufacture, use, or sell any patented invention that may relate to them.

This report was cleared for public release by the USAF 88th Air Base Wing (88 ABW) Public Affairs Office (PAO) and is available to the general public, including foreign nationals.

Copies may be obtained from the Defense Technical Information Center (DTIC)
(<http://www.dtic.mil>).

AFRL-RQ-WP-TR-2014-0051 HAS BEEN REVIEWED AND IS APPROVED FOR
PUBLICATION IN ACCORDANCE WITH ASSIGNED DISTRIBUTION STATEMENT.

*//Signature//

JAMES J. JOO, Engineer
Design and Analysis Branch
Aerospace Vehicles Division

//Signature//

THOMAS C. CO, Branch Chief
Design and Analysis Branch
Aerospace Vehicles Division

//Signature//

FRANK WITZEMAN, Chief
Aerospace Vehicles Division
Aerospace Systems Directorate

This report is published in the interest of scientific and technical information exchange, and its publication does not constitute the Government's approval or disapproval of its ideas or findings.

*Disseminated copies will show “//Signature//” stamped or typed above the signature blocks.

REPORT DOCUMENTATION PAGE					Form Approved OMB No. 0704-0188	
<p>The public reporting burden for this collection of information is estimated to average 1 hour per response, including the time for reviewing instructions, searching existing data sources, gathering and maintaining the data needed, and completing and reviewing the collection of information. Send comments regarding this burden estimate or any other aspect of this collection of information, including suggestions for reducing this burden, to Department of Defense, Washington Headquarters Services, Directorate for Information Operations and Reports (0704-0188), 1215 Jefferson Davis Highway, Suite 1204, Arlington, VA 22202-4302. Respondents should be aware that notwithstanding any other provision of law, no person shall be subject to any penalty for failing to comply with a collection of information if it does not display a currently valid OMB control number. PLEASE DO NOT RETURN YOUR FORM TO THE ABOVE ADDRESS.</p>						
1. REPORT DATE (DD-MM-YY) February 2014		2. REPORT TYPE Final		3. DATES COVERED (From - To) 01 October 2010 – 30 September 2013		
4. TITLE AND SUBTITLE ENERGY-BASED DESIGN OF RECONFIGURABLE MICRO AIR VEHICLE (MAV) FLIGHT STRUCTURES				5a. CONTRACT NUMBER In-house		
				5b. GRANT NUMBER		
				5c. PROGRAM ELEMENT NUMBER 61102F		
6. AUTHOR(S) James J. Joo and Gregory W. Reich (AFRL/RQVC) Richard V. Beblo (University of Dayton Research Institute)				5d. PROJECT NUMBER 3002		
				5e. TASK NUMBER N/A		
				5f. WORK UNIT NUMBER Q0CU		
7. PERFORMING ORGANIZATION NAME(S) AND ADDRESS(ES) Design and Analysis Branch (AFRL/RQVC) Aerospace Vehicles Division Air Force Research Laboratory, Aerospace Systems Directorate Wright-Patterson Air Force Base, OH 45433-7542 Air Force Materiel Command, United States Air Force				8. PERFORMING ORGANIZATION REPORT NUMBER AFRL-RQ-WP-TR-2014-0051		
9. SPONSORING/MONITORING AGENCY NAME(S) AND ADDRESS(ES) Air Force Research Laboratory Aerospace Systems Directorate Wright-Patterson Air Force Base, OH 45433-7542 Air Force Materiel Command United States Air Force				10. SPONSORING/MONITORING AGENCY ACRONYM(S) AFRL/RQVC		
				11. SPONSORING/MONITORING AGENCY REPORT NUMBER(S) AFRL-RQ-WP-TR-2014-0051		
12. DISTRIBUTION/AVAILABILITY STATEMENT Approved for public release; distribution unlimited.						
13. SUPPLEMENTARY NOTES PA Case Number: 88ABW-2014-0632; Clearance Date: 20 Feb 2014.						
14. ABSTRACT The objective of the project is to understand how to mechanize multi-jointed MAV wings for perching and/or flapping applications and develop an energy-based design framework for the solution of combined multi-physics, multi-objective problems.						
15. SUBJECT TERMS MAV						
16. SECURITY CLASSIFICATION OF:			17. LIMITATION OF ABSTRACT: SAR	18. NUMBER OF PAGES 102	19a. NAME OF RESPONSIBLE PERSON (Monitor) James J. Joo	
a. REPORT Unclassified	b. ABSTRACT Unclassified	c. THIS PAGE Unclassified			19b. TELEPHONE NUMBER (Include Area Code) N/A	

TABLE OF CONTENTS

<u>Content</u>	<u>Page</u>
List of Figures	ii
List of Tables	iv
Preface	v
Section 1. Introduction	1
1.1 Morphing	1
1.2 Optimization	4
1.3 Problem Description	5
Section 2. Methodology	7
2.1 Geometry Setup	7
2.2 Finite Element Model	12
2.2.1 Step 1: Discretization	13
2.2.2 Element Stiffness Matrix	13
2.2.3 Global Stiffness Matrix	26
2.2.4 Displacement Solution	27
2.2.5 Element Stresses	28
2.3 Aerodynamics	29
2.3.1 Perching Maneuvers	29
2.3.2 Force Estimation	32
2.4 Optimization	35
2.4.1 Compliance Objective Using the SIMP Model	35
2.4.2 Optimality Criteria Method	40
2.5 Substructure and Actuation Optimization	42
2.5.1 Elements	43
2.5.2 Element Formulation	44
2.5.3 Vortex Lattice Method by Ring Vortex Elements/Aeroelastic Effects	49
2.5.4 Optimization Background	51
2.5.5 Problem Formulation	57
2.5.6 Sensitivity Analysis	59
Section 3. Results	61
3.1 Aerodynamic Results	61
3.2 Optimized Static Structural Layouts	67
3.3 Grid Independence	82
3.4 Optimized Actuation System	83
Section 4. Conclusions	85
4.1 Summary	85
4.2 Recommendations	86
4.3 Future Work	87
List of Acronyms, Abbreviations, and Symbols	88
Section 5. Bibliography	89

LIST OF FIGURES

<u>Figure</u>	<u>Page</u>
Figure 1: Eagle Owl Soaring [2]	1
Figure 2: Eagle Owl Flyby [3]	2
Figure 3: Eagle Owl Perching [4]	2
Figure 4: Comparison of Fixed-Wing and Morphing Performances [5].....	3
Figure 5: Lockheed-Martin's Z-Wing [6]	4
Figure 6: NextGen's Batwing [6].....	4
Figure 7: Generalized Topology Design Problem	5
Figure 8: Geometry Layout for Three Section Wing	7
Figure 9: Wing Geometry GUI	8
Figure 10: Example Wing Geometry	9
Figure 11: Birdwing in Forward Swept Configuration (m)	9
Figure 12: Birdwing in Zero Sweep Configuration (m).....	10
Figure 13: Birdwing in Back Swept Configuration (m).....	10
Figure 14: Birdwing in Dive Configuration (m)	11
Figure 15: General Quadrilateral Element Mapping to Computational Domain [13]	14
Figure 16: Mapping of General Quadrilateral Element to Computational Domain.....	19
Figure 17: Natural Coordinate Unit Vectors.....	25
Figure 18: Computational Domain Indexing Example	27
Figure 19: Computational Domain Indexing Example	28
Figure 20: Perching Maneuver: Altitude vs. Range.....	30
Figure 21: Perching Maneuver: Range vs. Time	30
Figure 22: Perching Maneuver: Attitude vs. Range.....	31
Figure 23: Perching Maneuver: Velocity vs. Range	31
Figure 24: Main Menu of Tornado Software	32
Figure 25: Example of Tornado Geometry Output [21]	33
Figure 26: Example of Tornado Vortex Panels Output [22].....	33
Figure 27: Viscous Drag Estimation Curve	34
Figure 28: SIMP Penalization of Element Thickness	38
Figure 29: Example "SIMP" Output.....	41
Figure 30: Example "SIMPm" Output with No Checkerboard Filter.....	42
Figure 31: Model Element Designation	43
Figure 32: Line Element Configurations	43
Figure 33: Joint Element Configurations	44
Figure 34: Typical Joint-Beam-Joint Model.....	46
Figure 35: Membrane Pre-Strain.....	49
Figure 36: C_p Distributions	50
Figure 37: Static Aeroelastic Analysis.....	51
Figure 38: C_p for Birdwing Geometries along Perching Trajectory	63
Figure 39: Force [N] for Birdwing in Swept Back Configuration at Point 1.....	64
Figure 40: Force [N] for Birdwing in Dive Configuration at Point 2	65

Figures

(List of Figures continued)

Page

Figure 41: Force [N] for Birdwing in Zero Sweep Configuration at Point 3.....	66
Figure 42: Force [N] for Birdwing in Forward Swept Configuration at Point 4	67
Figure 43: Membrane Structure for Birdwing at Point 1	68
Figure 44: Bending Structure for Birdwing at Point 1	69
Figure 45: Combined Structure for Birdwing at Point 1	70
Figure 46: Combined Structure for Birdwing at Point 1 without Viscous Drag.....	71
Figure 47: Membrane Structure for Birdwing at Point 2	72
Figure 48: Bending Structure for Birdwing at Point 2.....	73
Figure 49: Combined Structure for Birdwing at Point 2.....	74
Figure 50: Combined Structure for Birdwing at Point 2 without Viscous Drag.....	75
Figure 51: Membrane Structure for Birdwing at Point 3	76
Figure 52: Bending Structure for Birdwing at Point 3	77
Figure 53: Combined Structure for Birdwing at Point 3.....	78
Figure 54: Combined Structure for Birdwing at Point 3 without Viscous Drag.....	78
Figure 55: Membrane Structure for Birdwing at Point 4	79
Figure 56: Bending Structure for Birdwing at Point 4.....	80
Figure 57: Combined Structure for Birdwing at Point 4 without Viscous Drag.....	81
Figure 58: Combined Structure for Birdwing at Point 3 with Coarse Mesh.....	82
Figure 59: Convergence Data for Figure 58	83
Figure 60: Results without Membrane Elements	83
Figure 61: Results with Membrane Elements	84

LIST OF TABLES

<u>Table</u>	<u>Page</u>
Table 1: Sectioned Geometry for Multiple Configuration Birdwing	12
Table 2: Data for Selected Points along Perching Maneuver	32
Table 3: Aerodynamic Data for Birdwing along Perching Trajectory	61

PREFACE

A topology optimization model for conceptual wing structure layouts of morphing micro air vehicles (MAVs) has been developed and implemented in MATLAB. Specifically, a 6 degree-of-freedom (DOF) finite element (FE) model with a general quadrilateral discretization scheme was created by superposition of a known simple linear plane membrane element and a Kirchhoff plate bending element derived herein. The purpose of the six degree-of-freedom model was to accommodate in-plane and out-of-plane aerodynamic loading combinations. The FE model was validated and the MATLAB implementation was verified with classical beam and plate solutions. A compliance minimization optimization objective was then formulated with the Solid Isotropic Material with Penalization (SIMP) method, subject to the equilibrium constraint computed by the FE model, and solved with the Optimality Criteria (OC) method. With the topology optimization model in place, four aerodynamic loading scenarios were extracted from points along a feasible MAV perching flight trajectory and used to determine wing thickness distributions for given planform shapes. The results suggest conceptual structural layouts in morphing MAVs, but equally important, the simple MATLAB implementation of the model can be adapted for a variety of objective statements for MAV morphing wing design.

Section 1. INTRODUCTION

1.1 Morphing

The ambiguous characterization of an aircraft as morphing could denote any one of sundry possible modifications to an aircraft's structure during flight; but a more recent goal in this venue seeks to characterize morphing aircraft as those that can significantly modify their wing shape to adapt to multiple mission roles, hence developing high-performance in dissimilar flight regimes.

In 2003, the Defense Advanced Research Projects Agency (DARPA) began the 2 1/2 year Morphing Aircraft Structures (MAS) program in conjunction with the Air Force Research Laboratory's (AFRL) Air Vehicles Directorate (now Aerospace Systems Directorate). The MAS program sought to design and build aircraft where, distinct from all of the historical morphing efforts of the past, morphing would entail radical, aerodynamically efficient shape change, thus transforming the mission of an aircraft. DARPA further elaborates that "the program envisions changing wing areas, wing spans, and other dimensions far more radically than before," where "radical" describes a change on the order of 50 percent. [1] Depending on the mission requirements, these efforts will likely convert military aircraft from large and heavy, piloted aircraft to relatively small, unmanned aerial vehicles (UAVs). That nature does in fact take advantage of drastic wing morphing through disparate flight maneuvers is piquantly and elegantly epitomized by the eagle owl in Figure 1 to Figure 3, in which the planform shapes are outlined.



Figure 1: Eagle Owl Soaring [2]

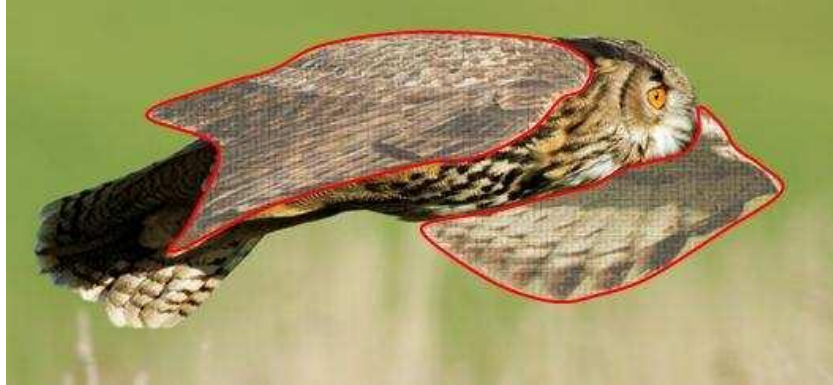


Figure 2: Eagle Owl Flyby [3]



Figure 3: Eagle Owl Perching [4]

Modifying drag is crucial as lessening drag is a priority for both long range endurance missions and high speed maneuvers, and accumulating drag is paramount for rapid deceleration of a vehicle to a landing of near zero velocity. But producing a change in either lift or drag should not be thought of as separate affairs; rather aerodynamic efficiency is influenced each time the lift-to-drag ratio is changed. The “best” velocity for a particular mission segment often depends directly on wing plan-form. An effective graphic juxtaposing conventional fixed geometry and morphing geometry is that of the spider plot shown in Figure 4. In the plot, the outermost radius of the plot is the best possible performance for a particular mission segment. On the legend, the “Firebee” represents the performance of a fixed-wing aircraft, the “airfoil” represents the same aircraft but with morphing airfoil capability, and the “geometry” series represents a study where wing area, wingspan, taper ratio, and sweep angle are free to vary independently of each other. Clearly, a wing capable of telescoping, chord extension, and variable sweep behooves a multi-role platform.

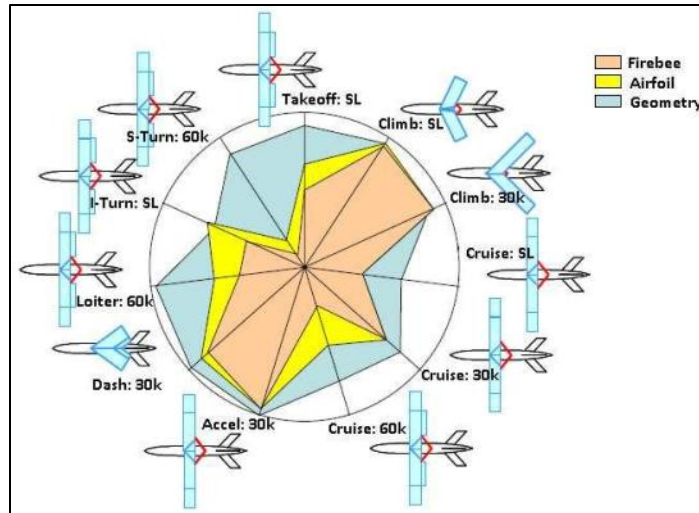


Figure 4: Comparison of Fixed-Wing and Morphing Performances [5]

Even a brief survey of aerodynamic dividends attainable by morphing aircraft promises a lucrative enterprise, but realizing morphing potential is a multifarious technical challenge. In an effort to resolve the many challenges, the first two phases of the MAS program sought to achieve four technical goals:

1. “Innovative, active wing structures that change shape;
2. Integration and aeronautical use of advanced sensors, skin and structure materials, internal mechanisms and distributed power sources;
3. Advanced capabilities for the military community;
4. Advanced shape-changing materials, efficient actuators and sophisticated, smart mechanisms.”

[6]

According to the MAS program manager Terrence Weisshaar, morphing aircraft wings would ideally have at least a 50 percent area change, thus reconciling the reconnaissance mission requirement of a wide wingspan and large wing area with the combat requirement of minimum wing area for speeds of Mach 2 and 3. As the MAS program entered Phase III, two contractor teams, Lockheed-Martin Advanced Development Programs and NextGen Aeronautics, sought to demonstrate the advantageousness of morphing by comparing performance in both morphed and unmorphed configurations for climbing and turning maneuvers. Lockheed-Martin developed a UAV, dubbed “Z-Wing” (Figure 5), with two-position wings that essentially fold and tuck up alongside the fuselage, in effect, hiding a large part of the planform. Lockheed’s 1/8 inch thick skin, fabricated by Shape Memory Polymer (SMP) technology, was capable of stretching 100 percent upon stimulation of a current passing through it.

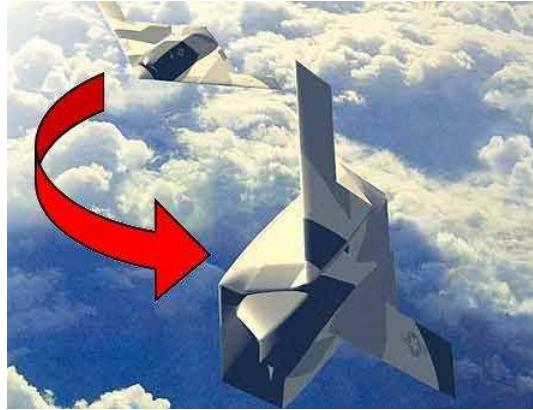


Figure 5: Lockheed-Martin's Z-Wing [6]

Unlike the three-dimensional morphing of the Lockheed UAV, NextGen's morphing concept, called "Batwing" (Figure 6), consisted of in-plane shape change. With the same flexible skin challenge, NextGen achieved a 40 percent area change, 30 percent span change, and 20° change in sweep while successfully test flying a remotely piloted vehicle called the MFX-1. In light of the technical competencies hoped to be gleaned from the MAS program, progress with flexible skin, structural actuation, and suitable flight control technologies were realized.



Figure 6: NextGen's Batwing [6]

1.2 Optimization

As stated by the MAS program, the technical challenge of morphing wing design will involve the multidisciplinary integration of sensors, actuators, structures, mechanisms, and skins; a challenge far exceeding simple design of beams or four-bar linkages. Such a combinative problem is likely to have intricate solutions, not easily approachable on the basis of intuition alone. A promising design approach to a multifaceted problem is found in the character of optimization. Optimization allows a designer a direct way of stating any number of objectives—quantities to be minimized or maximized—and design variables—parameters that can assume a range of values throughout the optimization process. Then, once the designer has identified the underlying constraints (usually comprised of guiding engineering principles or simple geometric relationships), as well as governing bounds on the design variables (set by physical or other reasonable limitations), optimization solvers iterate through a set of equations numerous times until a stated objective converges within a change tolerance. With this manner of problem formulation and assuming the mechanics of a problem have been correctly formulated, a designer focuses his attention on identifying the most desirable objectives to meet. Optimization is not without its

difficulties, as challenges may lay in interpreting results or in the manufacturability of solutions, but it is certainly an advantageous tool to aid the morphing challenge.

Topology optimization seeks the optimal layout within a stated design domain (Figure 7). The prescribed quantities consist only of the loading and support conditions, the fraction of the design space to be filled with material, “volume fraction,” and any other desired design restrictions such as a requirement for a hole or to fill the boundary of the domain. The shape and connectivity are not prescribed and are determined from the optimization. The topology problem is called a distributed parameter system because the design variables represent a field or continuum with infinite degrees of freedom. Thus, formulating a calculable problem will require discretization of the field such that the field is comprised of a finite set of elements each with a finite number of DOF. The selected discretization scheme will influence the resulting structure, and hence incites the enterprise of obtaining a grid-independent solution.

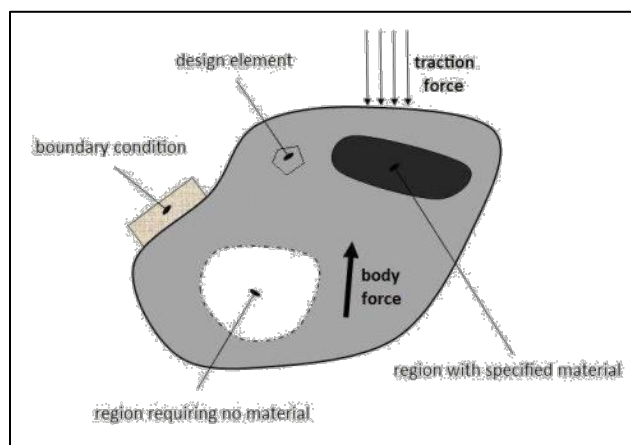


Figure 7: Generalized Topology Design Problem

Though a continuum requires discretization, the distributed parameter system is not to be confused with a discrete parameter system which results when a structural problem only has a finite number of design variables. Such problems describe naturally discrete systems (i.e., the sizing of truss cross-sectional areas). Topology optimization is capable of driving toward a discrete or a continuous solution depending on the formulation, and either solution may be worthy of consideration, depending on how the structure is to be constructed or manufactured. While the objective function may encourage a discrete or a continuous solution, it is chiefly seeking to minimize a particular quantity. What that quantity represents is perhaps even more germane to the structural layout than is the discretization scheme. Of the many objective functions that can be employed, a natural starting point is that of compliance minimization, which is equivalent to stiffness maximization. Because a topological approach to design is very general (i.e., determination of the quantity and/or layout of beams, trusses, membranes, actuators, springs, pivot locations, etc.) and because an optimization problem can be formulated by an assortment of objective statements (i.e., compliance, strain or potential energy, fundamental eigenvalue, buckling load, etc.), topology optimization is highly practicable to morphing aircraft structures.

1.3 Problem Description

In view of the many alluring morphing challenges, the structural layout of morphing MAV wings subjected to a gamut of aerodynamic loads as the MAV executes a perching maneuver will be

investigated. A perching maneuver is a common landing scheme of birds in which they dive below a landing location, exchange kinetic energy for potential energy while pulling up to the perch, and then come to an abrupt vertical landing on the perch. The perching maneuver stimulates much interest because it is a miniature of a multi-role mission, in which an aircraft leaves a reference condition, such as a loiter wing configuration, “tucks” its wings into a dive configuration, and then flares them back out both to quickly ascend and to collect momentum-reducing drag.

A few points along the perching trajectory will be extracted which are representative of the extremes of the maneuver. A three-dimensional estimation of the aerodynamic loads will be made and applied to the morphing wing shapes. By constructing a compliance optimization, conceptual wing layouts of the structure will be investigated for the dissimilar load cases. A computational tool which will provide insight into the design mechanization of morphing aircraft structures focusing on minimizing the energy required to achieve the desired shape change was also developed. Unlike conventional aircraft design methodologies which aim to minimize the compliance of structures, this approach will leverage the aeroelastic effects on structures to adapt the configurations in an effort to minimize actuator utilization. Recent investigations have been separately conducted for mechanism design, topology and structural optimization, actuator placement, and energy efficiency. This effort aims to combine these disciplines to produce a tool for efficient integrations of actuators, mechanisms, and elastic structures for the design of morphing aircraft.

Section 2. METHODOLOGY

This chapter details the theoretical methodology leading to the development of the MATLAB codes used to predict the results of Section 1. The initial task was to establish a geometry generation method, and select a few baseline geometries. Next the development and derivation of the finite element models needed to solve the equilibrium constraint in the optimization is described. A perching trajectory with corresponding flight data is then chosen, and the process for estimating the resulting aerodynamic loads to be applied to the FE model is related. The compliance minimization objective using the SIMP model is formulated, and the OC method used to solve the optimization problem is described. Finally, the optimization methods used to prescribe the optimum placement and type of actuators required for various shape changes is presented.

2.1 Geometry Setup

The scope of the current investigation is limited to planform-changing, two-dimensional morphing, akin to NextGen's Batwing. In order to use simple bilinear shape functions to describe the geometry of the finite elements, planform shapes are framed by straight lines. Additionally, the wing is comprised of any number of trapezoidal sections. This restriction ensures that the leading and trailing edges have the same number of straight-edged line segments, and that the tip chord is parallel to the root chord. It is feasible for any geometry that meets these criteria to be discretized by a structured mesh, though meeting the criteria does not guarantee that the geometry will be conducive to a structured mesh. For instance, a wing with a near-zero taper for its last section will have very small cells at the tip, which may lead to bad results in both the finite element analysis and the aerodynamic analysis.

Figure 8 displays a MATLAB generated; three-sectioned, general wing planform mesh in terms of the script's input variables. The code provides a graphical user interface (GUI) for easy creation of a wing in any number of configurations (Figure 9). More details of the generation and visualization of the mesh are presented by Elgersma [7].

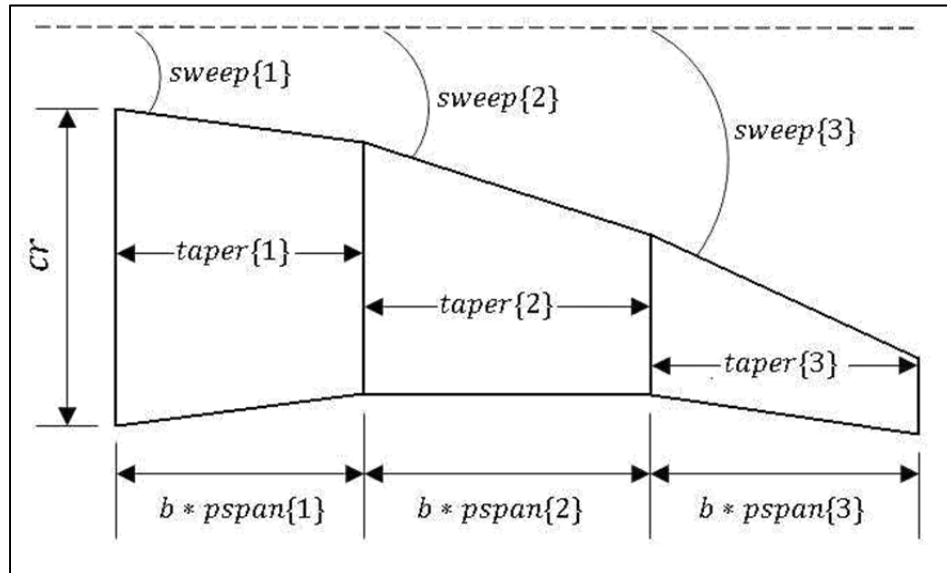


Figure 8: Geometry Layout for Three-Section Wing

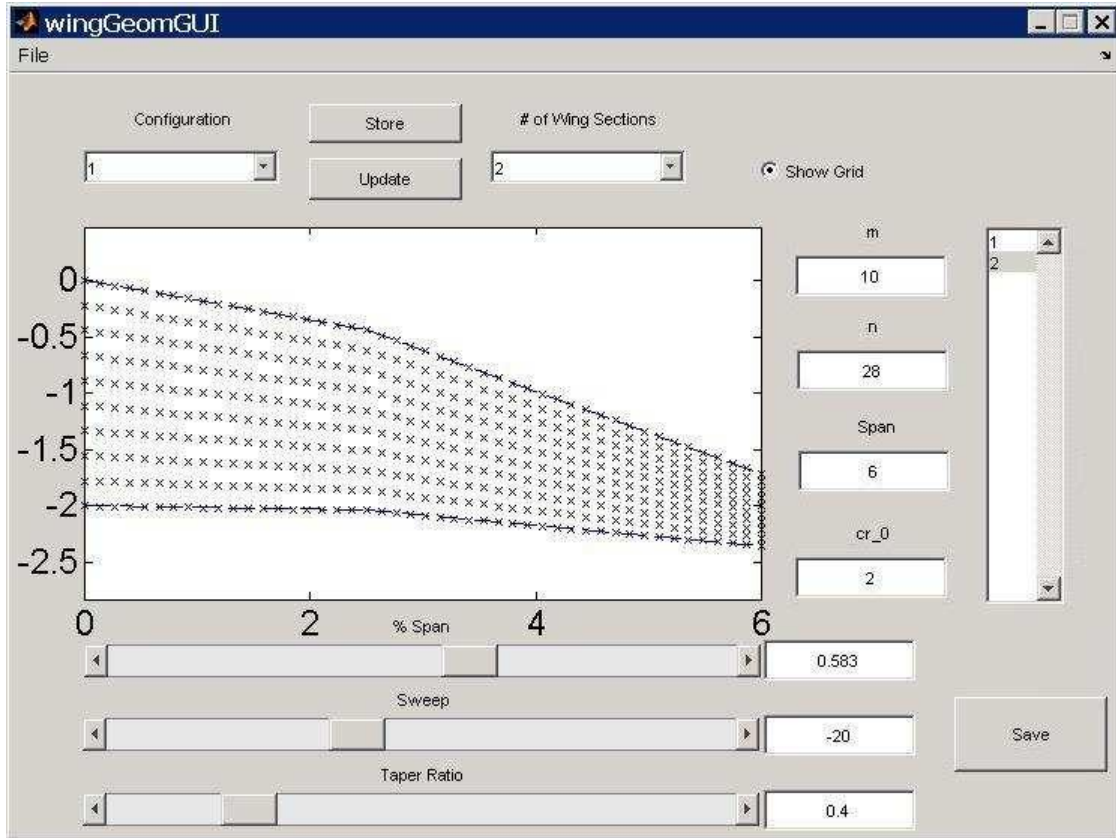


Figure 9: Wing Geometry GUI

For each wing configuration, the input variables define a root chord and span for the entire wing, and a taper ratio, sweep angle, and percent of the total span for each wing section. The mesh is created by linear interpolation in two directions with the number of grid points in both directions specified by the user. After initial development of the script, the upper profiles of a NACA 4-series airfoil and a reflexed airfoil were hardcoded into the script to add camber to otherwise flat wings. An example of a two-sectioned wing with camber generated by the GUI and is shown in Figure 10.

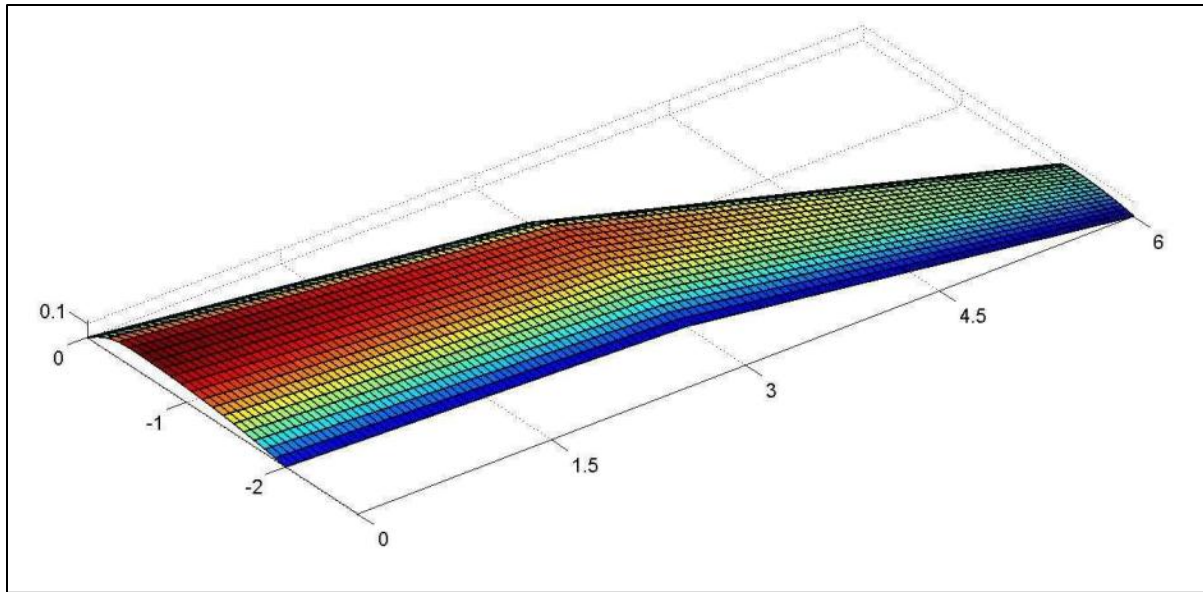


Figure 10: Example Wing Geometry

In order to capture similar planform configurations as the eagle owl (shown in Figure 1 through Figure 3) is capable of morphing through, a rotating mechanism is envisioned that can sweep about 5° forward during a flare, and then sweep back roughly 55° to 60° during a diving dash. The trapezoidal partitions and generated meshes for four configurations of this fictitious geometry (dubbed “birdwing”) are shown in Figure 11 through Figure 14. Table 1 gives the geometry parameters that define the wing configurations. In later analysis, simple rectangular wings with and without sweep are also used for baseline comparison to the birdwing.

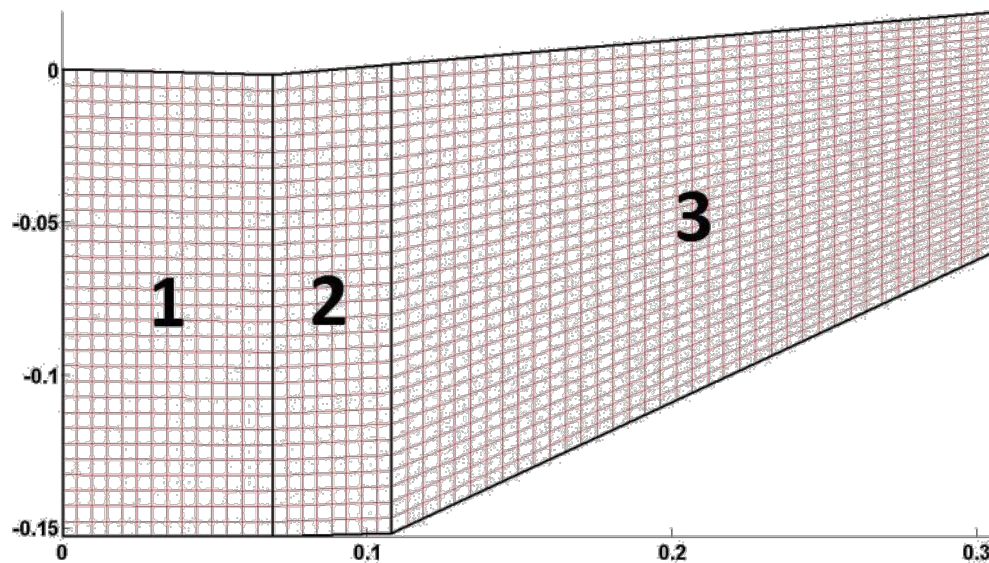


Figure 11: Birdwing in Forward Swept Configuration (m)

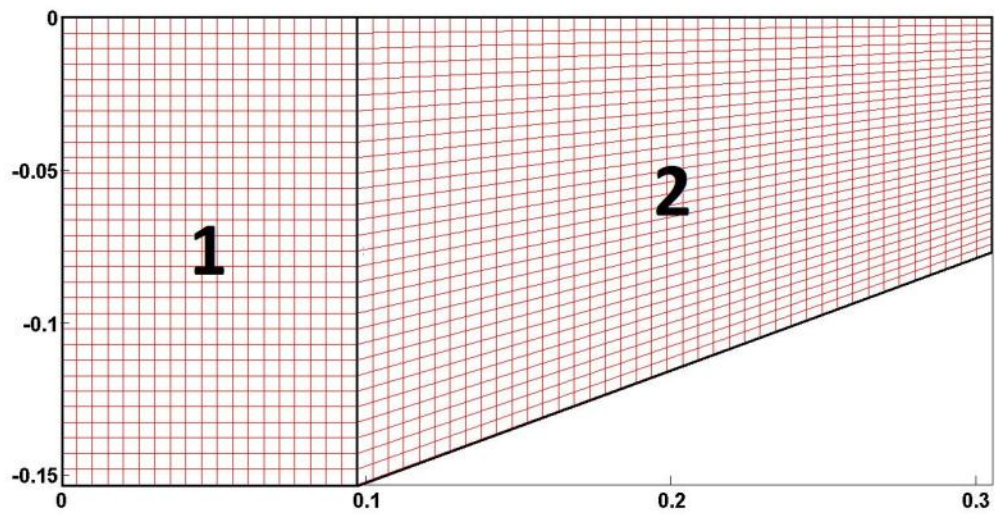


Figure 12: Birdwing in Zero Sweep Configuration (m)

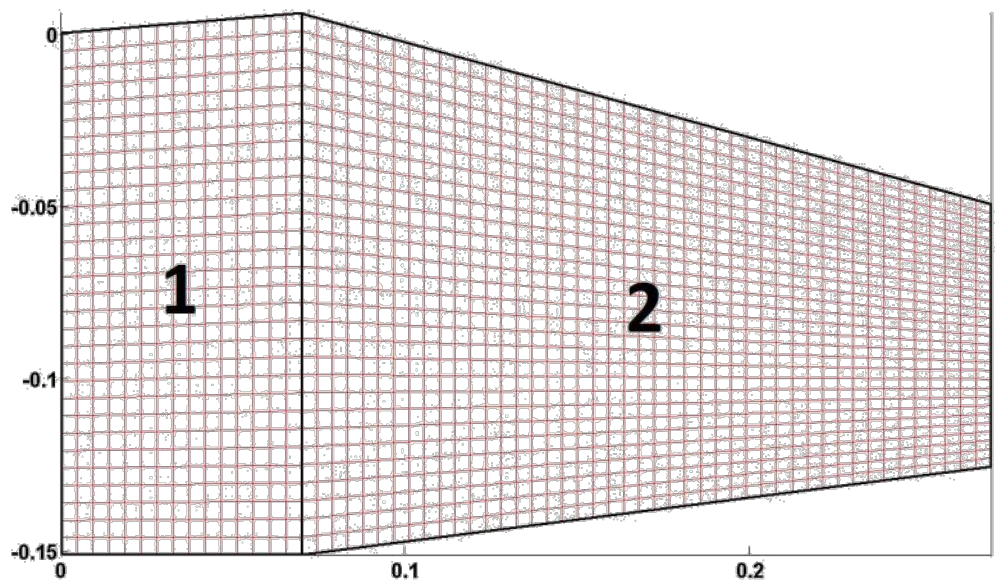


Figure 13: Birdwing in Back Swept Configuration (m)

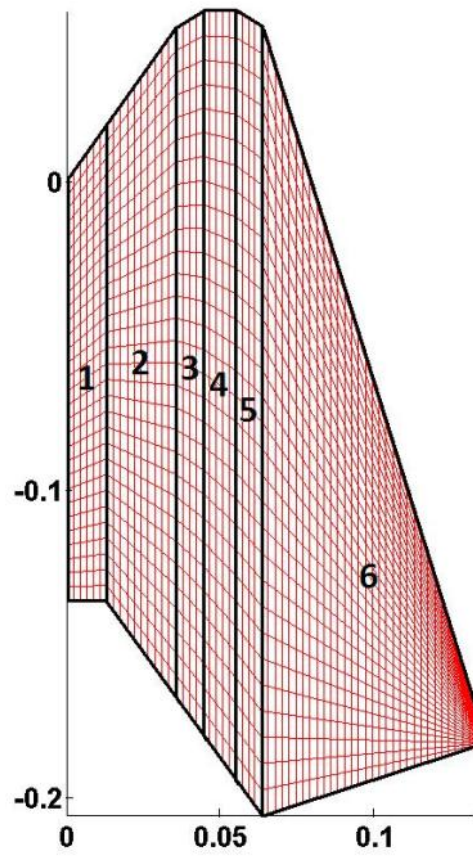


Figure 14: Birdwing in Dive Configuration (m)

Table 1: Sectioned Geometry for Multiple Configuration Birdwing

Configuration			5° Forward	0° Sweep	15° Back	Dive
Partition #1	Chord	m	0.153	0.153	0.151	0.136
	Span (%)	m	0.069 (22.6)	0.097 (31.8)	0.070 (25.9)	0.013 (9.7)
	Taper	—	0.988	1.000	1.040	1.135
	Sweep	°	-1.56	0	4.90	54.74
	QC Sweep*	°	-1.17	0	3.68	46.69
	Panels**	#	14	19	15	6
Partition #2	Chord	m	0.152	0.153	0.157	0.154
	Span (%)	m	0.039 (12.8)	0.208 (68.2)	0.200 (74.1)	0.023 (16.9)
	Taper	—	1.014	0.501	0.483	1.408
	Sweep	°	4.97	0	-15.50	54.74
	QC Sweep	°	4.19	5.24	-9.95	35.63
	Panels	#	8	41	45	10
Partition #3	Chord	m	0.154	—	—	0.217
	Span (%)	m	0.197 (64.6)	—	—	0.009 (6.7)
	Taper	—	0.510	—	—	1.081
	Sweep	°	4.97	—	—	30.89
	QC Sweep	°	10.35	—	—	5.97
	Panels	#	38	—	—	4
Partition #4	Chord	m	—	—	—	0.234
	Span (%)	m	—	—	—	0.011 (8.0)
	Taper	—	—	—	—	1.063
	Sweep	°	—	—	—	0
	QC Sweep	°	—	—	—	-18.99
	Panels	#	—	—	—	5
Partition #5	Chord	m	—	—	—	0.249
	Span (%)	m	—	—	—	0.008 (6.2)
	Taper	—	—	—	—	1.027
	Sweep	°	—	—	—	-30.35
	QC Sweep	°	—	—	—	-38.07
	Panels	#	—	—	—	4
Partition #6	Chord	m	—	—	—	0.256
	Span (%)	m	—	—	—	0.070 (52.5)
	Taper	—	—	—	—	0.040
	Sweep	°	—	—	—	-72.65
	QC Sweep	°	—	—	—	-66.73
	Panels	#	—	—	—	31
Total Span			0.305	0.305	0.270	0.133

*QC Sweep is the quarter-chord sweep

**Panels is the number of spanwise panels

2.2 Finite Element Model

Previous investigations by Joo et al. [8] [9] and Inoyama et al. [10] [11] [12] lacked out-of-plane loading capability in their finite element models. Therefore, the goal of this section is to develop a 6 DOF model that can support membrane (in-plane) and bending (out-of-plane) loads and be easily implemented in MATLAB. The approach undertaken is to first develop membrane (Section 2.2.2.1) and bending (Section 2.2.2.2) stiffness matrices independently, and then superimpose the 2 to form the full 6 DOF model

(Section 2.2.2.3). Section 2.2.2.3 also defines a transformation matrix so that non-planar geometries can be analyzed. After the element stiffness matrices are derived, the rest of the finite element method as it relates to the MATLAB coding process is described in Sections 2.2.3 through 2.2.5.

In the following sections, the finite element method will be broken down into the following eight general steps:

- Step 1:** Discretize the Geometry
- Step 2:** Select the Element Types
- Step 3:** Select a Displacement Function
- Step 4:** Define the Strain/Displacement and Stress/Strain (or Equivalent) Relations
- Step 5:** Derive the Element Stiffness Matrix
- Step 6:** Assemble the Global Stiffness Matrix
- Step 7:** Apply Boundary Conditions and Solve for the Unknown Degrees of Freedom
- Step 8:** Solve for the Element Stresses

While Steps 1 and 6–8 are largely the same for the different element types, a stiffness matrix must be developed for each element type in Steps 2 through 5 (Section 2.2.2).

2.2.1 Step 1: Discretization

Mentioned in the discussion of the geometry, the mesh type of choice is a structured arrangement of quadrilateral elements rather than an unstructured collocation of triangular elements, and is therefore easily created by two-dimensional linear interpolation. Another advantage of a structured mesh over an unstructured mesh is ease of coding. Each quadrilateral element has four definite neighboring cells and can be mapped to a rectangular computational domain, allowing a programmer to simply loop through the rows and columns of the mesh. The elements are ordered such that the upper left corner of the computational domain is the first element, and successive elements are then counted down through the rows and then right through the columns (see Figure 18). Using general quadrilaterals rather than rectangular elements allows a complex geometry to be fitted with a structured mesh. However, the disadvantage is that cells can be skewed and are more likely to have large aspect ratios, which typically increases the inaccuracy of the solution. The bird wing in the dive configuration (Figure 14) demonstrates this point precisely, where highly skewed cells dominate the sixth wing section and aspect ratio grows large as the section tapers nearly to a point.

2.2.2 Element Stiffness Matrix

2.2.2.1 Quadrilateral Membrane Element

This derivation follows the nomenclature and methods of Reference [13].

Step 2: Select the Element Type

The general quadrilateral membrane element considered here stretches in two directions and thus has 2 DOF for each of its 4 nodes.

$$\{d\} = \begin{Bmatrix} d_1 \\ d_2 \\ d_3 \\ d_4 \end{Bmatrix}; \{d_1\} = \begin{Bmatrix} u_1 \\ v_1 \end{Bmatrix} \quad (1)$$

Writing out the total eight displacements gives

$$\{d\} = \{u_1 \quad v_1 \quad u_2 \quad v_2 \quad u_3 \quad v_3 \quad u_4 \quad v_4\}^T \quad (2)$$

Since the element shape is an arbitrary quadrilateral, a transformation from the physical shape to a square element in the computational domain will be required in the displacement function selection.

Step 3: Select a Displacement Function

In an isoparametric membrane formulation, the same shape functions that are used to define the element shape are also used to define the displacements within the element. Thus, the shape functions that map the natural coordinates r and s of any point in a square element to the global coordinates x and y in the general quadrilateral are also the shape functions that relate the internal displacements of the element u and v to its nodal displacements $\{d\}$. The transformation between the natural coordinate system and the global is depicted in Figure 15. The natural coordinates are attached to the element and rotate with the element. They need not be parallel with the global coordinates or orthogonal to each other. The four corners and edges of the quadrilateral are bounded by $+1$ or -1 . The displacement of any point P located at (x, y) in the element is described by u and v .

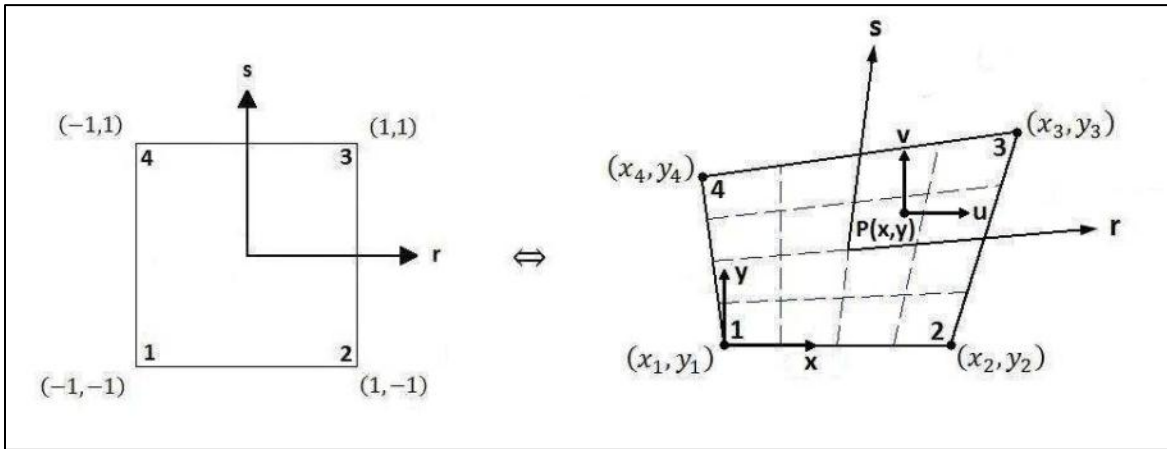


Figure 15: General Quadrilateral Element Mapping to Computational Domain [13]

The size and shape of the quadrilateral is determined by the eight nodal coordinates $x_1, y_1, x_2, y_2, x_3, y_3, x_4, y_4$. Therefore, any internal coordinate can be determined by bilinear interpolation of the natural coordinates for first-order shape functions. The global coordinates can be expressed by eight unknown constants.

$$\begin{aligned} x &= A_1 + A_2 r + A_3 s + A_4 rs \\ y &= A_5 + A_6 r + A_7 s + A_8 rs \end{aligned} \quad (3)$$

The A coefficients are determined by evaluating x and y at the four nodes (-1,-1), (1,-1), (1,1), and (-1,1) in natural coordinates and (x₁,y₁), (x₂,y₂), (x₃,y₃), and (x₄,y₄) in global coordinates and simultaneously solving for the A's.

$$\begin{Bmatrix} x_1 \\ x_2 \\ x_3 \\ x_4 \end{Bmatrix} = \begin{bmatrix} 1 & -1 & -1 & 1 \\ 1 & 1 & -1 & -1 \\ 1 & 1 & 1 & 1 \\ 1 & -1 & 1 & -1 \end{bmatrix} \begin{Bmatrix} A_1 \\ A_2 \\ A_3 \\ A_4 \end{Bmatrix} \quad \begin{Bmatrix} y_1 \\ y_2 \\ y_3 \\ y_4 \end{Bmatrix} = \begin{bmatrix} 1 & -1 & -1 & 1 \\ 1 & 1 & -1 & -1 \\ 1 & 1 & 1 & 1 \\ 1 & -1 & 1 & -1 \end{bmatrix} \begin{Bmatrix} A_5 \\ A_6 \\ A_7 \\ A_8 \end{Bmatrix} \quad (4)$$

Solution of these matrix equations for the A's and substitution of the expressions for the A's back into Eqs. (3) leads to the following mapping:

$$\begin{aligned} x &= \frac{1}{4} [(1-r)(1-s)x_1 + (1+r)(1-s)x_2 + (1+r)(1+s)x_3 + (1-r)(1+s)x_4] \\ y &= \frac{1}{4} [(1-r)(1-s)y_1 + (1+r)(1-s)y_2 + (1+r)(1+s)y_3 + (1-r)(1+s)y_4] \end{aligned} \quad (5)$$

These coordinates can be expressed in matrix form in the following manner:

$$\begin{Bmatrix} x \\ y \end{Bmatrix} = \begin{bmatrix} N_1 & 0 & N_2 & 0 & N_3 & 0 & N_4 & 0 \\ 0 & N_1 & 0 & N_2 & 0 & N_3 & 0 & N_4 \end{bmatrix} \begin{Bmatrix} x_1 \\ y_1 \\ x_2 \\ y_2 \\ x_3 \\ y_3 \\ x_4 \\ y_4 \end{Bmatrix} \quad (6)$$

Here the shape functions N_i relate the nodal coordinates (x_i, y_i) to any (x, y) position along the membrane. They are functions of the natural coordinates (r, s).

$$\begin{aligned} N_1 &= \frac{1}{4}(1-r)(1-s) & N_2 &= \frac{1}{4}(1+r)(1-s) \\ N_3 &= \frac{1}{4}(1+r)(1+s) & N_4 &= \frac{1}{4}(1-r)(1+s) \end{aligned} \quad (7)$$

The shape function partial derivatives with respect to the natural coordinates are

$$\begin{aligned} N_{1,r} &= \frac{1}{4}(-1+s) & N_{2,r} &= \frac{1}{4}(1-s) & N_{3,r} &= \frac{1}{4}(1+s) & N_{4,r} &= \frac{1}{4}(-1-s) \\ N_{1,s} &= \frac{1}{4}(-1+r) & N_{2,s} &= \frac{1}{4}(-1-r) & N_{3,s} &= \frac{1}{4}(1+r) & N_{4,s} &= \frac{1}{4}(1-r) \end{aligned} \quad (8)$$

The partial derivatives of the global coordinates then become

$$\begin{Bmatrix} x_r \\ x_s \end{Bmatrix} = \frac{1}{4} \begin{bmatrix} -1+s & 1-s & 1+s & -1-s \\ -1+r & -1-r & 1+r & 1-r \end{bmatrix} \begin{Bmatrix} x_1 \\ x_2 \\ x_3 \\ x_4 \end{Bmatrix} \quad (9)$$

$$\begin{Bmatrix} y_r \\ y_s \end{Bmatrix} = \frac{1}{4} \begin{bmatrix} -1+s & 1-s & 1+s & -1-s \\ -1+r & -1-r & 1+r & 1-r \end{bmatrix} \begin{Bmatrix} y_1 \\ y_2 \\ y_3 \\ y_4 \end{Bmatrix} \quad (10)$$

The displacement functions are now defined in the same manner as Eq. (6) with the shape functions defined by Eqs. (7):

$$\begin{Bmatrix} u \\ v \end{Bmatrix} = \begin{bmatrix} N_1 & 0 & N_2 & 0 & N_3 & 0 & N_4 & 0 \\ 0 & N_1 & 0 & N_2 & 0 & N_3 & 0 & N_4 \end{bmatrix} \begin{Bmatrix} u_1 \\ v_1 \\ u_2 \\ v_2 \\ u_3 \\ v_3 \\ u_4 \\ v_4 \end{Bmatrix} \quad (11)$$

where u and v are displacements parallel to the global x and y coordinates. Eq. (11) can be represented simply as

$$\{\psi\} = [N]\{d\} \quad (12)$$

Step 4: Define the Strain/Displacement and Stress/Strain Relations

Now that the element has been selected and the displacement functions defined, the strain/displacement matrix [B] must be established such that

$$\{\varepsilon\} = [B]\{d\} \quad (13)$$

The usual relationship between strains and displacements [13] for the two-dimensional case is given as

$$\varepsilon_x = \frac{\partial u}{\partial x} \quad ; \quad \varepsilon_y = \frac{\partial v}{\partial y} \quad ; \quad \gamma_{xy} = \frac{\partial u}{\partial y} + \frac{\partial v}{\partial x} \quad (14)$$

Eqs. (14) can be combined into the following matrix equation:

$$\begin{Bmatrix} \varepsilon_x \\ \varepsilon_y \\ \gamma_{xy} \end{Bmatrix} = \begin{bmatrix} \frac{\partial(\cdot)}{\partial x} & 0 \\ 0 & \frac{\partial(\cdot)}{\partial y} \\ \frac{\partial(\cdot)}{\partial y} & \frac{\partial(\cdot)}{\partial x} \end{bmatrix} \begin{Bmatrix} u \\ v \end{Bmatrix} \quad (15)$$

or more succinctly

$$\{\varepsilon\} = [D']\{\psi\} \quad (16)$$

Since the global coordinates are themselves functions of the natural coordinates (Eqs. (6) and (7)), the Jacobian is needed to express the partial derivatives of the global coordinates.

$$\frac{\partial(\quad)}{\partial x} = \frac{1}{|J|} \left[\frac{\partial(\quad)}{\partial r} y_s - \frac{\partial(\quad)}{\partial s} y_r \right] \quad ; \quad \frac{\partial(\quad)}{\partial y} = \frac{1}{|J|} \left[\frac{\partial(\quad)}{\partial s} x_r - \frac{\partial(\quad)}{\partial r} x_s \right] \quad (17)$$

Where

$$|J| = x_r y_s - x_s y_r \quad (18)$$

Substituting Eqs. (17) into Eq. (15) yields an alternate form of [D']:

$$[D'] = \frac{1}{|J|} \begin{bmatrix} \frac{\partial(\quad)}{\partial r} y_s - \frac{\partial(\quad)}{\partial s} y_r & 0 \\ 0 & \frac{\partial(\quad)}{\partial s} x_r - \frac{\partial(\quad)}{\partial r} x_s \\ \frac{\partial(\quad)}{\partial s} x_r - \frac{\partial(\quad)}{\partial r} x_s & \frac{\partial(\quad)}{\partial r} y_s - \frac{\partial(\quad)}{\partial s} y_r \end{bmatrix} \quad (19)$$

Substitution of Eq. (12) into Eq. (16) leads to the definition of the strain/displacement matrix [B] by Eq. (13):

$$\begin{matrix} [B] & = & [D'] & [N] \\ (3 \times 8) & & (3 \times 2) & (2 \times 8) \end{matrix} \quad (20)$$

Thus [B] is computed by operation of [D'] on [N]:

$$[B(r, s)] = \frac{1}{|J|} \begin{bmatrix} B_1 & B_2 & B_3 & B_4 \end{bmatrix} \quad (21)$$

where the submatrices of [B] are given by

$$[B_i] = \begin{bmatrix} (N_{i,r})y_s - (N_{i,s})y_r & 0 \\ 0 & (N_{i,s})x_r - (N_{i,r})x_s \\ (N_{i,s})x_r - (N_{i,r})x_s & (N_{i,r})y_s - (N_{i,s})y_r \end{bmatrix} \quad (22)$$

The stresses are then related to the strains by the constitutive matrix [D] [13]

$$\{\sigma\} = [D]\{\varepsilon\} \quad (23)$$

where [D] is defined for a state of plane stress as

$$[D] = \frac{E}{1 - \nu^2} \begin{bmatrix} 1 & \nu & 0 \\ \nu & 1 & 0 \\ 0 & 0 & \frac{1 - \nu}{2} \end{bmatrix} \quad (24)$$

where E is Young's modulus and ν is Poisson's ratio. Upon substitution of Eq. (13) into Eq. (14), the element stresses are related directly to the nodal displacements.

$$\{\sigma\} = [D][B]\{d\} \quad (25)$$

Step 5: Derive the Element Stiffness Matrix

To derive an expression for the stiffness matrix $[k]$, the principle of minimum potential energy is employed, where the strain energy is given by

$$U = \frac{1}{2} \iiint_V \{\varepsilon\}^T \{\sigma\} dV \quad (26)$$

A derivation following this method is given in Reference [13], and results in the following expression for the stiffness matrix:

$$[k] = \iiint_V [B]^T [D] [B] dV \quad (27)$$

Since $[B]$ does not vary through the thickness of the membrane element, the stiffness matrix becomes an area integral.

$$[k] = t \iint_A [B]^T [D] [B] dx dy \quad (28)$$

However, $[B]$ is a function of the natural coordinates r and s , and not the global coordinates x and y which define the volume over which the integration is to be performed. Thus the variables must be transformed using the determinant of the Jacobian matrix J (a proof for a general transformation is given in [14]).

$$\iint_A f(x, y) dx dy = \iint_A f(r, s) |J| dr ds \quad (29)$$

Since the area is bounded by ± 1 in the natural coordinates, $[k]$ becomes

$$[k] = t \int_{-1}^1 \int_{-1}^1 [B]^T [D] [B] |J| dr ds \quad (30)$$

Since $[B]$ is a rather complicated expression, the integration determining the element stiffness matrix is best carried out numerically. In the presented work the Gaussian quadrature method is used to evaluate the integral.

2.2.2.2 Quadrilateral Bending Element

A general quadrilateral bending element formulation was not found among the finite element literature. Therefore a formulation of such a bending element was derived using classic Kirchhoff plate theory and using the same shape functions that defined the membrane element shape in the previous section. The formulation is essentially a synthesis of Chapters 10 and 12 found in Reference [13]. A stand-alone derivation of the bending element stiffness matrix is provided in Reference [7] with the results of Steps 2 through 5 repeated here for completeness.

Step 2: Select the Element Type

A plate element can translate and rotate out-of-plane. This gives the plate element three degrees of freedom per node, a transverse displacement w and two rotations θ_x and θ_y .

$$\{d\} = \begin{Bmatrix} d_i \\ d_j \\ d_m \\ d_n \end{Bmatrix} ; \quad \{d_i\} = \begin{Bmatrix} w_i \\ \theta_{xi} \\ \theta_{yi} \end{Bmatrix} \quad (31)$$

Writing out the 12 displacements gives

$$\{d\} = \left\{ w_i \ \theta_{xi} \ \theta_{yi} \ w_j \ \theta_{xj} \ \theta_{yj} \ w_m \ \theta_{xm} \ \theta_{ym} \ w_n \ \theta_{xn} \ \theta_{yn} \right\}^T \quad (32)$$

As with the membrane element, a transformation from the arbitrary quadrilateral to a square element in the computational domain is required.

Step 3: Select a Displacement Function

Although the same shape functions that are used to define the membrane element shape are also used to define the bending element shape, the formulation is not technically isoparametric because the nodal displacements are out-of-plane and have their own shape functions. The same element shape mapping is shown in Figure 16 for the bending element, where representative loads are shown at node i .

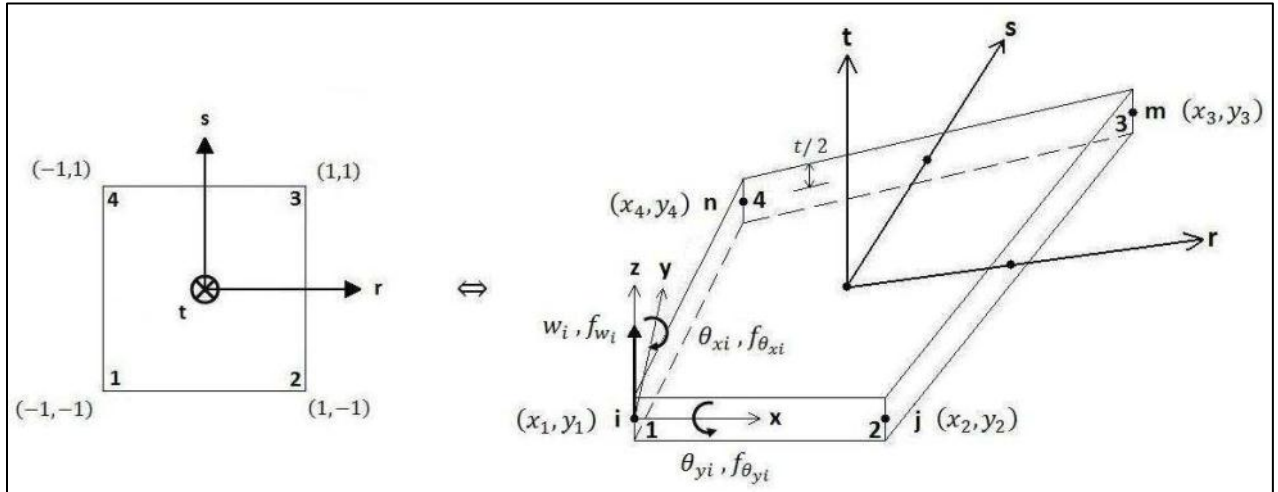


Figure 16: Mapping of General Quadrilateral Element to Computational Domain

As with the membrane element, the size and shape of the quadrilateral is determined by the eight nodal coordinates by Eqs. (6) and (7), and obviously have the same partial derivatives (Eqs. (9) and (10)). Given that there are 12 degrees of freedom, a 12-term polynomial is selected for the displacement function that enables rigid body motion and constant strain.

$$w = a_1 + a_2x + a_3y + a_4x^2 + a_5xy + a_6y^2 + a_7x^3 + a_8x^2y + a_9xy^2 + a_{10}y^3 + a_{11}x^3y + a_{12}xy^3 \quad (33)$$

The rotations follow from Eq. (33) since

$$\theta_x = \frac{\partial w}{\partial y} \quad ; \quad \theta_y = -\frac{\partial w}{\partial x} \quad (34)$$

The displacements can be put into the form of Eq. (12) by following the process found in Reference [7].

Step 4: Define Curvature/Displacement and Moment/Curvature Relations

Rather than relating the displacements to the strains (Eq. (13)) which vary linearly through the thickness of the bending element, displacements are instead related to the curvatures:

$$\{\kappa\} = [B]\{d\} \quad (35)$$

The curvature/displacement matrix [B] is calculated by the process explained in Reference [7]. Because the stresses also vary linearly through the thickness of the bending element, the curvatures are related to the moments instead.

$$\{M\} = [D]\{\kappa\} \quad (36)$$

where the constitutive matrix [D] is defined as

$$[D] = D \begin{bmatrix} 1 & \nu & 0 \\ \nu & 1 & 0 \\ 0 & 0 & \frac{1-\nu}{2} \end{bmatrix} \quad (37)$$

Here D is expressed as

$$D = \frac{Et^3}{12(1-\nu^2)} \quad (38)$$

Combining Eqs. (35) and (36) relates the moments to the displacements.

$$\{M\} = [D][B]\{d\} \quad (39)$$

Step 5: Derive the Element Stiffness Matrix

Step 5 must be modified slightly from the process followed in the membrane derivation, since moments are computed rather than stresses. The potential energy of the plate is given as

$$U = \frac{1}{2} \iint (M_x\kappa_x + M_y\kappa_y + M_{xy}\kappa_{xy}) dA \quad (40)$$

Minimizing the potential energy leads to a slight difference from Eq. (28), where thickness no longer sits in front of the integral.

$$[k] = \iint_A [B]^T [D] [B] dx dy \quad (41)$$

The rest of Step 5 is the same for the bending element and results in a [12 x 12] stiffness matrix.

2.2.2.3 Combined Quadrilateral Membrane-Bending Element

A shell element is a thin curved surface with six degrees of freedom at each node. When the radius of curvature approaches infinity, the shell element approaches a flat plate. When a surface is modeled by many small shell elements, each element may be considered as a flat plate with a particular orientation in space. A conventional finite plate bending element, such as discussed in the previous section, does not allow in-plane membrane deformation. In the analysis of three-dimensional structures, membrane and bending stiffnesses are uncoupled for small displacements. Thus, a shell element can be formed by superimposing the membrane and bending stiffness matrices together in the following manner:

$$[k]_{20 \times 20} = \left[\begin{array}{c|c} [k_m]_{8 \times 8} & [0]_{8 \times 12} \\ \hline [0]_{12 \times 8} & [k_b]_{12 \times 12} \end{array} \right] \quad (42)$$

where subscripts m and b denote membrane and bending deformations of the shell element. In this formulation, the bending and membrane elements do not share common degrees of freedom and hence are uncoupled. Note that this results in a stiffness matrix of order [20 x 20], or five degrees of freedom per node. The element structure stiffness equations are

$$\left\{ \begin{array}{c} \{f_m\}_{8 \times 1} \\ \{f_b\}_{12 \times 1} \end{array} \right\} = \left[\begin{array}{c|c} [k_m]_{8 \times 8} & [0]_{8 \times 12} \\ \hline [0]_{12 \times 8} & [k_b]_{12 \times 12} \end{array} \right] \left\{ \begin{array}{c} \{d_m\}_{8 \times 1} \\ \{d_b\}_{12 \times 1} \end{array} \right\} \quad (43)$$

For a single shell element, there is no twisting, in-plane rotation θ_z (referred to as a “drilling” rotation), but for an assemblage of elements, a bending rotation in one element may result in a drilling rotation in an adjacent element. To account for this, the drilling degree of freedom must be added to each node, raising the order of the stiffness matrix to a [24 x 24].

$$\left\{ \begin{array}{c} \{f_m\}_{8 \times 1} \\ \{f_b\}_{12 \times 1} \\ \{f_{\theta_z}\}_{4 \times 1} \end{array} \right\} = \left[\begin{array}{c|c|c} [k_m]_{8 \times 8} & [0]_{8 \times 12} & [0]_{8 \times 4} \\ \hline [0]_{12 \times 8} & [k_b]_{12 \times 12} & [0]_{12 \times 4} \\ \hline [0]_{4 \times 20} & [0]_{4 \times 4} & [0]_{4 \times 4} \end{array} \right] \left\{ \begin{array}{c} \{d_m\}_{8 \times 1} \\ \{d_b\}_{12 \times 1} \\ \{d_{\theta_z}\}_{4 \times 1} \end{array} \right\} \quad (44)$$

Since there is no stiffness associated with the drilling degrees of freedom, the stiffness matrix will be singular if all the elements joining a node are coplanar. If flat geometry is to be analyzed by superposition, the on-diagonal null matrix is replaced with an artificial stiffness matrix which causes the twisting rotations to produce corresponding moments M_z . One suggested fictitious stiffness matrix [15] is the following:

$$\begin{Bmatrix} M_{z1} \\ M_{z2} \\ M_{z3} \\ M_{z4} \end{Bmatrix} = \alpha EV \begin{bmatrix} 1.0 & -0.5 & -0.5 & -0.5 \\ -0.5 & 1.0 & -0.5 & -0.5 \\ -0.5 & -0.5 & 1.0 & -0.5 \\ -0.5 & -0.5 & -0.5 & 1.0 \end{bmatrix} \begin{Bmatrix} \theta_{z1} \\ \theta_{z2} \\ \theta_{z3} \\ \theta_{z4} \end{Bmatrix} \quad (45)$$

where α is a small number such as 0.3, E is Young's modulus, and V is the elemental volume. The element volume can be calculated directly from its coordinates by the following formula:

$$V = \frac{t}{2} \left(\begin{vmatrix} x_1 & x_2 \\ y_1 & y_2 \end{vmatrix} + \begin{vmatrix} x_2 & x_3 \\ y_2 & y_3 \end{vmatrix} + \begin{vmatrix} x_3 & x_4 \\ y_3 & y_4 \end{vmatrix} + \begin{vmatrix} x_4 & x_1 \\ y_4 & y_1 \end{vmatrix} \right) \quad (46)$$

where t is the element thickness. The current order of the displacement matrix in Eq. (44) is

$$\{d\} = \{u_i \ v_i \ u_j \ v_j \ u_m \ v_m \ u_n \ v_n \ w_i \ \theta_{xi} \ \theta_{yi} \ w_j \ \theta_{xj} \ \theta_{yj} \ w_m \ \theta_{xm} \ \theta_{ym} \ w_n \ \theta_{xn} \ \theta_{yn} \ \theta_{zi} \ \theta_{zj} \ \theta_{zm} \ \theta_{zn}\}^T \quad (47)$$

Following the degrees-of-freedom indexing scheme that will be described in Section 2.2.3, the displacement vector should be ordered as follows:

$$\{d\} = \{u_i \ v_i \ w_i \ \theta_{xi} \ \theta_{yi} \ \theta_{zi} \ u_j \ v_j \ w_j \ \theta_{xj} \ \theta_{yj} \ \theta_{zj} \ u_m \ v_m \ w_m \ \theta_{xm} \ \theta_{ym} \ \theta_{zm} \ u_n \ v_n \ w_n \ \theta_{xn} \ \theta_{yn} \ \theta_{zn}\}^T \quad (48)$$

Before rearranging the combined stiffness matrix [k], the membrane and bending stiffness matrices can be further broken down into submatrices.

$$[k_m]_{8 \times 8} = \begin{bmatrix} [k_{11}]_m & [k_{12}]_m & [k_{13}]_m & [k_{14}]_m \\ [k_{21}]_m & [k_{22}]_m & [k_{23}]_m & [k_{24}]_m \\ [k_{31}]_m & [k_{32}]_m & [k_{33}]_m & [k_{34}]_m \\ [k_{41}]_m & [k_{42}]_m & [k_{43}]_m & [k_{44}]_m \end{bmatrix} \quad (49)$$

$$[k_b]_{12 \times 12} = \begin{bmatrix} [k_{11}]_b & [k_{12}]_b & [k_{13}]_b & [k_{14}]_b \\ [k_{21}]_b & [k_{22}]_b & [k_{23}]_b & [k_{24}]_b \\ [k_{31}]_b & [k_{32}]_b & [k_{33}]_b & [k_{34}]_b \\ [k_{41}]_b & [k_{42}]_b & [k_{43}]_b & [k_{44}]_b \end{bmatrix} \quad (50)$$

The fictitious stiffness matrix of Eq. (45) can be rewritten slightly as follows:

$$[k_f]_{4 \times 4} = \begin{bmatrix} k_f & k'_f & k'_f & k'_f \\ k'_f & k_f & k'_f & k'_f \\ k'_f & k'_f & k_f & k'_f \\ k'_f & k'_f & k'_f & k_f \end{bmatrix} \quad (51)$$

where k_f is defined as

$$k_f = \alpha EV \quad (52)$$

and k'_f is defined as

$$k'_f = -0.5 \alpha EV \quad (53)$$

Using the notation of Eq. (49) through Eq. (51), the total membrane and bending stiffness matrix is combined [16] in the following manner:

$$[k]_{24 \times 24} = \begin{bmatrix} [k_{11}]_m & 0 & 0 & 0 & 0 & [k_{12}]_m & 0 & 0 & 0 & 0 & [k_{13}]_m & 0 & 0 & 0 & 0 & [k_{14}]_m & 0 & 0 & 0 & 0 \\ 0 & 0 & 0 & 0 & 0 & 0 & 0 & 0 & 0 & 0 & 0 & 0 & 0 & 0 & 0 & 0 & 0 & 0 & 0 \\ 0 & 0 & [k_{11}]_b & 0 & 0 & 0 & [k_{12}]_b & 0 & 0 & 0 & [k_{13}]_b & 0 & 0 & 0 & [k_{14}]_b & 0 & 0 & 0 & 0 \\ 0 & 0 & 0 & 0 & 0 & 0 & 0 & 0 & 0 & 0 & 0 & 0 & 0 & 0 & 0 & 0 & 0 & 0 & 0 \\ 0 & 0 & 0 & 0 & 0 & k_f & 0 & 0 & 0 & 0 & 0 & 0 & 0 & 0 & 0 & 0 & 0 & 0 & 0 \\ 0 & 0 & 0 & 0 & 0 & 0 & 0 & 0 & 0 & 0 & 0 & 0 & 0 & 0 & 0 & 0 & 0 & 0 & 0 \\ [k_{21}]_m & 0 & 0 & 0 & 0 & [k_{22}]_m & 0 & 0 & 0 & 0 & [k_{23}]_m & 0 & 0 & 0 & 0 & [k_{24}]_m & 0 & 0 & 0 & 0 \\ 0 & 0 & 0 & 0 & 0 & 0 & 0 & 0 & 0 & 0 & 0 & 0 & 0 & 0 & 0 & 0 & 0 & 0 & 0 \\ 0 & 0 & [k_{21}]_b & 0 & 0 & 0 & [k_{22}]_b & 0 & 0 & 0 & [k_{23}]_b & 0 & 0 & 0 & [k_{24}]_b & 0 & 0 & 0 & 0 \\ 0 & 0 & 0 & 0 & 0 & 0 & 0 & 0 & 0 & 0 & 0 & 0 & 0 & 0 & 0 & 0 & 0 & 0 & 0 \\ 0 & 0 & 0 & 0 & 0 & k'_f & 0 & 0 & 0 & 0 & 0 & 0 & 0 & 0 & 0 & 0 & 0 & 0 & 0 \\ [k_{31}]_m & 0 & 0 & 0 & 0 & [k_{32}]_m & 0 & 0 & 0 & 0 & [k_{33}]_m & 0 & 0 & 0 & 0 & [k_{34}]_m & 0 & 0 & 0 & 0 \\ 0 & 0 & 0 & 0 & 0 & 0 & 0 & 0 & 0 & 0 & 0 & 0 & 0 & 0 & 0 & 0 & 0 & 0 & 0 \\ 0 & 0 & [k_{31}]_b & 0 & 0 & 0 & [k_{32}]_b & 0 & 0 & 0 & [k_{33}]_b & 0 & 0 & 0 & [k_{34}]_b & 0 & 0 & 0 & 0 \\ 0 & 0 & 0 & 0 & 0 & 0 & 0 & 0 & 0 & 0 & 0 & 0 & 0 & 0 & 0 & 0 & 0 & 0 & 0 \\ 0 & 0 & 0 & 0 & 0 & k'_f & 0 & 0 & 0 & 0 & 0 & 0 & 0 & 0 & 0 & 0 & 0 & 0 & 0 \\ [k_{41}]_m & 0 & 0 & 0 & 0 & [k_{42}]_m & 0 & 0 & 0 & 0 & [k_{43}]_m & 0 & 0 & 0 & 0 & [k_{44}]_m & 0 & 0 & 0 & 0 \\ 0 & 0 & 0 & 0 & 0 & 0 & 0 & 0 & 0 & 0 & 0 & 0 & 0 & 0 & 0 & 0 & 0 & 0 & 0 \\ 0 & 0 & [k_{41}]_b & 0 & 0 & 0 & [k_{42}]_b & 0 & 0 & 0 & [k_{43}]_b & 0 & 0 & 0 & [k_{44}]_b & 0 & 0 & 0 & 0 \\ 0 & 0 & 0 & 0 & 0 & 0 & 0 & 0 & 0 & 0 & 0 & 0 & 0 & 0 & 0 & 0 & 0 & 0 & 0 \\ 0 & 0 & 0 & 0 & 0 & k'_f & 0 & 0 & 0 & 0 & 0 & 0 & 0 & 0 & 0 & 0 & 0 & 0 & k_f \end{bmatrix} \quad (54)$$

For geometries that are not flat with entirely coplanar elements, each “shell” element has a unique orientation with a local axis system, indicated by a $\hat{\cdot}$ over the variable. A transformation matrix [T] can be created to map global displacements and forces to corresponding local displacements and forces.

$$\{\hat{d}\} = [T]\{d\} \quad ; \quad \{\hat{f}\} = [T]\{f\} \quad (55)$$

The local and global stiffness matrix equations are given as

$$\{\hat{f}\} = [\hat{k}]\{\hat{d}\} \quad ; \quad \{f\} = [k]\{d\} \quad (56)$$

Substituting the local displacements and forces of Eqs. (55) into the local stiffness matrix equation yields

$$[T]\{f\} = [\hat{k}][T]\{d\} \quad (57)$$

which leads to

$$\{f\} = [T]^{-1}[\hat{k}][T]\{d\} \quad (58)$$

Thus the global stiffness matrix is computed via the following relation:

$$[k] = [T]^{-1}[\hat{k}][T] \quad (59)$$

Since [T] is an orthogonal matrix, the transpose of [T] can be used instead of its inverse to save computational time.

$$[k] = [T]^T[\hat{k}][T] \quad (60)$$

Local forces can also be mapped back to the global forces using the transpose.

$$\{f\} = [T]^T\{\hat{f}\} \quad (61)$$

The transformation matrix [17] relating global degrees of freedom to local is expressed as

$$\begin{Bmatrix} \hat{u} \\ \hat{v} \\ \hat{w} \\ \hat{\theta}_x \\ \hat{\theta}_y \\ \hat{\theta}_z \end{Bmatrix} = \begin{bmatrix} l_{11} & l_{12} & l_{13} & 0 & 0 & 0 \\ l_{21} & l_{22} & l_{23} & 0 & 0 & 0 \\ l_{31} & l_{32} & l_{33} & 0 & 0 & 0 \\ 0 & 0 & 0 & l_{11} & l_{12} & l_{13} \\ 0 & 0 & 0 & l_{21} & l_{22} & l_{23} \\ 0 & 0 & 0 & l_{31} & l_{32} & l_{33} \end{bmatrix} \begin{Bmatrix} u \\ v \\ w \\ \theta_x \\ \theta_y \\ \theta_z \end{Bmatrix} \quad (62)$$

where the l_{ij} 's are the direction cosines given as

$$\begin{aligned} l_{11} &= \cos(\mathbf{e}_x, \mathbf{e}_r) \quad ; \quad l_{12} = \cos(\mathbf{e}_y, \mathbf{e}_r) \quad ; \quad l_{13} = \cos(\mathbf{e}_z, \mathbf{e}_r) \\ l_{21} &= \cos(\mathbf{e}_x, \mathbf{e}_s) \quad ; \quad l_{22} = \cos(\mathbf{e}_y, \mathbf{e}_s) \quad ; \quad l_{23} = \cos(\mathbf{e}_z, \mathbf{e}_s) \\ l_{31} &= \cos(\mathbf{e}_x, \mathbf{e}_t) \quad ; \quad l_{32} = \cos(\mathbf{e}_y, \mathbf{e}_t) \quad ; \quad l_{33} = \cos(\mathbf{e}_z, \mathbf{e}_t) \end{aligned} \quad (63)$$

Eq. (62) transforms the displacements at a particular node, for example, at node i:

$$\{\hat{d}_i\} = [T_n]\{d_i\} \quad (64)$$

Thus, the transformation for a four node element becomes

$$[T]_{24 \times 24} = \begin{bmatrix} [T_n]_{6 \times 6} & 0 & 0 & 0 \\ 0 & [T_n]_{6 \times 6} & 0 & 0 \\ 0 & 0 & [T_n]_{6 \times 6} & 0 \\ 0 & 0 & 0 & [T_n]_{6 \times 6} \end{bmatrix} \quad (65)$$

The direction cosines can of course be calculated from the familiar calculus formula

$$l_{ij} = \frac{\mathbf{v}_i \cdot \mathbf{v}_j}{\|\mathbf{v}_i\| \|\mathbf{v}_j\|} \quad (66)$$

However, determining the unit vectors is not as straight forward. The global unit vectors are simply

$$\mathbf{e}_x = [1 \ 0 \ 0] \quad ; \quad \mathbf{e}_y = [0 \ 1 \ 0] \quad ; \quad \mathbf{e}_z = [0 \ 0 \ 1] \quad (67)$$

but the unit vectors of the natural coordinates will require some effort to calculate. The element normal unit vector \mathbf{e}_t can be computed from the cross product of two vectors lying in the element, for example, vectors extending from node 1 to nodes 2 and 4 of the element as shown in Figure 17.

$$\mathbf{e}_t = \frac{\vec{v}_{21} \times \vec{v}_{41}}{\|\vec{v}_{21} \times \vec{v}_{41}\|} \quad (68)$$

In order to determine the unit vectors \mathbf{e}_r and \mathbf{e}_s , the midpoint of the element and the midpoints of the sides $r = 1$ and $s = 1$ are needed (shown as P_5 , P_6 , and P_7 in Figure 17). The x and y coordinates of these three points are calculated by evaluating Eqs. (6) and (7) at $(r, s) = (0, 0)$, $(1, 0)$, and $(0, 1)$. The plane of the element can be defined by its normal vector and one of its four sets of nodal coordinates:

$$e_{tx}(x - x_1) + e_{ty}(y - y_1) + e_{tz}(z - z_1) = 0 \quad (69)$$

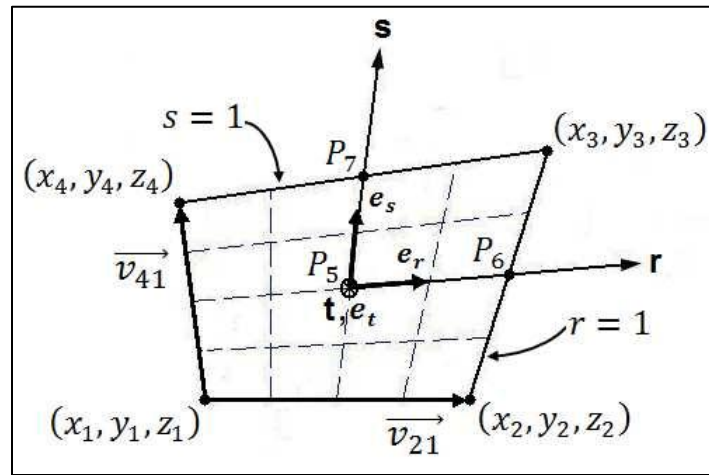


Figure 17: Natural Coordinate Unit Vectors

With the x and y coordinates obtained from the shape function mapping, Eq. (69) can be evaluated to determine the z coordinates.

$$z = z_1 - \frac{1}{e_{tz}}[e_{tx}(x - x_1) + e_{ty}(y - y_1)] \quad (70)$$

Thus, unit vectors e_r and e_s are the normalized vectors calculated with the coordinates of points 5, 6, and 7.

$$\begin{aligned} e_s &= \frac{\langle P_{6x} - P_{5x}, P_{6y} - P_{5y}, P_{6z} - P_{5z} \rangle}{\|\langle P_{6x} - P_{5x}, P_{6y} - P_{5y}, P_{6z} - P_{5z} \rangle\|} \\ e_s &= \frac{\langle P_{7x} - P_{5x}, P_{7y} - P_{5y}, P_{7z} - P_{5z} \rangle}{\|\langle P_{7x} - P_{5x}, P_{7y} - P_{5y}, P_{7z} - P_{5z} \rangle\|} \end{aligned} \quad (71)$$

With the unit vectors e_r , e_s , and e_t , Eq. (66) can be applied nine times to compute the direction cosines of Eqs. (63).

2.2.3 Global Stiffness Matrix

Step 6 of the finite element method involves assembling the local stiffness matrices together to form the global stiffness matrix for the structure. But before the global stiffness matrix can be compiled, the elemental stiffness matrices must each be evaluated by Eq. (30), Eq. (41), or Eq. (54). A procedure is constructed to loop through each element in the computational domain. Mentioned in Section 2.2.1, the elements are indexed by counting down through the rows and then to the right through the columns. The degrees of freedom are also numbered in this fashion along the nodes. An example two DOF membrane mesh is shown in Figure 18. The degrees of freedom corresponding to each element are then ordered in a vector. The arrows in Figure 18 indicate that the degrees of freedom are counted counterclockwise starting with the bottom left hand corner of the element (see also Figure 15). Indices representing the column and row number of the element's position within the mesh facilitate selecting the corresponding degrees of freedom for the element based on its number. Along with the degrees of freedom, the nodal coordinates corresponding to each element will also need to be assembled to compute the strain-displacement matrix, and ultimately evaluate the stiffness matrix. The nodal coordinates define the shape of an element, which alone differentiates one element's stiffness over another's.

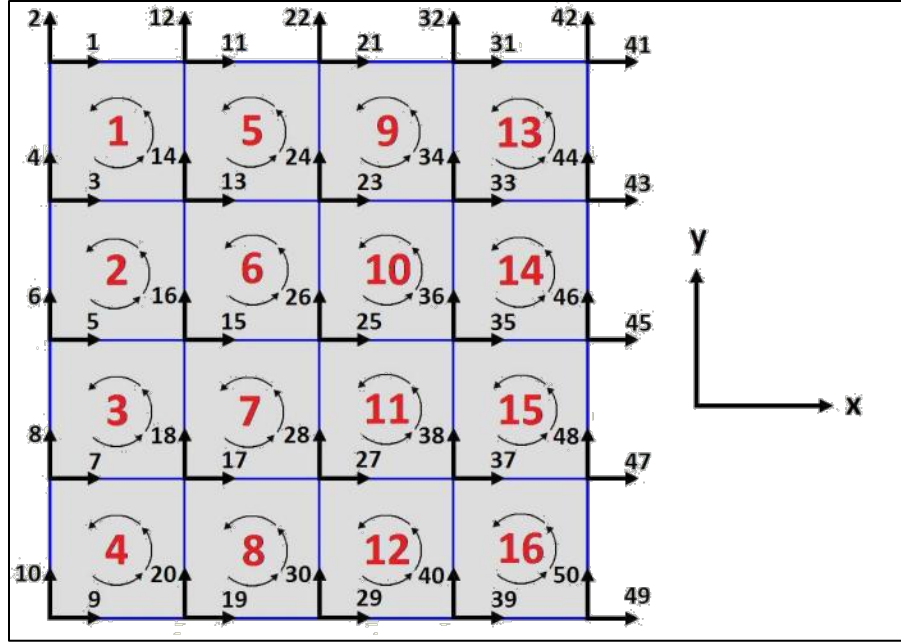


Figure 18: Computational Domain Indexing Example

Once all of the elemental stiffness matrices $[k_e]$ have been evaluated, the direct stiffness method [13] forms the global stiffness matrix $[K]$ by directly assembling individual element stiffness matrices. In other words, elemental stiffness matrices are superimposed to form the total structure stiffness matrix.

$$[K] = \sum_{e=1}^N [k_e] \quad (72)$$

2.2.4 Displacement Solution

In Step 7 of the finite element method, the boundary conditions consisting of the external forces and any constrained degrees of freedom are applied to the global structure stiffness equation. In a manner similar to the global stiffness matrix, the global nodal loads are obtained by lumping the body forces, distributed loads, and concentrated nodal loads at the proper nodes into a column vector. Section 2.3.2 describes how the aerodynamic load calculated for the bird wing is divided among the nodes.

$$\{F\} = \sum_{e=1}^N \{f_e\} \quad (73)$$

Resolving body and surface forces into concentrated nodal loads usually involves a single or double integral. An example of integrating a surface load can be found in Reference [13]. The fixed and free degrees of freedom are specified in two different vectors. For instance, one boundary condition choice for the bird wing is to clamp the root chord. In this case, the user would specify the degrees of freedom along the root to be fixed and all other degrees of freedom as free. A more detailed description of the process and associated MATLAB program is discussed in Reference [7]. An example output is shown in Figure 19 for a two-sectioned, 3-DOF model.

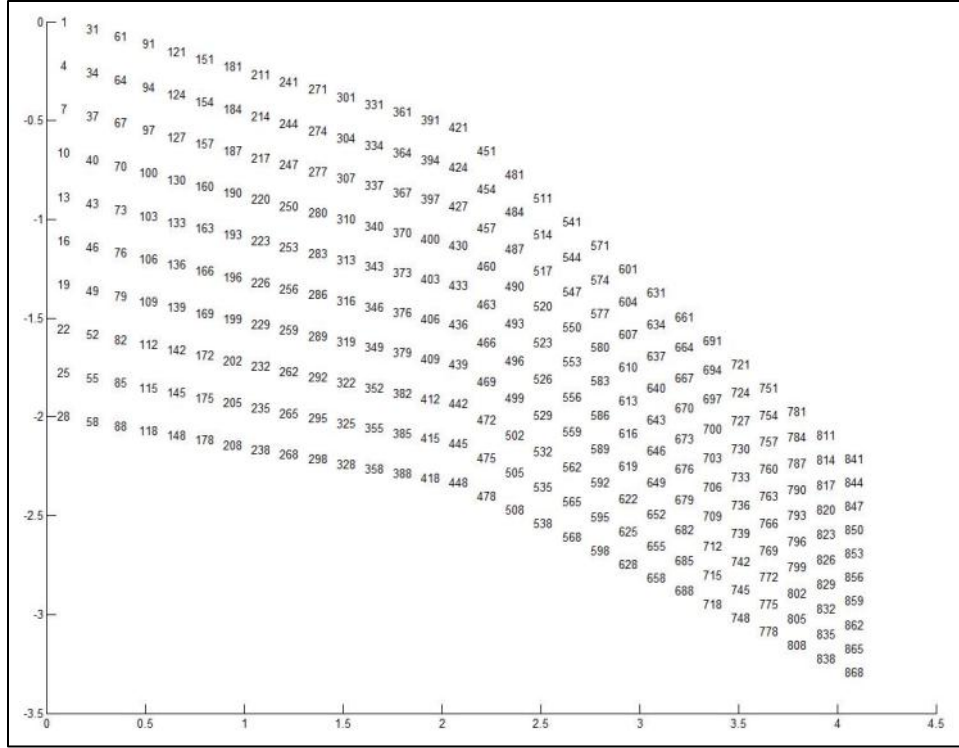


Figure 19: Computational Domain Indexing Example

With the fixed degrees of freedom specified, the corresponding displacements can be directly set to zero in the total structure displacement matrix $\{d\}$. Thus the global structure stiffness equations can be solved.

$$\{F\} = [K]\{d\} \quad (74)$$

It is important to note that $\{F\}$ and $\{d\}$ may represent vectors of moments and rotations rather than forces and translations. With the free DOF specified, Eq. (74) can be elegantly solved in MATLAB by the following command:

$$d(freedofs, 1) = K(freedofs, freedofs) \backslash F(freedofs, 1) \quad (75)$$

2.2.5 Element Stresses

The final step of the method consists of visualizing the results of the displacement solution. After calculating the displacements $\{d\}$, the elemental strains and stresses are computed from Eqs. (13) and (25), respectively. For the two-dimensional state of stress, three independent stresses exist and are represented by the column vector

$$\{\sigma\} = \begin{Bmatrix} \sigma_x \\ \sigma_y \\ \tau_{xy} \end{Bmatrix} \quad (76)$$

The principal stresses are determined from Mohr's Circle [18].

$$\sigma_{max} = \frac{\sigma_x + \sigma_y}{2} + \sqrt{\left(\frac{\sigma_x - \sigma_y}{2}\right)^2 + \tau_{xy}^2} \quad (77)$$

$$\sigma_{min} = \frac{\sigma_x + \sigma_y}{2} - \sqrt{\left(\frac{\sigma_x - \sigma_y}{2}\right)^2 + \tau_{xy}^2} \quad (78)$$

The von Mises effective stress σ_{vm} [19] is defined as the uniaxial tensile stress that would create the same distortion energy as is created by the actual combination of applied stresses, and thus treats multiaxial stresses as if they were due to pure tensile loading. Von Mises stress for the two-dimensional case can be calculated with the principal stress.

$$\sigma_{vm} = \sqrt{\sigma_{max}^2 - \sigma_{max}\sigma_{min} + \sigma_{min}^2} \quad (79)$$

When plotting a structure's deformed state, the element patches can be colored by the von Mises stress for effective visualization.

Validation of the membrane and bending models against classical analysis are detailed in Reference [7]. Comparisons with the individual membrane and bending models are also made for the combined membrane-bending model.

2.3 Aerodynamics

2.3.1 Perching Maneuvers

In the interest of capturing wing loads on a MAV during a similar maneuver, perching maneuver data was selected from Reference [20]. Four points along the maneuver were selected from which the aircraft and aerodynamic data were extracted. The four selected points are marked on Figure 20 through Figure 23, which give the data curves of altitude versus range, range versus time, angle of attack versus range, pitch versus range, and velocity versus range. Table 2 provides the data estimated from the figures at each point.

The four points are intended to represent the more extreme aerodynamic conditions of the maneuver. Point 1 is at the beginning of the trajectory when the MAV is likely in the 15° back sweep position (Figure 13). The dive can be said to have begun since the near -100°/s angle of attack and pitch derivatives indicate the vehicle is pitching down fast from its cruising or loitering condition. At Point 2, the MAV is midway through the dive and experiences the peak velocity of the maneuver. The MAV starts to pitch up again, though the pitch angle is still negative. The wings are in the dive configuration (Figure 14), much like those of the eagle owl in Figure 2. At Point 3, the MAV is at the bottom of the dive and begins ascending. The pitch rate is at a maximum due to how fast the MAV is still moving. The wings are transitioning from the dive to forward sweep configuration, and so the configuration with no sweep (Figure 12) is selected at this point. Finally at Point 4, the MAV has covered 98.5 percent of the range and is at a low velocity as it is pulling up into a vertical stance. Consequently the angle of attack is post-stall and the angle of attack rate is at a very high value of 216°/s. The wings are fully flared with forward sweep (Figure 11) so that they can collect as much drag as possible to bring the vehicle to a halt.

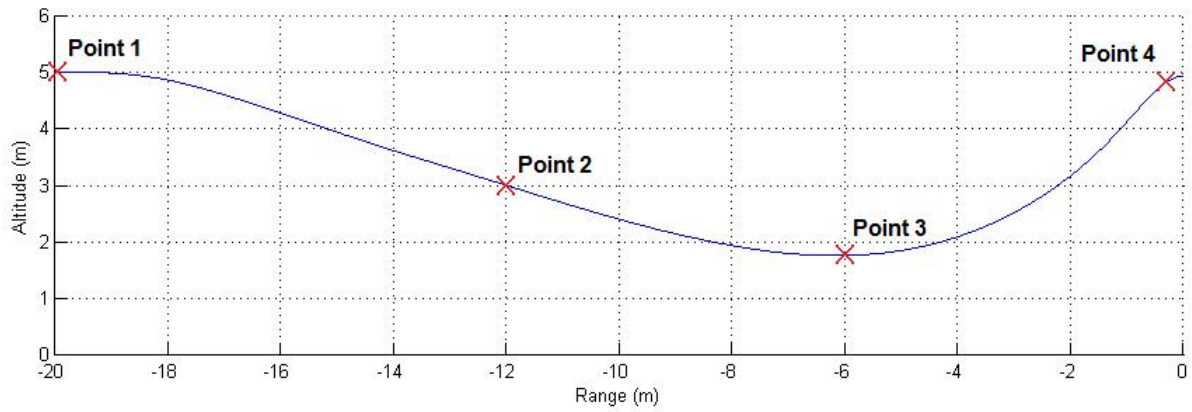


Figure 20: Perching Maneuver: Altitude vs. Range

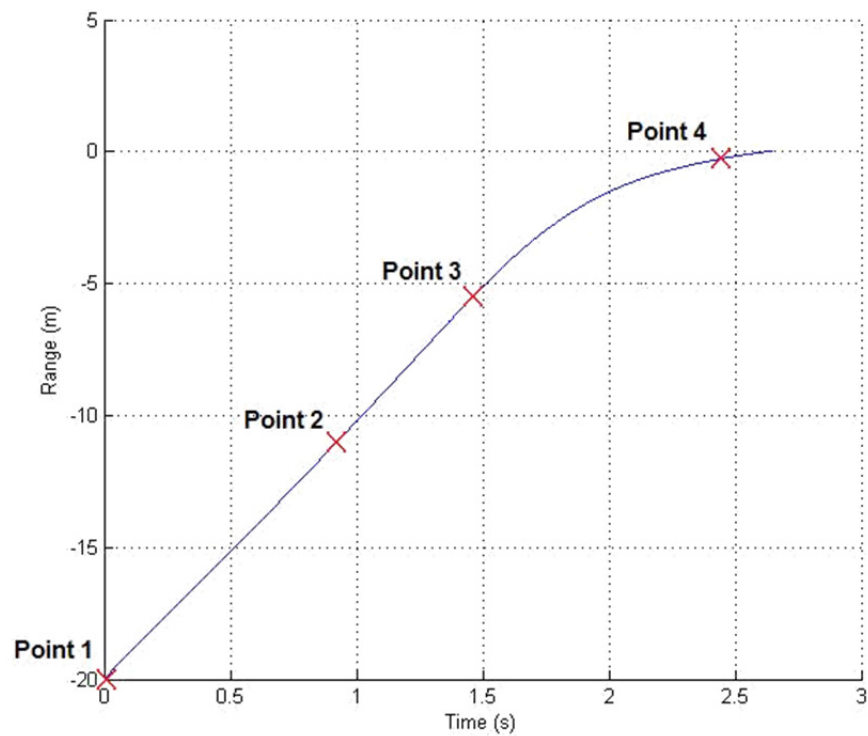


Figure 21: Perching Maneuver: Range vs. Time

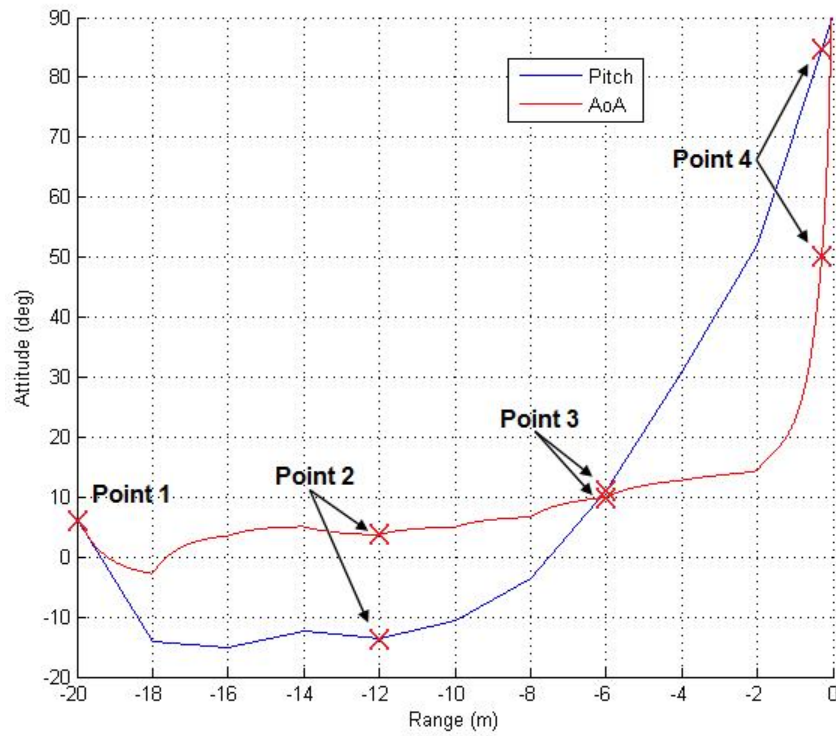


Figure 22: Perching Maneuver: Attitude vs. Range

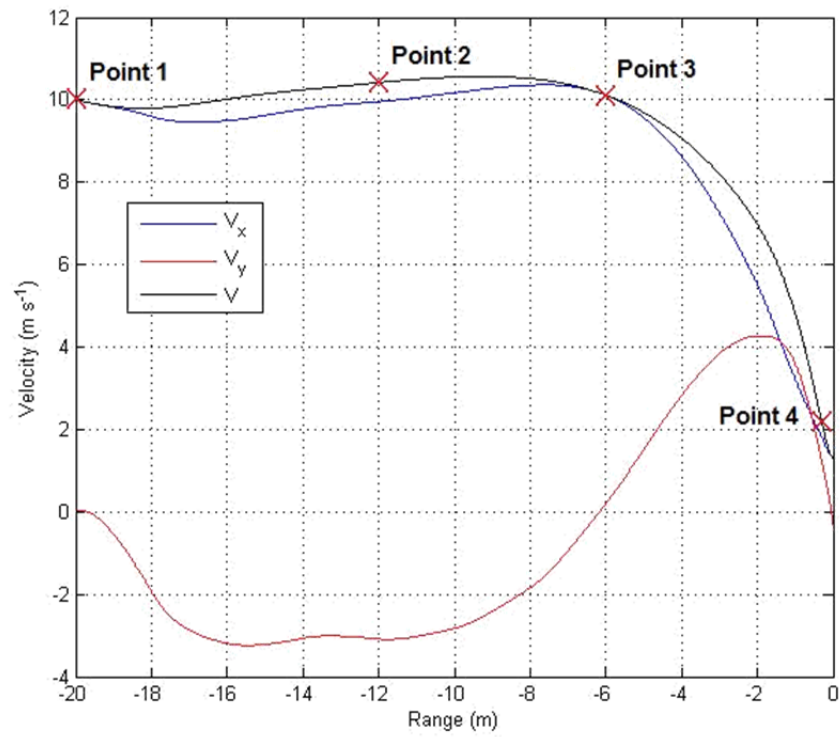


Figure 23: Perching Maneuver: Velocity vs. Range

Table 2: Data for Selected Points along Perching Maneuver

Selected Location:		Point 1	Point 2	Point 3	Point 4
Range	m	-20	-12	-6	-0.31
Altitude	m	5	3	1.78	4.80
Time	s	0	0.92	1.46	2.44
Velocity	m/s	10	10.41	10.11	2.19
AOA	°	6	3.75	10	50
AOA Rate	°/s	-98.92	0	14.6	216.2
Pitch Rate	°/s	-98.82	0	68.3	26.4

2.3.2 Force Estimation

With the geometry and flight conditions selected, a method for estimating the wing loading was established. A vortex lattice program developed in MATLAB called “Tornado” [21] was the product of the Master’s thesis referred to in Reference [22]. Figure 24 shows the main menu of Tornado.

The first menu item allows the user to define a new geometry or load one of the many existing wings. A new geometry is built by defining any number of wing partitions in the same manner as Figure 8 with the parameters given in Table 2. Thus, the vortex panel meshes and the finite element meshes were created to be identical to one another. The geometries of the fictitious sweeping mechanism shown in Figure 11 through Figure 14 were created in this manner with “flat plate” airfoils. Next, the flight conditions of the four points selected in Table 2 were created and saved in menu item 2. The lattice was then generated with menu item 5, where the fixed wake, standard vortex lattice method was selected. Figure 25 shows a sample geometry output, and Figure 26 shows the vortex panels generated for the sample output.

```

TORNADO Version 135 Release version
build 2010 03 20 14:07 UTC
Main Menu

Input operations.
[1]. Aircraft geometry setup
[2]. Flight condition setup
[3]. Change rudder setting
[4]. Move reference point

Lattice operations.
[5]. Generate lattice.

Computation operations.
[6]. Processor access

Post processing and interactive operations.
[7]. Post processing, Result/Plot functions
[8]. Keyboard access

Auxiliary operations.
[10]. About / Release Info
[100]. Help files
[0]. Exit Tornado

Please enter choice from above:

```

Figure 24: Main Menu of Tornado Software

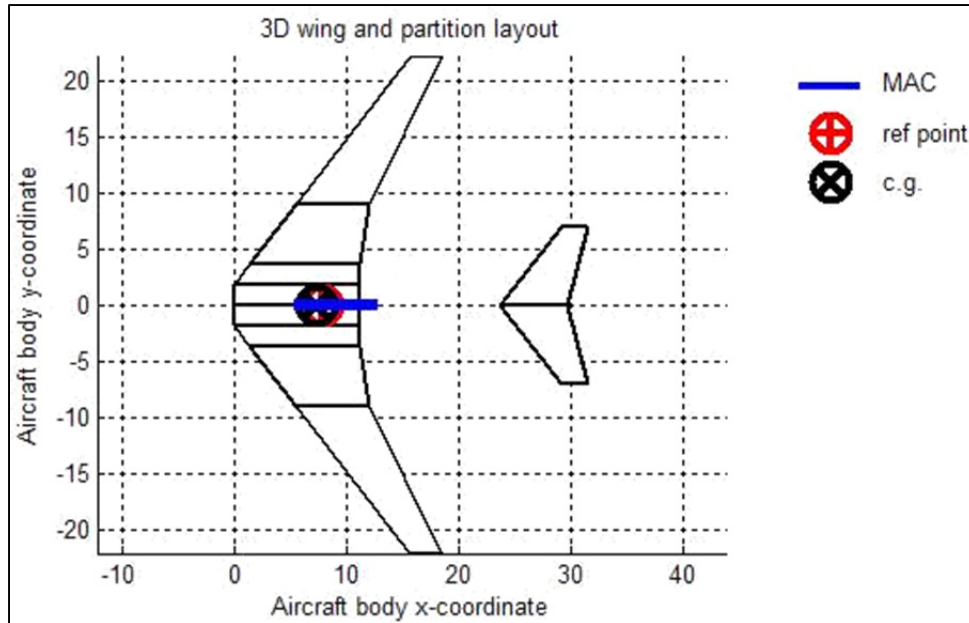


Figure 25: Example of Tornado Geometry Output [21]

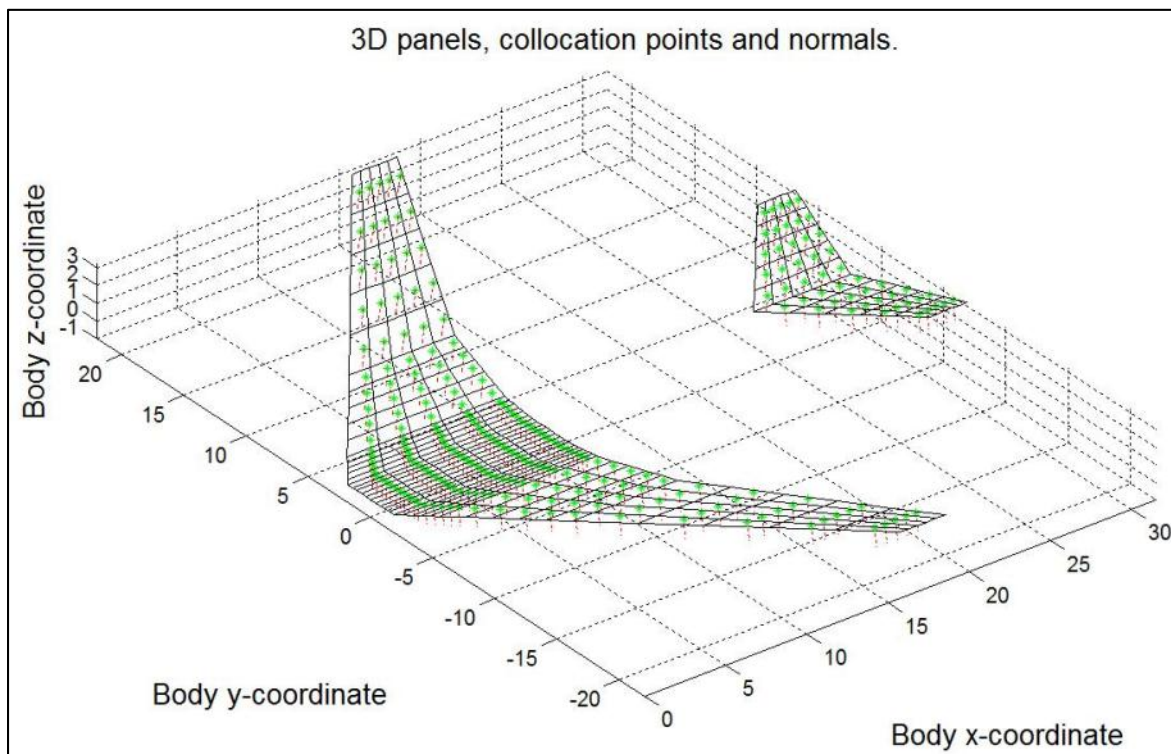


Figure 26: Example of Tornado Vortex Panels Output [22]

In light of the several processing options given in menu item 6, only static computations at the specified flight states were performed. Tornado outputs five different MATLAB structures: geo, state, lattice, ref, and results. The geo and state structures simply return the geometry and flight conditions defined by the user. The lattice structure returns the mesh data. The ref structure is not useful, since the mean

aerodynamic chord and center of gravity location are only needed for full aircraft analysis. The pertinent data is reported in the results structure, which gives three column vectors of the x, y, and z force components acting on each panel. Since vortex lattice methods are inherently inviscid, an alternative method for viscous drag estimation was made. An auxiliary processing option was added to the current version of Tornado to predict zero-lift, flat-plate drag, which gives an estimate of the skin friction drag C_{D0} . For the perching maneuver, the form drag due to flow separation as the MAV exceeds the stall angle of attack has an even bigger impact on the wing loading, since at 90° , the loading is almost entirely due to drag. (Although it should be noted that drag loading is still a bending load, as is the lift loading at low angles of attack). Therefore to estimate the form drag as it varies with angle of attack, the following equation was used:

$$D = q_\infty S [C_{D0} + (1 - C_{D0}) \sin \alpha] \quad (80)$$

where q_∞ is the dynamic freestream pressure, S is the planform area, and α is the angle of attack. The effect of Eq. (80) is shown in Figure 27. In this fashion, the drag is exactly equal to the zero-lift drag prediction at 0° angle of attack. At 90° angle of attack or when C_{D0} is equal to one, the drag is equal to $q_\infty S$, as C_D equal to one implies.

To apply the aerodynamic forces calculated from Tornado to the finite element model, the single resultant force per each panel calculated by the vortex lattice method needed to be divided onto the nodes of the given element. Since the locations of the resultant force acting on each panel were not known, the forces were assumed to act through the centroid of the element.

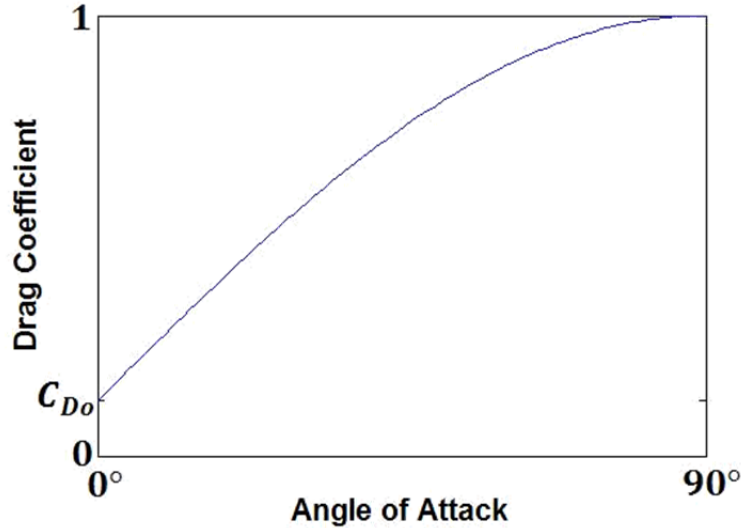


Figure 27: Viscous Drag Estimation Curve

Following this assumption, one fourth of each of the three components of the force vector was applied to the four nodes of the element. Thus at each node, one quarter of the force acting through each of the adjacent elements to that node were added together. To distribute the estimated drag force over the nodes, the total estimated drag was first divided among the chords, weighting the division by the local chord length. Then, the component of the total drag for a given chord was distributed evenly among the nodes

along that chord. In this manner, the estimated drag force at each node was then added to the lift and inviscid drag loads calculated by Tornado.

2.4 Optimization

2.4.1 Compliance Objective Using the SIMP Model

In structural topology, the maximum stiffness or rigidity of a structure is often sought by distributing a limited amount of material throughout the design domain. In this pursuit, a common restatement of the maximum stiffness objective is minimization of flexibility. The basic relationship of flexibility to rigidity can be seen with the fundamental linear spring in elementary mechanics, where the flexibility is simply the reciprocal of the spring stiffness.

In order to minimize the flexibility of a structure, a suitable measure of flexibility must be selected to formulate the objective of an optimization problem. Though there are a number of measures of flexibility, the compliance of a structure will be used here. Compliance can be thought of as the strain energy [18] in a deformed solid body. Provided no energy is gained or lost in the form of heat, the work required to deform a body is equivalent to the strain energy of that body in its deformed state. Work is, of course, the product of force and displacement. Thus, for a discrete finite element formulation, compliance is simply $\{F\}^T \{d\}$, where $\{d\}$ are the nodal displacements and $\{F\}$ are the external forces at the nodes (see References [23] and [24] for a continuous formulation of compliance). Using compliance as a measure of flexibility has the advantage that it is a convex function of the design variables, whereas a measure such as $\{d\}^T \{d\}$ is a nonconvex function of the design variables. Also, a body where compliance has been minimized will have the same specific strain energy in each element.

Though the flexible skin process summarized in Section 2.2 suggested that skin design should include Young's modulus, shear modulus, thickness, and possibly Poisson's ratio in the design variables, only element thickness is considered here in the design variables as a simpler starting point. Thus, for a finite element discretization with N elements, the design variables are given in the vector

$$\{\rho\} = \left\{ \rho_1 \quad \rho_2 \quad \dots \quad \rho_e \quad \dots \quad \rho_N \right\}^T \quad (81)$$

where ρ_e is the thickness of element e . It will be discussed later whether only including element thickness in the design variables leads to results that can be correlated to skin design.

With the stated objective and design variables, the design constraints must now be specified. The nodal displacements $\{d\}$ in the objective function will be solved by the finite element method (Eq. (75)), and therefore a simultaneous optimization formulation includes Eq. (74), repeated here, as a constraint.

$$\{F\} = [K]\{d\} \quad (82)$$

Substituting in Eq. (72) in for the global stiffness $[K]$ gives

$$\{F\} = \left(\sum_{e=1}^N [k_e] \right) \{d\} \quad (83)$$

As stated in the opening sentence of this section, compliance minimization is only beneficial if a limit on the material distributed throughout the design domain Ω is imposed. In the absence of such a constraint, compliance minimization would simply lead to infinite thickness throughout the entire design domain; but with a limited volume V of material, the optimization must “economize” the material distribution. Expressing the material constraint as an inequality gives:

$$\sum_{e=1}^N \rho_e a_e \leq V \quad (84)$$

where a_e is the area of element e . In matrix form, this constraint is

$$\{\rho\}^T \{a\} - V \leq 0 \quad (85)$$

Additionally, for a physical solution to occur, the design variables must be confined by an upper and lower bound.

$$0 < \rho_{min} \leq \rho_e \leq \rho_{max}, \quad e = 1, \dots, N \quad (86)$$

Though ρ_{min} and ρ_{max} can be considered inequality constraints, most optimization solution methods take into account optimization variable bounds without explicitly adding them as constraints. Design variable bounds are sometimes referred to as “box” constraints.

Putting the objective function and constraints together, a simultaneous compliance minimization with two constraints is given by

$$\begin{aligned} \min_{\rho, d(\rho)} \quad & \{F\}^T \{d\} \\ \text{s.t.} \quad & \left(\sum_{e=1}^N [k_e] \right) \{d\} = \{F\}, \\ & \{\rho\}^T \{a\} - V \leq 0, \quad 0 < \rho_{min} \leq \rho_e \leq \rho_{max}, \quad e = 1, \dots, N \end{aligned} \quad (87)$$

A better programmatic formulation of the problem is to nest the equilibrium constraint in the compliance objective, thus making the objective statement a function in the design variables only, and not in $d(\rho)$ as well. This also reduces the number of constraints down to the single material constraint.

$$\begin{aligned} \min_{\rho} \quad & c(\rho) \\ \text{s.t.} \quad & \{\rho\}^T \{a\} - V \leq 0, \quad 0 < \rho_{min} \leq \rho_e \leq \rho_{max}, \quad e = 1, \dots, N \end{aligned} \quad (88)$$

where the compliance, c , is given as

$$c(\rho) = \{F\}^T \{d\}, \quad \text{where } \{d\} \text{ solves: } \left(\sum_{e=1}^N [k_e] \right) \{d\} = \{F\} \quad (89)$$

While the values of the design variables are allowed to range between ρ_{\min} and ρ_{\max} , the optimization problem of Eq. (88) is really a sizing problem, as defined in Section 1.2. In a topology design, the optimal placement of a material within the design domain Ω is desired such that points in space will either have material or they will be void. In this case, the structural geometry is rendered as a black and white image, albeit pixelated due to the finite element discretization. Thus topology optimization is seeking to determine the optimal subset Ω^{mat} of material points. Ideally, the element stiffness matrices would be defined piecewise over the domain Ω in the following manner:

$$[k(x)] = 1_{\Omega^{\text{mat}}}(x)[k_e(x)], \quad 1_{\Omega^{\text{mat}}}(x) = \begin{cases} 1 & : x \in \Omega^{\text{mat}} \\ 0 & : x \in \Omega \setminus \Omega^{\text{mat}} \end{cases} \quad (90)$$

where $[k_e(x)]$ indicates that the element stiffness matrix varies over the domain. In this distributed, discrete 0-1 problem, the material constraint is represented as

$$\int_{\Omega} 1_{\Omega^{\text{mat}}} d\Omega = \text{Vol}(\Omega^{\text{mat}}) = V \quad (91)$$

Unfortunately, a number of problems arise with the character of a discrete problem; allowing finite elements to have zero stiffness leads to singularities in the solution process. Also, optimization algorithms where design variables take only discrete values are not efficient for large-scale problems with lots of variables. Thus, a model that allows intermediate values in the design variables but also penalizes them, the so-called Solid Isotropic Material with Penalization (SIMP) model, is used.

In the SIMP model, the constitutive matrix is directly penalized. For the membrane element, the constitutive matrix (Eq. (24)) takes the form

$$[D] = \frac{\rho^q E t}{1 - \nu^2} \begin{bmatrix} 1 & \nu & 0 \\ \nu & 1 & 0 \\ 0 & 0 & \frac{1 - \nu}{2} \end{bmatrix} \quad (92)$$

where the penalty q is some constant (typically ≥ 1). Since the upper bound ρ_{\max} is set to 1, the physical thickness t is still included in the constitutive matrix such that when an element is fully present ($\rho = 1$), the actual physical thickness is scaled by t . The quantity ρ^q can be thought of as the “effective” thickness. To avoid numerical problems induced by zero stiffness, the lower bound on the thickness is $\rho_{\min} = \varepsilon \approx 0$ ($\varepsilon = 0.001$ is typical). Figure 28 shows the effect the choice of exponent q has on penalization. When $q = 1$, the stiffness of an element is proportional to the amount of material designated to that element, and hence the thicker an element is, the stiffer it becomes. This is not the case for $q > 1$. Putting some values to Figure 28, at half the available material ($\rho = 0.5$), the effective thickness is only about 0.2 for $q = 3$. In this case, the effective thickness does not reach one half until a ρ of about 0.8. What choice of exponent q performs the best is a matter of numerical experimentation.

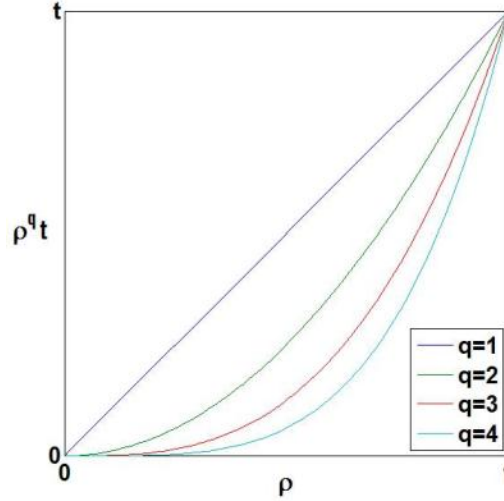


Figure 28: SIMP Penalization of Element Thickness

However, Bendsøe and Sigmund point out [23] that in order for a material to be realizable from a 2-D SIMP model, q must satisfy the following relationship with Poisson's ratio:

$$q \geq \max \left\{ \frac{2}{1-\nu}, \frac{4}{1+\nu} \right\} \quad (93)$$

Thus, for a material with $\nu = 1/3$, the smallest q is 3. In fact, $q = 3$ has been found to be a good choice for the exponent, and will be used here unless otherwise stated. For a plate bending element, the constitutive matrix (Eq. (37)) reveals that the element stiffness already has cubic dependence on the thickness. This implies that the optimal design naturally prefers to achieve either the upper or lower bound on thickness, and an additional penalty need not be imposed (consult Reference [23] for more information).

Rather than keep the design variables in the constitutive matrix, the global stiffness matrix can be more readily seen as a function of the design variables when they are placed outside of the element stiffness matrix:

$$[K] = \left(\sum_{e=1}^N \rho_e^q [k_e] \right) \quad (94)$$

With the amendment to the compliance objective with the SIMP model, the optimization statement is modified slightly.

$$\begin{aligned} \min_{\rho} \quad & c(\rho) \\ \text{s.t.} \quad & \{\rho\}^T \{a\} - V \leq 0, \quad \varepsilon \leq \rho_e \leq 1, \quad e = 1, \dots, N \end{aligned} \quad (95)$$

where the compliance is given as

$$c(\rho) = \{F\}^T \{d\}, \quad \text{where } \{d\} \text{ solves: } \left(\sum_{e=1}^N \rho_e^q [k_e] \right) \{d\} = \{F\} \quad (96)$$

Once $\{d\}$ has been calculated from the finite element method, a substitution can be made for the global force vector $\{F\}$ such that

$$c(\rho) = \{d\}^T \left(\sum_{e=1}^N \rho_e^q [k_e] \right)^T \{d\} \quad (97)$$

The total compliance can be computed by summing up the compliance of each element, much in the same way that the direct stiffness method adds element stiffnesses and forces together to obtain the global stiffness and force vectors. Thus Eq. (97) becomes

$$c(\rho) = \sum_{e=1}^N c_e(\rho_e) = \sum_{e=1}^N \rho_e^q \{d_e\}^T [k_e]^T \{d_e\} \quad (98)$$

The Karush-Kuhn Tucker (KKT) optimality conditions [25], which give the first-order necessary conditions, are now derived for the compliance minimization of Eq. (95). The Lagrangian function is given as

$$\mathcal{L}(\rho, \lambda) = c(\rho) + \lambda (\{\rho\}^T \{a\} - V + s^2) \quad (99)$$

where λ is the Lagrange multiplier for the single volume constraint, and s is the slack variable for the inequality constraint. A formal derivation of the compliance gradient with respect to the design variables is given in Reference [24], where both a direct analytical method and the adjoint analytical method are employed to attain the following:

$$\frac{\partial c_e}{\partial \rho_e} = 2\{d_e\}^T \frac{\partial \{f_e\}}{\partial \rho_e} - \{d_e\}^T \frac{\partial [k_e]^T}{\partial \rho_e} \{d_e\} \quad (100)$$

The first term in Eq. (100) is only included when the global force vector is a function of the design variables, for example, when the weight of the structure is included in the loading. With the modification of $[k_e]$ by the SIMP model and excluding thickness dependency of the loading, the compliance sensitivity reduces to

$$\frac{\partial c_e}{\partial \rho_e} = -q\rho_e^{q-1} \{d_e\}^T [k_e]^T \{d_e\} \quad (101)$$

The gradient condition for the design variables thus becomes

$$\frac{\partial \mathcal{L}}{\partial \rho_e} = -q\rho_e^{q-1} \{d_e\}^T [k_e]^T \{d_e\} + \lambda \rho_e a_e = 0, \quad e = 1, \dots, N \quad (102)$$

and the volume constraint is recovered from the gradient condition

$$\frac{\partial \mathcal{L}}{\partial \lambda} = \{\rho\}^T \{a\} - V + s^2 = 0 \quad (103)$$

A feasibility check on the inequality requires that

$$s^2 \geq 0. \quad (104)$$

The switching conditions are derived from the derivative of the Lagrangian function with respect to the slack variable.

$$\lambda_s = 0 \quad (105)$$

Finally, the Lagrange multiplier is required to be nonnegative since it is associated with an inequality.

$$\lambda \geq 0 \quad (106)$$

The KKT conditions produce enough equations for the unknowns and, in theory, the equations could be solved simultaneously. However, the nested compliance optimization problem has been shown to be convex [24] (although the simultaneous formulation is not) and can therefore take advantage of convex algorithms.

2.4.2 Optimality Criteria Method

Though there are many ways to solve the compliance optimization problem, a general procedure for solving the nested formulation using first order algorithms is described in the following steps:

1. Start with an initial design ρ^0 and set the iteration counter $k = 0$. A typical initial design is $\rho^0 = \text{Vol}(\Omega^{\text{mat}})/\text{Vol}(\Omega)$.
2. Perform a finite element analysis for the current design, solving for the displacement vector $d(\rho^k)$ from the equilibrium condition $K(\rho^k)d(\rho^k) = F$.
3. For the current iteration, calculate the compliance $c(\rho^k)$, the constraint function $(\rho^k)^T a - V$, and the corresponding sensitivities.
4. Evaluate an appropriate update scheme (i.e., by solving an explicit, convex approximation) to give a new design ρ^{k+1} .
5. Update the counter $k = k + 1$ and return to step 2 unless a stopping criteria has been met.

Step 4 provides leeway in selecting an update scheme for the design variables and indeed, there are many, such as SLP [25], SQP [25], CONLIN [24], and MMA [26]. However, the Optimality Criteria (OC) method is a historically older, classical approach that can be seen as a special case of the explicit convex approximation method, and has turned out to be very efficient at solving topology optimization problems.

A more descriptive presentation of the OC method is given in Reference [24], but only a brief description is presented here. The OC method takes advantage of the fact that the material volume is a monotonically decreasing function of the Lagrange multiplier λ . Hence, a stationary point is achieved when the volume constraint is satisfied. The update of the design variables is calculated by

$$\rho_e^{k+1} = \min \left\{ \max \left[\rho_e^k \left(\frac{q \rho_e^{q-1} (d_e^k)^T k_e^T d_e^k}{\lambda a_e} \right)^\eta, \rho_{\min} \right], \rho_{\max} \right\} \quad (107)$$

such that the volume constraint

$$\sum_{e=1}^N a_e \rho_e^{k+1}(\lambda) - V = 0 \quad (108)$$

is satisfied, where ρ_e^{k+1} is now a function of λ . The update scheme can be written a little more compactly by substituting the compliance sensitivity (Eq. (101)) into Eq. (107).

$$\rho_e^{k+1} = \min \left\{ \max \left[\rho_e^k \left(-\frac{\partial c_e / \partial \rho_e}{\lambda a_e} \right)^\eta, \rho_{min} \right], \rho_{max} \right\} \quad (109)$$

In this manner, each thickness is updated independently. The min and max functions are used so that the box constraints are not violated. The exponent η acts like a damping knob on the update process and is chosen by experiment (a value of 0.5 is typical). Note that the design has converged when the quantity in parenthesis is equal to unity, or if

$$\frac{q \rho_e^{\eta-1} (\mathbf{d}_e^k)^T \mathbf{k}_e^T \mathbf{d}_e^k}{a_e} = \lambda = \text{constant}, \quad \text{for all } e = 1, \dots, N \quad (110)$$

This quantity is twice the specific strain energy of an element. The implication of Eq. (110) is that the OC method is closely related to a fully stressed design, where all elements have the same strain energy, and therefore the same stress. However, with the penalization method, the specific strain energy is only constant for elements with intermediate densities, since it is lower in regions with $\rho = \rho_{min}$ and higher in regions with $\rho = \rho_{max}$. The design update does however add material to elements with a specific strain energy higher than λ , and it removes material from elements with a specific strain energy lower than λ , assuming the bounds on ρ are not violated.

A bi-sectioning routine is used to implement Eqs. (108) and (109). First, an upper and a lower bound on the Lagrange multiplier are selected, for example, $\lambda_{upp} = 100,000$ and $\lambda_{low} = 0$. Next, the middle point between those bounds is set as λ_{mid} . The update is computed with Eq. (109) using λ_{mid} . The volume constraint is then checked with the updated variables. If the constraint is violated with excessive material, then the lower bound is set to λ_{mid} , and if the constraint is violated with an inadequate amount of material, then the upper bound is set to λ_{mid} . This process continues until the value of λ is found within a certain tolerance which yields a design update that satisfies the volume constraint.

An example output is shown in Figure 29 where the rectangular design domain topology, representing the right wing of an aircraft, has been optimized for an in-plane load applied at the upper, right-hand corner of the domain. The boundary conditions are fixed such that the root chord is clamped.

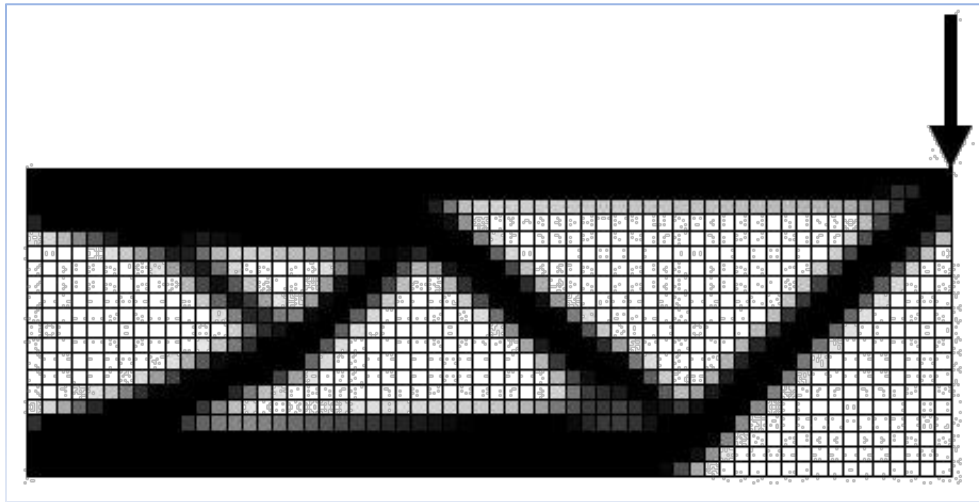


Figure 29: Example “SIMP” Output

As a final note, several complications can arise with the formulation given in this section. A common one that severely inhibits a good solution is that of the so-called checkerboard pattern. A checkerboard pattern occurs when the design function alternates between 0 and 1 and produces a numerically artificial stiffness. This problem is described in detail in Reference [23]. Sigmund devised a mesh-independency filter in his 99-line code for the compliance sensitivities that also eliminates the checkerboard pattern. Only one additional parameter used for specifying the radius of the filter is added to the method. A radius of less than 1 indicates the filter is turned off. The problem in Figure 29 is repeated again in Figure 30, displaying the erroneous results that occur when the checkerboard filter is turned off. A detailed investigation of the influence of each of the parameters on solution convergence is discussed in Reference [7].



Figure 30: Example “SIMPm” Output with No Checkerboard Filter.

2.5 Substructure and Actuation Optimization

Morphing structures are comprised of active and inactive components that work together to generate the desired shape change in the structure. Active components, such as linear and rotational actuators, convert energy to motion to perturb the structure. Inactive components, such as variously compliant beams and joints, guide the structure towards the final shape and provide the necessary structural rigidity. Since the objective of this energy based design of the substructure and actuation system is to minimize the amount of actuation energy required to achieve the desired shape change within a flight environment, the influence of external forces must be included in the analysis model. This chapter focuses on the development of the analysis model used in the optimization routine and provides insight into element formulation, model kinematics, and external force estimation.

In order to properly represent the design space for a morphing structures actuation system, an innovative approach to finite element models must be conceived. This model must facilitate the designation of actuators, rigid and compliant beams, rigid and compliant joints, and even voided elements within the design space. The formulation of the model must be general enough such that elements can take the form of any combination of active or inactive components.

The model kinematics must represent the motion of the morphing structure as accurately as possible. Simplifying loads due to actuators as static loads is not acceptable since the static loads will not take into

account the rotation of the actuators as the structure changes shape; however, a dynamic finite element method is not conducive for the analysis model since it will be solved many times during the optimization routine. Therefore, a modified static finite element method must be used to provide a better approximation of the morphing motion.

To model the external forces on the structure, an accurate but quickly solvable aerodynamic code must be used. For this reason, a vortex lattice method (VLM) is used to quickly calculate the external aerodynamic forces acting on the structure. These forces are then splined to the structure and additional information is used to provide a static aeroelastic analysis.

2.5.1 Elements

The mesh and connectivity information is used to define the substructure elements within the model. These elements can be classified as either line elements, joint elements, or attachment elements as shown in Figure 31.

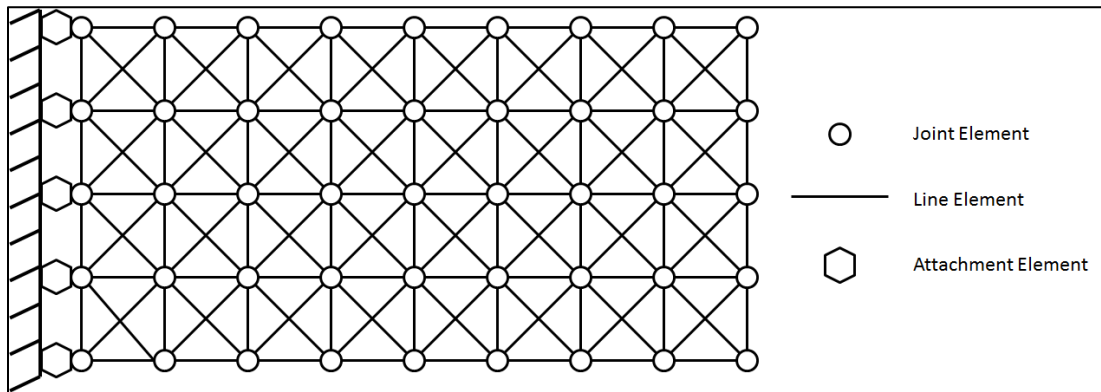


Figure 31: Model Element Designation

2.5.1.1 Line Elements

The foundation of all line element configurations is the classic Euler-Bernoulli beam element. Line elements can take on various configurations depending on the values of their associated design variables. Examples of these configurations, presented in Figure 32, include frames, trusses, inactive telescopes, active telescopes, actuators, and voids.

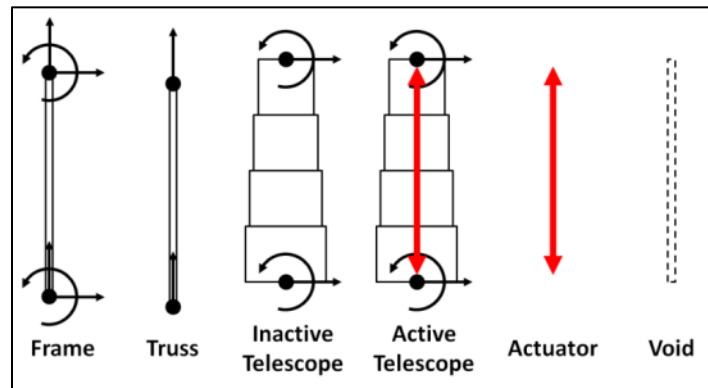


Figure 32: Line Element Configurations

- *Frame elements* are classic Euler-Bernoulli beam elements that exhibit both axial and bending stiffness.
- *Truss elements* are classic elements that exhibit only axial stiffness.
- *Inactive telescopic elements* are elements that exhibit a very low axial stiffness allowing them to extend and contract when external loads are applied; however, they also exhibit a meaningful bending stiffness.
- *Active telescopes* are similar to inactive telescopes except they also provide an actuator force.
- *Actuator elements* exhibit neither axial nor bending stiffness and provide only an actuator force.
- *Void elements* exhibit neither axial nor bending stiffness and they do not provide an actuator force.

All line elements are subject to a maximum allowable stroke constraint to prohibit them from extending or contracting an unrealistic amount. Additionally, actuator type elements are subjected to a predefined maximum force. Formulation details of these configurations are presented in the following section.

2.5.1.2 Joint Elements

The foundation for all joint elements is the rotational spring element. Joint elements can vary their rotational stiffness through the values of their associated design variables. Depending on the stiffness of the spring, the joint element can be classified as revolute joints, compliant joints, or semi-rigid joints. Examples of these configurations are presented in Figure 33.

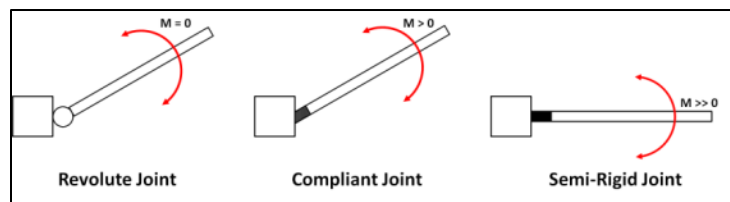


Figure 33: Joint Element Configurations

- *Revolute joints* are joint elements with very low rotational stiffness. These joints are hinges and are not able to support moments.
- *Compliant joints* are joint elements with moderate rotational stiffness and are able to support moments at the cost of high rotational strain. These joints are best described as spring hinges.
- *Semi-rigid joints* are joint elements with very high rotational stiffness. These joints are essentially fixed.

2.5.1.3 Attachment Elements

Attachment elements are basically line elements at the boundary between the wing and the fuselage. These elements are oriented such that the axial direction is parallel to the fuselage. Constraints on the elements degrees of freedom are set such that the element is not able to penetrate the fuselage. Further discussion on the formulation of attachment elements is detailed in the following section.

2.5.2 Element Formulation

As previously mentioned, in order to properly represent the design space for morphing structures, an innovative approach to finite element models must be conceived. This single element or a multitude of elements must be able to accommodate any form of line or joint configuration within the design space. This section focuses on the formulation of the element used in the analysis model which is not only able

to accommodate all combinations of line and joint configurations, but also decreases the solution time of the model.

2.5.2.1 Line Element

The foundation for the line element is the Euler-Bernoulli beam element. This element, combined with design variables, ρ_{11} and ρ_{12} , multiplied to the axial and non-axial portion of the element stiffness matrix, respectively, is able to accommodate all of the various line element configurations (see Eq. (111)). The design variables are constrained to values between zero and one, which effectively changes the stiffness of that element to a percentage of the total stiffness. For instance, if the design variable ρ_{11} has a very small value and ρ_{12} has a value of one, then the element has low axial stiffness, but high bending stiffness and could be an inactive or active telescope.

$$\begin{Bmatrix} F_{xi} \\ F_{yi} \\ M_{zi} \\ F_{xj} \\ F_{yj} \\ M_{zj} \end{Bmatrix} = \begin{bmatrix} \frac{EA\rho_{11}^p}{L} & 0 & 0 & -\frac{EA\rho_{11}^p}{L} & 0 & 0 \\ 0 & \frac{12\rho_{12}^p EI_z}{L^3} & \frac{6\rho_{12}^p EI_z}{L^2} & 0 & -\frac{12\rho_{12}^p EI_z}{L^3} & \frac{6\rho_{12}^p EI_z}{L^2} \\ 0 & \frac{6\rho_{12}^p EI_z}{L^2} & \frac{4\rho_{12}^p EI_z}{L} & 0 & -\frac{6\rho_{12}^p EI_z}{L^2} & \frac{2\rho_{12}^p EI_z}{L} \\ -\frac{EA\rho_{11}^p}{L} & 0 & 0 & \frac{EA\rho_{11}^p}{L} & 0 & 0 \\ 0 & -\frac{12\rho_{12}^p EI_z}{L^3} & -\frac{6\rho_{12}^p EI_z}{L^2} & 0 & \frac{12\rho_{12}^p EI_z}{L^3} & -\frac{6\rho_{12}^p EI_z}{L^2} \\ 0 & \frac{6\rho_{12}^p EI_z}{L^2} & \frac{2\rho_{12}^p EI_z}{L} & 0 & -\frac{6\rho_{12}^p EI_z}{L^2} & \frac{4\rho_{12}^p EI_z}{L} \end{bmatrix} \begin{Bmatrix} u_i \\ v_i \\ \theta_{zi} \\ u_j \\ v_j \\ \theta_{zj} \end{Bmatrix} \quad (111)$$

2.5.2.2 Joint Element

The foundation for the joint element is simple rotational spring element which solely has rotational stiffness. This element is combined with a design variable much like the line element, which is constrained to values between zero and one (see Eq. (112)).

$$\begin{Bmatrix} M_{zi} \\ M_{zj} \end{Bmatrix} = \begin{bmatrix} k\rho_{j1}^\beta & -k\rho_{j1}^\beta \\ -k\rho_{j1}^\beta & k\rho_{j1}^\beta \end{bmatrix} \begin{Bmatrix} \theta_{zi} \\ \theta_{zj} \end{Bmatrix} \quad (112)$$

2.5.2.3 Condensed Element

What makes this element formulation unique and favorable to this type of analysis is how the individual line and joint elements are condensed into a single element stiffness matrix. This process is formally known as Guyan Reduction [27].

Figure 34 represents how typical analyses using beam and rotational spring elements would be modeled. This system requires four different nodes to fully define the design space. Notice the axial DOF is absent from this derivation since it is not coupled to and therefore has no effect on the non-axial portions of the element stiffness matrix.

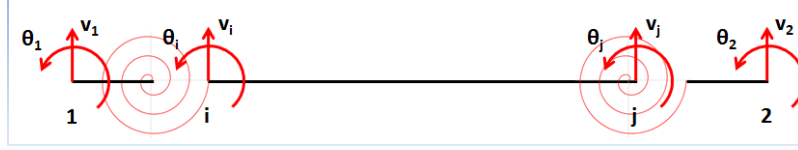


Figure 34: Typical Joint-Beam-Joint Model

Setting $k_1 = \alpha_1 \frac{EI_z}{L}$ and $k_2 = \alpha_2 \frac{EI_z}{L}$, the stiffness matrix for each component can be formulated:

$$\begin{Bmatrix} M_{z1} \\ M_{zi} \end{Bmatrix} = \begin{bmatrix} \frac{EI_z \alpha_1}{L} & -\frac{EI_z \alpha_1}{L} \\ -\frac{EI_z \alpha_1}{L} & \frac{EI_z \alpha_1}{L} \end{bmatrix} \begin{Bmatrix} \theta_{z1} \\ \theta_{zi} \end{Bmatrix} \quad (113)$$

$$\begin{Bmatrix} F_{yi} \\ M_{zi} \\ F_{yj} \\ M_{zj} \end{Bmatrix} = \begin{bmatrix} \frac{12\rho_{l2}^p EI_z}{L^3} & \frac{6\rho_{l2}^p EI_z}{L^2} & -\frac{12\rho_{l2}^p EI_z}{L^3} & \frac{6\rho_{l2}^p EI_z}{L^2} \\ \frac{6\rho_{l2}^p EI_z}{L^2} & \frac{4\rho_{l2}^p EI_z}{L} & -\frac{6\rho_{l2}^p EI_z}{L^2} & \frac{2\rho_{l2}^p EI_z}{L} \\ -\frac{12\rho_{l2}^p EI_z}{L^3} & -\frac{6\rho_{l2}^p EI_z}{L^2} & \frac{12\rho_{l2}^p EI_z}{L^3} & -\frac{6\rho_{l2}^p EI_z}{L^2} \\ \frac{6\rho_{l2}^p EI_z}{L^2} & \frac{2\rho_{l2}^p EI_z}{L} & -\frac{6\rho_{l2}^p EI_z}{L^2} & \frac{4\rho_{l2}^p EI_z}{L} \end{bmatrix} \begin{Bmatrix} v_i \\ \theta_{zi} \\ v_j \\ \theta_{zj} \end{Bmatrix} \quad (114)$$

$$\begin{Bmatrix} M_{zj} \\ M_{z2} \end{Bmatrix} = \begin{bmatrix} \frac{EI_z \alpha_2}{L} & -\frac{EI_z \alpha_2}{L} \\ -\frac{EI_z \alpha_2}{L} & \frac{EI_z \alpha_2}{L} \end{bmatrix} \begin{Bmatrix} \theta_{zj} \\ \theta_{z2} \end{Bmatrix} \quad (115)$$

Where, α_1 and α_2 are functions of the design variables associated with the rotational spring. If, α_i equals zero, then the joint is a hinge joint; however, if α_i approaches infinity, then the joint is fixed joint. Details of these functions are discussed later in this section.

From equilibrium requirements, F_{y1} equals F_{yi} and F_{y2} equals F_{yj} , and from compatibility requirements, v_1 equals v_i and v_2 equals v_j , the stiffness relationships for the entire system can be assembled:

$$\begin{Bmatrix} M_{zi} \\ M_{zj} \\ F_{y1} \\ M_{z1} \\ F_{y2} \\ M_{z2} \end{Bmatrix} = \begin{bmatrix} \frac{EI_z (4\rho_{l2}^p + \alpha_1)}{L} & \frac{2\rho_{l2}^p EI_z}{L} & \frac{6\rho_{l2}^p EI_z}{L^2} & -\frac{EI_z \alpha_1}{L} & -\frac{6\rho_{l2}^p EI_z}{L^2} & 0 \\ \frac{2\rho_{l2}^p EI_z}{L} & \frac{EI_z (4\rho_{l2}^p + \alpha_2)}{L} & \frac{6\rho_{l2}^p EI_z}{L^2} & 0 & -\frac{6\rho_{l2}^p EI_z}{L^2} & -\frac{EI_z \alpha_2}{L} \\ \frac{6\rho_{l2}^p EI_z}{L^2} & \frac{6\rho_{l2}^p EI_z}{L^2} & \frac{12\rho_{l2}^p EI_z}{L^3} & 0 & -\frac{12\rho_{l2}^p EI_z}{L^3} & 0 \\ -\frac{EI_z \alpha_1}{L} & 0 & 0 & \frac{EI_z \alpha_1}{L} & 0 & 0 \\ -\frac{6\rho_{l2}^p EI_z}{L^2} & -\frac{6\rho_{l2}^p EI_z}{L^2} & -\frac{12\rho_{l2}^p EI_z}{L^3} & 0 & \frac{12\rho_{l2}^p EI_z}{L^3} & 0 \\ 0 & -\frac{EI_z \alpha_2}{L} & 0 & 0 & 0 & \frac{EI_z \alpha_2}{L} \end{bmatrix} \begin{Bmatrix} \theta_{zi} \\ \theta_{zj} \\ v_1 \\ \theta_{z1} \\ v_2 \\ \theta_{z2} \end{Bmatrix} \quad (116)$$

To remove θ_{zi} and θ_{zj} , use the condensation Eq.(117).

$$[\hat{K}] = [K_{cc}] - [K_{cb}][K_{bb}]^{-1}[K_{bc}] \quad (117)$$

Where,

$$[K_{bb}] = \begin{bmatrix} \frac{EI_z (4\rho_{l2}^p + \alpha_1)}{L} & \frac{2\rho_{l2}^p EI_z}{L} \\ \frac{2\rho_{l2}^p EI_z}{L} & \frac{EI_z (4\rho_{l2}^p + \alpha_2)}{L} \end{bmatrix} \quad (118)$$

$$[K_{bc}] = [K_{cb}]^T = \begin{bmatrix} \frac{6\rho_{l2}^p EI_z}{L^2} & -\frac{EI_z \alpha_1}{L} & -\frac{6\rho_{l2}^p EI_z}{L^2} & 0 \\ \frac{6\rho_{l2}^p EI_z}{L^2} & 0 & -\frac{6\rho_{l2}^p EI_z}{L^2} & -\frac{EI_z \alpha_2}{L} \end{bmatrix} \quad (119)$$

$$[K_{cc}] = \begin{bmatrix} \frac{12\rho_{l2}^p EI_z}{L^3} & 0 & -\frac{12\rho_{l2}^p EI_z}{L^3} & 0 \\ 0 & \frac{EI_z \alpha_1}{L} & 0 & 0 \\ -\frac{12\rho_{l2}^p EI_z}{L^3} & 0 & \frac{12\rho_{l2}^p EI_z}{L^3} & 0 \\ 0 & 0 & 0 & \frac{EI_z \alpha_2}{L} \end{bmatrix} \quad (120)$$

The resulting element stiffness for the Joint-Beam-Joint configuration (sans axial stiffness) presented in Eq. (121) is:

$$\begin{bmatrix}
\frac{12\rho_{l2}^p EI_z (\rho_{l2}^p a_2 + \alpha_1 (\rho_{l2}^p + a_2))}{L^3 (4\rho_{l2}^p (3\rho_{l2}^p + a_2) + \alpha_1 (4\rho_{l2}^p + a_2))} & \frac{6\rho_{l2}^p EI_z \alpha_1 (2\rho_{l2}^p + a_2)}{L^2 (4\rho_{l2}^p (3\rho_{l2}^p + a_2) + \alpha_1 (4\rho_{l2}^p + a_2))} & -\frac{12\rho_{l2}^p EI_z (\rho_{l2}^p a_2 + \alpha_1 (\rho_{l2}^p + a_2))}{L^3 (4\rho_{l2}^p (3\rho_{l2}^p + a_2) + \alpha_1 (4\rho_{l2}^p + a_2))} & \frac{6\rho_{l2}^p EI_z (2\rho_{l2}^p + \alpha_1) a_2}{L^2 (4\rho_{l2}^p (3\rho_{l2}^p + a_2) + \alpha_1 (4\rho_{l2}^p + a_2))} \\
\frac{6\rho_{l2}^p EI_z \alpha_1 (2\rho_{l2}^p + a_2)}{L^2 (4\rho_{l2}^p (3\rho_{l2}^p + a_2) + \alpha_1 (4\rho_{l2}^p + a_2))} & \frac{4\rho_{l2}^p EI_z \alpha_1 (3\rho_{l2}^p + a_2)}{L (4\rho_{l2}^p (3\rho_{l2}^p + a_2) + \alpha_1 (4\rho_{l2}^p + a_2))} & -\frac{6\rho_{l2}^p EI_z \alpha_1 (2\rho_{l2}^p + a_2)}{L^2 (4\rho_{l2}^p (3\rho_{l2}^p + a_2) + \alpha_1 (4\rho_{l2}^p + a_2))} & \frac{2\rho_{l2}^p EI_z \alpha_1 a_2}{L (4\rho_{l2}^p (3\rho_{l2}^p + a_2) + \alpha_1 (4\rho_{l2}^p + a_2))} \\
-\frac{12\rho_{l2}^p EI_z (\rho_{l2}^p a_2 + \alpha_1 (\rho_{l2}^p + a_2))}{L^3 (4\rho_{l2}^p (3\rho_{l2}^p + a_2) + \alpha_1 (4\rho_{l2}^p + a_2))} & -\frac{6\rho_{l2}^p EI_z \alpha_1 (2\rho_{l2}^p + a_2)}{L^2 (4\rho_{l2}^p (3\rho_{l2}^p + a_2) + \alpha_1 (4\rho_{l2}^p + a_2))} & \frac{12\rho_{l2}^p EI_z (\rho_{l2}^p a_2 + \alpha_1 (\rho_{l2}^p + a_2))}{L^3 (4\rho_{l2}^p (3\rho_{l2}^p + a_2) + \alpha_1 (4\rho_{l2}^p + a_2))} & -\frac{6\rho_{l2}^p EI_z (2\rho_{l2}^p + \alpha_1) a_2}{L^2 (4\rho_{l2}^p (3\rho_{l2}^p + a_2) + \alpha_1 (4\rho_{l2}^p + a_2))} \\
\frac{6\rho_{l2}^p EI_z (2\rho_{l2}^p + \alpha_1) a_2}{L^2 (4\rho_{l2}^p (3\rho_{l2}^p + a_2) + \alpha_1 (4\rho_{l2}^p + a_2))} & \frac{2\rho_{l2}^p EI_z \alpha_1 a_2}{L (4\rho_{l2}^p (3\rho_{l2}^p + a_2) + \alpha_1 (4\rho_{l2}^p + a_2))} & -\frac{6\rho_{l2}^p EI_z (2\rho_{l2}^p + \alpha_1) a_2}{L^2 (4\rho_{l2}^p (3\rho_{l2}^p + a_2) + \alpha_1 (4\rho_{l2}^p + a_2))} & \frac{4\rho_{l2}^p EI_z (3\rho_{l2}^p + \alpha_1) a_2}{L (4\rho_{l2}^p (3\rho_{l2}^p + a_2) + \alpha_1 (4\rho_{l2}^p + a_2))}
\end{bmatrix} \quad (121)$$

To demonstrate how this element is able to adapt into all the desired configurations, some special cases are demonstrated below.

Rigid Joint- Stiff Beam-Rigid Joint ($\alpha_1 = \infty$; $\rho_{l2} = 1$; $\alpha_2 = \infty$)

$$\begin{bmatrix}
\frac{12EI_z}{L^3} & \frac{6EI_z}{L^2} & -\frac{12EI_z}{L^3} & \frac{6EI_z}{L^2} \\
\frac{6EI_z}{L^2} & \frac{4EI_z}{L} & -\frac{6EI_z}{L^2} & \frac{2EI_z}{L} \\
-\frac{12EI_z}{L^3} & -\frac{6EI_z}{L^2} & \frac{12EI_z}{L^3} & -\frac{6EI_z}{L^2} \\
\frac{6EI_z}{L^2} & \frac{2EI_z}{L} & -\frac{6EI_z}{L^2} & \frac{4EI_z}{L}
\end{bmatrix} \quad (122)$$

Pinned Joint- Stiff Beam-Rigid Joint ($\alpha_1 = 0$; $\rho_{l2} = 1$; $\alpha_2 = \infty$)

$$\begin{bmatrix}
\frac{3EI_z}{L^3} & 0 & -\frac{3EI_z}{L^3} & \frac{3EI_z}{L^2} \\
0 & 0 & 0 & 0 \\
-\frac{3EI_z}{L^3} & 0 & \frac{3EI_z}{L^3} & -\frac{3EI_z}{L^2} \\
\frac{3EI_z}{L^2} & 0 & -\frac{3EI_z}{L^2} & \frac{3EI_z}{L}
\end{bmatrix} \quad (123)$$

As previously mentioned the variable α_i is actually a function of the design variables and is defined as:

$$\alpha_i = \rho_{ji}^\beta k_{joint_max} \quad (124)$$

Please note ρ_j stands for “joint design variable” and is not index notation. The purpose of defining α_i in this manner is to control the rotational stiffness through a design variable that is constrained to values between zero and one. If ρ_j equals zero, then α_i equals zero; and if ρ_j equals one, then α_i equals k_{joint_max} . The magnitude selected for k_{joint_max} was 1,000. This value produced a stiffness of 99.7 percent of a true fixed end. The Pinned Joint-Stiff Beam-Rigid Joint element stiffness matrix is provided in Eq. (125).

$$\begin{bmatrix} \frac{2.991EI_z}{L^3} & 0 & -\frac{2.991EI_z}{L^3} & \frac{2.991EI_z}{L^2} \\ 0 & 0 & 0 & 0 \\ -\frac{2.991EI_z}{L^3} & 0 & \frac{2.991EI_z}{L^3} & -\frac{2.991EI_z}{L^2} \\ \frac{2.991EI_z}{L^2} & 0 & -\frac{2.991EI_z}{L^2} & \frac{2.991EI_z}{L} \end{bmatrix} \quad (125)$$

In addition to the previously derived in-plane element, an out-of-plane element of a similar derivation and a membrane element were added. The out-of-plane element supports the aerodynamic loads generated by the vortex lattice method and the membrane element serves to provide internal resistance within the structure. The membrane element is a basic four node, bilinear quadrilateral (Q4), plane isoperimetric element that is unable to support bending loads. The program is configured to accept user a specified pre-strain value. Figure 35 demonstrates how the pre-strain is applied.

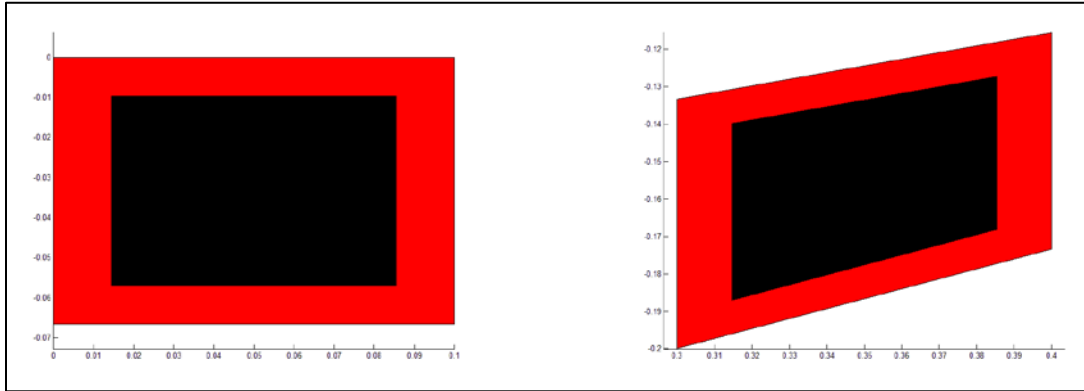


Figure 35: Membrane Pre-Strain

The pre-strain is achieved through the *patch* and *shrinkfaces* functions in MATLAB. In Figure 35, the black region represents the original dimensions and the red region represents the “stretched” dimensions. The internal load associated with stretching the membrane is then applied to the respective nodes in the element.

2.5.3 Vortex Lattice Method by Ring Vortex Elements/Aeroelastic Effects

To capture the aerodynamic effects on the structure for a given flight configuration, a vortex lattice method (VLM) based on ring vortex elements as described by Katz and Plotkin [28] was added. Results

from the VLM were compared with other commercially available codes such as Tornado and matched favorably. Examples of C_p plots for a flared wing configuration and swept wing configuration generated by this VLM are presented in Figure 36. The C_p distributions across the wings indicate typical results.

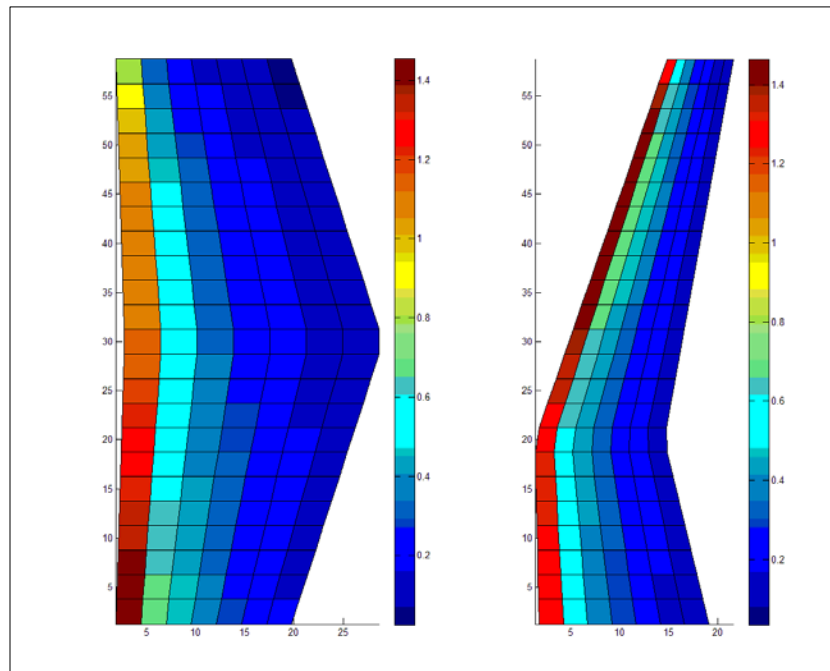


Figure 36: C_p Distributions

During the VLM subroutine, the aerodynamic influence coefficient (AIC) matrix used for static aeroelastic analyses was calculated. This matrix was used to calculate an aerodynamic stiffness penalty that was subtracted from the global stiffness matrix. This process provides a simple static aeroelastic result. Figure 37 provides an example of the deflections provided by the swept wing configuration static aeroelastic analysis.

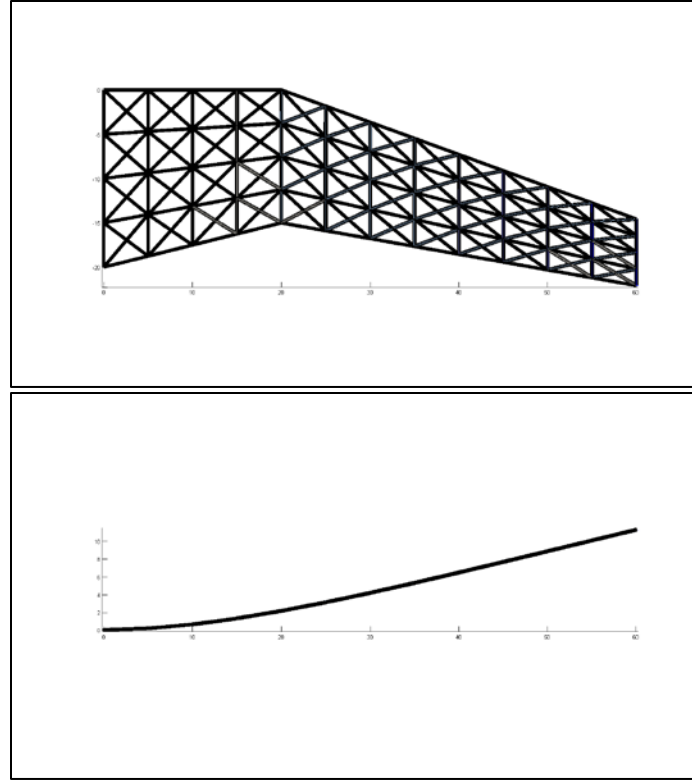


Figure 37: Static Aeroelastic Analysis

2.5.4 Optimization Background

The topology optimization relied on two primary tools to achieve results. The first is the Method of Moving Asymptotes (MMA), which served as the backbone to the optimization process. The second was the SIMP method, which drives the solution to an “off” or “on” state. The SIMP method is important for obtaining discrete solutions.

Method of Moving Asymptotes (MMA) [23] [26]

The Method of Moving Asymptotes (MMA), developed by Svanberg, is a method for non-linear programming specifically useful in topology optimization applications. Non-linear programming refers to the process of solving optimization problem formulations where the objective function or some of the constraints are non-linear. Consider a structural optimization problem in standard form.

$P^{(0)}$:

minimize

$$f_0(x) \quad (x \in R^n)$$

subject to

$$\begin{aligned} f_i(x) - \hat{f}_i &\leq 0 & \text{for } i = 1, \dots, m \\ \underline{x}_j &\leq x_j \leq \bar{x}_j & \text{for } j = 1, \dots, n \end{aligned} \tag{126}$$

where $f_0(x)$ is the objective function, $f_i(x) - \hat{f}_i \leq 0$ are the constraints, and $x = (x_1, \dots, x_n)^T$ is the vector of design variables.

A general approach to solving this problem formulation is to generate and solve a series of convex approximating sub-problems in an iterative manner:

- I. Define a starting point $x^{(0)}$, and initialize the iteration index $k = 0$.
- II. Given an iteration point $x^{(k)}$, calculate $f_i(x^{(k)})$ and the gradients $\nabla f_i(x^{(k)})$ for $i = 1, \dots, m$.
- III. Generate a sub-problem $P^{(k)}$ by replacing the original objective function and constraints by a convex approximation, based on the calculations of the previous step.
- IV. Solve the sub-problem $P^{(k)}$.
- V. Set the solution of this sub-problem as the next iteration point $x^{(k+1)}$.
- VI. Increment k and go to set I.

Repeat this process until a convergence criterion is fulfilled, or when the user is satisfied with the current

solution $x^{(k)}$. Essentially, $f_i^{(k)}$ is obtained by a linearization of f_i in variables of the type $\frac{1}{(x_j - L_j)}$ or $\frac{1}{(U_j - x_j)}$ depending on the signs of the derivatives of f_i at $x^{(k)}$. L_j and U_j are parameters that are usually updated between iterations and are generally referred to as “moving asymptotes.” The process for updating these parameters will be discussed later in this section.

In order to generate the convex approximating sub-problem, a Taylor Series Expansion is taken from the original problem formulation f_i at design point k :

$$f_i^{(k)}(X) = f_i(X^{(k)}) + \sum_j \left(\frac{\partial f_i(X^{(k)})}{\partial X_j} \right) (X_j - X_j^{(k)}) + \frac{1}{2} \sum_j \left(\frac{\partial^2 f_i(X^{(k)})}{\partial X_j^2} \right) (X_j - X_j^{(k)})^2 + R \quad (127)$$

where,

$$X = (X_1, \dots, X_n)^T \\ X^{(k)} = (X_1^{(k)}, \dots, X_n^{(k)}) \quad (128)$$

Ignoring higher-order-terms and transforming the independent design variables in the form:

$$X_j = \frac{1}{(U_j^{(k)} - x_j)} \text{ and } X_j^{(k)} = \frac{1}{(U_j^{(k)} - x_j^{(k)})} \\ \text{Or} \\ X_j = \frac{1}{(x_j - L_j^{(k)})} \text{ and } X_j^{(k)} = \frac{1}{(x_j^{(k)} - L_j^{(k)})} \quad (129)$$

the Taylor Series approximation takes the form:

$$f_i^{(k)}(x) = f_i(x^{(k)}) + \sum_j \left(\frac{\partial f_i(x^{(k)})}{\partial X_j} \right) \left(\frac{1}{(U_j^{(k)} - x_j)} - \frac{1}{(U_j^{(k)} - x_j^{(k)})} \right) \quad (130)$$

Applying the chain rule and orthogonally condition,

$$\frac{\partial f_i(x^{(k)})}{\partial X_j} = \left(\frac{\partial f_i(x^{(k)})}{\partial x_n} \right) \left(\frac{\partial x_n}{\partial X_j} \right) \quad (131)$$

and

$$\frac{\partial x_n}{\partial X_j} = 0 \quad \text{for } n \neq j \quad (132)$$

the variable transformation at the k^{th} design point is,

$$\frac{\partial x_n}{\partial X_j}(x_j^{(k)}) = \frac{dx_n}{d\left(\frac{1}{(U_j^{(k)} - x_n)}\right)}(x_j^{(k)}) = \frac{dx_n}{\frac{dx_n}{(U_j^{(k)} - x_n)^2}}(x_j^{(k)}) = (U_j^{(k)} - x_j^{(k)})^2 \quad (133)$$

Applying Eq. (133) and Eq. (131) to Eq. (130), the Taylor Series approximation takes the form:

$$f_i^{(k)}(x) = f_i(x^{(k)}) + \sum_j \left(\frac{\partial f_i(x^{(k)})}{\partial x_j} \right) (U_j^{(k)} - x_j^{(k)})^2 \left(\frac{1}{(U_j^{(k)} - x_j)} - \frac{1}{(U_j^{(k)} - x_j^{(k)})} \right) \quad (134)$$

this can be simplified to,

$$f_i^{(k)}(x) = r_i^{(k)} + \sum_{j=1}^n \left(\frac{p_{ij}^{(k)}}{U_j^{(k)} - x_j} \right) \quad (135)$$

where,

$$r_i^{(k)} = f_i(x^{(k)}) - \sum_{j=1}^n \left(\frac{p_{ij}^{(k)}}{U_j^{(k)} - x_j^{(k)}} \right) \quad (136)$$

$$p_{ij}^{(k)} = \frac{\partial f_i(x^{(k)})}{\partial x_j} (U_j^{(k)} - x_j^{(k)})^2 \quad (137)$$

The previous derivation only took into account the upper asymptotic variables. Applying the same procedure to the lower asymptotic variables provides a similar approximating function.

$$f_i^{(k)}(x) = r_i^{(k)} + \sum_{j=1}^n \left(\frac{q_{ij}^{(k)}}{x_j - L_j^{(k)}} \right) \quad (138)$$

where,

$$r_i^{(k)} = f_i(x^{(k)}) - \sum_{j=1}^n \left(\frac{q_{ij}^{(k)}}{x_j^{(k)} - L_j^{(k)}} \right) \quad (139)$$

$$q_{ij}^{(k)} = \frac{\partial f_i(x^{(k)})}{\partial x_j} (x_j^{(k)} - L_j^{(k)})^2 \quad (140)$$

These two approximations can be combined into a single approximation where the upper asymptotic approximation is used when $\frac{\partial f_i}{\partial x_j} > 0$ and the lower asymptotic is used when $\frac{\partial f_i}{\partial x_j} < 0$. This single approximation is shown below.

$$f_i^{(k)}(x) = r_i^{(k)} + \sum_{j=1}^n \left(\frac{p_{ij}^{(k)}}{U_j^{(k)} - x_j} + \frac{q_{ij}^{(k)}}{x_j - L_j^{(k)}} \right) \quad (141)$$

where,

$$r_i^{(k)} = f_i(x^{(k)}) - \sum_{j=1}^n \left(\frac{p_{ij}^{(k)}}{U_j^{(k)} - x_j^{(k)}} + \frac{q_{ij}^{(k)}}{x_j^{(k)} - L_j^{(k)}} \right) \quad (142)$$

$$p_{ij}^{(k)} = \begin{cases} \frac{\partial f_i(x^{(k)})}{\partial x_j} (U_j^{(k)} - x_j^{(k)})^2 & \text{if } \partial f_i / \partial x_j > 0 \\ 0 & \text{if } \partial f_i / \partial x_j \leq 0 \end{cases} \quad (143)$$

$$q_{ij}^{(k)} = \begin{cases} 0 & \text{if } \partial f_i / \partial x_j \geq 0 \\ -\frac{\partial f_i(x^{(k)})}{\partial x_j} (x_j^{(k)} - L_j^{(k)})^2 & \text{if } \partial f_i / \partial x_j < 0 \end{cases} \quad (144)$$

Furthermore, it can be verified that $f_i^{(k)}$ is a first order approximation of f_i at $x^{(k)}$ meaning,

$$f_i^{(k)}(x^{(k)}) = f_i(x^{(k)}) \text{ and } \partial f_i^{(k)} / \partial x_j = \partial f_i / \partial x_j \text{ at } x = x^{(k)}.$$

To verify the convexity of this sub-problem approximation, the second derivative of $f_i^{(k)}$ with respect to x such that $L_j^{(k)} < x_j < U_j^{(k)}$ can be given by

$$\frac{\partial^2 f_i^{(k)}}{\partial x_j^2} = \frac{2p_{ij}^{(k)}}{(U_j^{(k)} - x_j)^3} + \frac{2q_{ij}^{(k)}}{(x_j - L_j^{(k)})^3} \quad (145)$$

and

$$\frac{\partial^2 f_i^{(k)}}{\partial x_j \partial x_1} = 0 \quad \text{if } j \neq 1 \quad (146)$$

Thus, since $p_{ij}^{(k)} \geq 0$ and $q_{ij}^{(k)} \geq 0$, $f_i^{(k)}$ is a convex function. Looking more closely at Eq. (145) one can see that the closer $L_j^{(k)}$ and $U_j^{(k)}$ are to $x_j^{(k)}$, the larger the second derivative becomes, the more curvature is given to the approximation, and the more conservative the approximation befits the original problem. Conversely, if $L_j^{(k)}$ and $U_j^{(k)}$ are selected far away from $x_j^{(k)}$, then the approximating functions become more linear. In the extreme case of $L_j^{(k)} = -\infty$ and $U_j^{(k)} = \infty$, then the approximating function becomes identical to the linear Taylor Series approximation

$$f_i^{(k)}(x) = f_i(x^{(k)}) + \sum_j \left(\frac{\partial f_i(x^{(k)})}{\partial x_j} \right) (x_j - x_j^{(k)}) \quad (147)$$

which is commonly used in the “sequence of linear programs” method.

With the convex approximating function defined, the following sub-problem formulation is given by,

$P^{(k)}$:

Minimize

subject to

$$\begin{aligned} & \sum_{j=1}^n \left(\frac{p_{0j}^{(k)}}{U_j^{(k)} - x_j} + \frac{q_{0j}^{(k)}}{x_j - L_j^{(k)}} \right) + r_0^{(k)} \\ & \sum_{j=1}^n \left(\frac{p_{ij}^{(k)}}{U_j^{(k)} - x_j} + \frac{q_{ij}^{(k)}}{x_j - L_j^{(k)}} \right) + r_i^{(k)} - \hat{f}_i \leq 0 \quad \text{for } i = 1, \dots, m \\ & \max \{ \underline{x}_j, \alpha_j^{(k)} \} \leq x_j \leq \min \{ \bar{x}_j, \beta_j^{(k)} \} \quad \text{for } j = 1, \dots, n \end{aligned} \quad (148)$$

where, the parameters $\alpha_j^{(k)}$ and $\beta_j^{(k)}$ are “move limits,” which are used to avoid the possibility of an unexpected division by zero. To avoid a division by zero, the move limits should be chosen such that,

$$L_j^{(k)} < \alpha_j^{(k)} < x_j^{(k)} < \beta_j^{(k)} < U_j^{(k)} \quad (149)$$

Methods for updating the moving asymptote parameters, $L_j^{(k)}$ and $U_j^{(k)}$, will now be discussed. A simple method for updating the moving asymptote parameters is to let

$$L_j^{(k)} = \underline{x}_j - s_0(\bar{x}_j - \underline{x}_j) \text{ and } U_j^{(k)} = \bar{x}_j + s_0(\bar{x}_j - \underline{x}_j) \quad (150)$$

where, s_0 is a fixed real number typically less than one. In this example the moving asymptotes are not dependent on k , which means they are “fixed asymptotes” rather than “moving.” To leverage the complete power of this algorithm, one must allow the moving asymptotes to move between iterations. The rules governing how the asymptote parameters should move are:

1. If the process tends to oscillate, then it should be stabilized by moving the asymptote closer to the current iteration point.
2. If the process is monotone and slow, then the approximation needs to be relaxed by moving the asymptotes away from the current iteration point.

An implementation of this methodology is as follow:

For $k = 0 : 1$, let

$$L_j^{(k)} = \underline{x}_j^{(k)} - (\bar{x}_j - \underline{x}_j) \text{ and } U_j^{(k)} = \underline{x}_j^{(k)} + (\bar{x}_j - \underline{x}_j) \quad (151)$$

For $k \geq 2$

- a) If the signs of $x_j^{(k)} - x_j^{(k-1)}$ and $x_j^{(k-1)} - x_j^{(k-2)}$ are opposite, this indicates an oscillation. Therefore, let

$$\begin{aligned} L_j^{(k)} &= x_j^{(k)} - s(x_j^{(k-1)} - L_j^{(k-1)}) \\ U_j^{(k)} &= x_j^{(k)} + s(U_j^{(k-1)} - x_j^{(k-1)}) \end{aligned} \quad (152)$$

- b) If the signs of $x_j^{(k)} - x_j^{(k-1)}$ and $x_j^{(k-1)} - x_j^{(k-2)}$ are equal, this indicates the asymptotes are slowing down the convergence. Therefore, let

$$\begin{aligned} L_j^{(k)} &= x_j^{(k)} - (x_j^{(k-1)} - L_j^{(k-1)})/s \\ U_j^{(k)} &= x_j^{(k)} + (U_j^{(k-1)} - x_j^{(k-1)})/s \end{aligned} \quad (153)$$

The methods of adjusting the moving asymptote parameters presented in this section are those recommended by Svanberg. There are numerous alternatives to adjusting these parameters and further work is suggested to determine the best practices.

2.5.5 Problem Formulation

Properly defining the problem formulation is imperative for achieving useful results in an optimization routine. One must first begin by developing a descriptive statement for the problem which describes the overall objective and requirements to be met. For the purposes of this study, a design set of structural members and linear actuators are desired which morph a wing from one shape to another using the least amount of energy. Next, analysis tools are identified which are able to mathematically model the design domain. Finite element analysis and VLM routines provide the structural and aerodynamic models necessary to define this design space. The design variables must then be chosen that define the design space and allow for a feasible optimization solution. The design variables in this study alter the stiffness characteristics of the elements as previously described. The final steps are to define the objective function to be optimized and constraints that adequately bound the problem.

Many variations of objective functions and constraints have been explored during this effort and will be expanded upon in the subsequent thesis. Outlined in this report is the current, most promising objective function and constraint set, which permit the optimization of multiple wing configurations.

Topology optimization of morphing aircraft structures is a rather difficult problem to define. The design space is rather open and problem is defined by a very large number of design variables. In addition, multiple objectives such as shape matching and actuator minimization tend to conflict when the solver is trying to reach a global minimum value. One may use various weighting or normalization procedures; however experience has shown these methods are difficult to balance. A two-step optimization has demonstrated the most promise in producing reliable results.

The first step in this optimization process is to generate a set of design variables which morph the wing into all configurations without considering the minimization of the actuators. This shape matching objective drives the nodes on the outer mold line of the wing to pre-determined locations while limiting the stroke of each line element and the overall volume fraction of the wing.

The second step sets the shape matching criteria as a constraint along with the stroke and volume fraction constraints but focuses on minimizing the actuator usage, as well as a function that drives the elements to a 0-1 solution.

The objective functions for the two step process are defined below:

Step 1

minimize:

$$f_0 = \sum (U_i^{target} - U(\rho)_i)^2$$

subject to:

$$f_{eq} = KU - F = 0$$

Static Equilibrium

$$f_m = E_m^2 - E_{max}^2 \leq 0$$

Stroke Limit

$$f_{+V} = \sum_{i \in L1} \rho_i + \sum_{i \in L2} \rho_i - V_{max} \leq 0$$

Volume Fraction Limit

where:

$$\rho_{min} \leq \rho_i \leq 1.0 \quad i \in J1, J2, L1, L2, B$$

$$-1.0 \leq \rho_j \leq 1.0 \quad j \in A$$

(154)

Step 2

minimize:

$$f_0 = \rho_j^2 + \sum [1 - (\frac{\rho_{j1}^3 + \rho_{j2}^3 + \rho_{jL1}^3}{3})^3]$$

subject to:

$$f_{eq} = KU - F = 0$$

Static Equilibrium

$$f_m = E_m^2 - E_{max}^2 \leq 0$$

Stroke Limit

$$f_{+V} = \sum_{i \in L1} \rho_i + \sum_{i \in L2} \rho_i - V_{max} \leq 0$$

Volume Fraction Limit

$$f_{shape} = \sum (U_i^{target} - U(\rho)_i)^2 - shapeError_{max}$$

Shape Matching

where:

$$\rho_{min} \leq \rho_i \leq 1.0 \quad i \in J1, J2, L1, L2, B$$

$$-1.0 \leq \rho_j \leq 1.0 \quad j \in A$$

(155)

The second objective in Step 2 is novel for this type of optimization process because it essentially applies the SIMP method twice and penalizes values that are neither zero nor one since intermediate values will not generate a minimum value for that particular objective. The closer the design variable is to a value of one, the smaller the objective gets. The traditional SIMP method works great for topology optimization problems that aim to minimize compliance given a limit on the amount of volume fraction allowed. The SIMP method works in a minimum compliance problem formulation because values that are neither zero nor one do not effectively utilize the potential gain in element stiffness and therefore “waste” valuable

volume fraction allotment. For topology optimization of morphing aircraft, the objective function as defined without this added objective can be minimized without producing a 0-1 solution. Just as the volume fraction limit drives the minimum compliance problem to 0-1 solution using the SIMP method, so does this additional objective in topology optimization for morphing structures. In addition, this additional objective drives the solution to favor complete beams with rigid joints such that only necessary telescoping members and revolute joints exist.

2.5.6 Sensitivity Analysis

Generally, sensitivities with respect to the design variables are required by optimization algorithms. When the objective function and constraints are functions of only the design variables, these sensitivities are fairly straightforward to derive. For functions that depend on the displacements as well as the design variables, the sensitivities can be derived by the chain-rule. These expressions will then contain the derivatives of the displacement, which can be obtained by taking the derivative of the static equilibrium equation:

$$KU = F \quad (156)$$

The following section describes how the sensitivity of the shape matching objective function is calculated.

In topology optimization, a moderate number of constraints are typically used. Therefore, it is generally better to calculate the sensitivities using the adjoint method where the derivatives of the displacements are not calculated explicitly. The displacement at the i^{th} degree of freedom can be expressed in terms of the global displacement by:

$$U_i = I_i^T U \quad (157)$$

Where I_i is the vector with 1 in the i^{th} and 0 in all other components. Since $KU - F = 0$, this function can be added to Eq. (157) without altering its value and can be written as:

$$U_i = I_i^T U + \lambda_i^T (KU - F) \quad (158)$$

Where λ_i is any arbitrary, but fixed real vector. Therefore the sensitivity of the displacement component can be written as:

$$\frac{\partial U_i}{\partial \rho_e} = I_i^T \frac{\partial U}{\partial \rho_e} + \lambda_i^T \frac{\partial K}{\partial \rho_e} U + \lambda_i^T K \frac{\partial U}{\partial \rho_e} - \lambda_i^T \frac{\partial F}{\partial \rho_e} \quad (159)$$

Which can be rearranged as:

$$\frac{\partial U_i}{\partial \rho_e} = (I_i^T + \lambda_i^T K) \frac{\partial U}{\partial \rho_e} + \lambda_i^T \frac{\partial K}{\partial \rho_e} U - \lambda_i^T \frac{\partial F}{\partial \rho_e} \quad (160)$$

Since the derivative of the global displacement vector cannot be obtained directly and since λ_i is arbitrary, one can set the first term to vanish by applying the following condition:

$$(I_i^T + \lambda_i^T K) = 0 \quad (161)$$

Which can be rearranged as:

$$K\lambda_i = -I_i \quad (162)$$

Where λ_i can be solved for and applied to Eq. (160) in order to obtain a manageable displacement sensitivity:

$$\frac{\partial U_i}{\partial \rho_e} = \lambda_i^T \frac{\partial K}{\partial \rho_e} U - \lambda_i^T \frac{\partial F}{\partial \rho_e} \quad (163)$$

Using Eq. (163), the gradient of the multi-objective function can now be expressed as:

$$\frac{\partial f_0}{\partial \rho_e} = \begin{cases} -2 \sum_{i \in T} (U_i^{target} - U_i) \frac{\partial U_i}{\partial \rho_e} & e \in J1, J2, L1, L2, A \end{cases} \quad (164)$$

By applying Eq. (163) to Eq.(164), one can obtain the full objective function sensitivity:

$$\frac{\partial f_0}{\partial \rho_e} = \begin{cases} -2W_1 \sum_{i \in T} (U_i^{target} - U_i) \lambda_i^T \frac{\partial K}{\partial \rho_{J1}} U & e \in J1 \\ -2W_1 \sum_{i \in T} (U_i^{target} - U_i) \lambda_i^T \frac{\partial K}{\partial \rho_{J2}} U & e \in J2 \\ -2W_1 \sum_{i \in T} (U_i^{target} - U_i) \lambda_i^T \frac{\partial K}{\partial \rho_{L1}} U & e \in L1 \\ -2W_1 \sum_{i \in T} (U_i^{target} - U_i) \lambda_i^T \frac{\partial K}{\partial \rho_{L2}} U & e \in L2 \\ 2W_1 q \rho_A^{q-1} \sum_{i \in T} (U_i^{target} - U_i) \lambda_i^T F_e^0 & e \in A \end{cases} \quad (165)$$

Section 3. RESULTS

This chapter explores wing structure layouts on a conceptual level for several wing shapes under various loading conditions. First, the aerodynamic results from Tornado of the birdwing geometry (Figure 11 through Figure 14) at the four points in the perching trajectory are presented. Then, the compliance minimization runs for each birdwing layout are compared. Finally, a brief grid independence check is provided.

3.1 Aerodynamic Results

The birdwing of Figure 11 through Figure 14 with zero camber (i.e., flat plate) maneuvering through the perching trajectory of Figure 20 is considered here. The wing is in the back swept position at Point 1, the dive position at Point 2, the zero sweep position at Point 3, and the forward swept position at Point 4.

The Tornado calculations of the birdwing at the four points along the perching trajectory are summarized in Table 3. The velocity and angle of attack have been included for reference.

Table 3: Aerodynamic Data for Birdwing along Perching Trajectory

		Point 1	Point 2	Point 3	Point 4
Vel.	m/s	10	10.41	10.11	2.19
AOA	°	6	3.75	10	50
Drag	N	0.0176	0.0033	0.0796	0.0456
Side	N	0.0061	0.0075	-0.0007	-0.0087
Lift	N	0.459	0.112	1.241	0.196
F _x	N	-0.0304	-0.0040	-0.1371	-0.1208
F _y	N	0.00610	0.00749	-0.00066	-0.00871
F _z	N	0.458	0.112	1.236	0.161
C _L	—	0.220	0.076	0.512	1.701
C _D	—	0.0085	0.0022	0.0328	0.3958
C _Y	—	0.0029	0.0051	-0.0003	-0.0757
R _e	—	90054	137712	91412	19987
CDo	—	0.0101	0.0082	0.0101	0.0113
Swet	m ²	0.0681	0.0444	0.0775	0.0785
Dvis	N	0.2368	0.1077	0.4410	0.0885
Normal	N	0.0248	0.0070	0.0766	0.0678
Axial	N	0.2355	0.1075	0.4343	0.0569

The lift forces at first glance seem to be inordinately small, as they are on the order of 1 N. However, since the wing is a flat plate, an estimate of the lift can be made assuming a lift slope of 2π . For the back swept configuration at Point 1, the lift coefficient is then

$$c_l = 2\pi\alpha = 2\pi(6\pi/180) = 0.6580 \quad (166)$$

The lift per unit span becomes

$$L' = c_l q_\infty c = 0.6580 \left[\frac{1}{2} (1.2244 \text{ kg/m}^3) (10 \text{ m/s}) \right] (0.153 \text{ m}) = 6.1630 \text{ N} \quad (167)$$

If the wing were rectangular with uniform lift per unit span across the span, the total lift force for the wing would be

$$L = L' * b = (6.1630 \text{ N})(0.270 \text{ m}) = 1.664 \text{ N} \quad (168)$$

The lift is in fact on the order of 1 N for such a small wing at a very low speed (about 23 mph). Since the wing is tapered and the lift distribution is certainly not uniform across the span, the resulting lift values are necessarily lower than predicted by the simple preceding equations. As expected, the highest lift occurs at Point 3 as the birdwing begins its ascent, and the lift at Point 2 is the lowest, about a tenth of the value at Point 3.

The drag calculated by Tornado is solely the induced drag, and therefore is related to the square of the lift coefficient. The higher drag values occur in the ascending portion of the trajectory, when the lift coefficient is highest. The fact that the drag at Point 4 is lower than at Point 3 is due to the very low velocity of 2.19 m/s. In retrospect, selecting a point along the trajectory between Points 3 and 4 where the velocity is only somewhat reduced and the angle of attack is relatively high would have produced a higher drag load. The drag at Point 2 is smaller than the drag at Point 3 by a factor of 24, due to the reduced wing area and the smaller angle of attack.

The distributions of the pressure coefficient differences between the upper and lower surfaces of the wing are shown in Figure 38. The pressure coefficient differences are much greater for the forward swept configuration at the end of the maneuver, where the angle of attack is very high. Contrariwise, the pressure coefficient differences are very low for the birdwing as it dives, because it is slicing through the air at a low angle of attack. In each of the four plots, the pressure coefficient difference is about four times that of the general distribution (the yellow areas) over the wing.

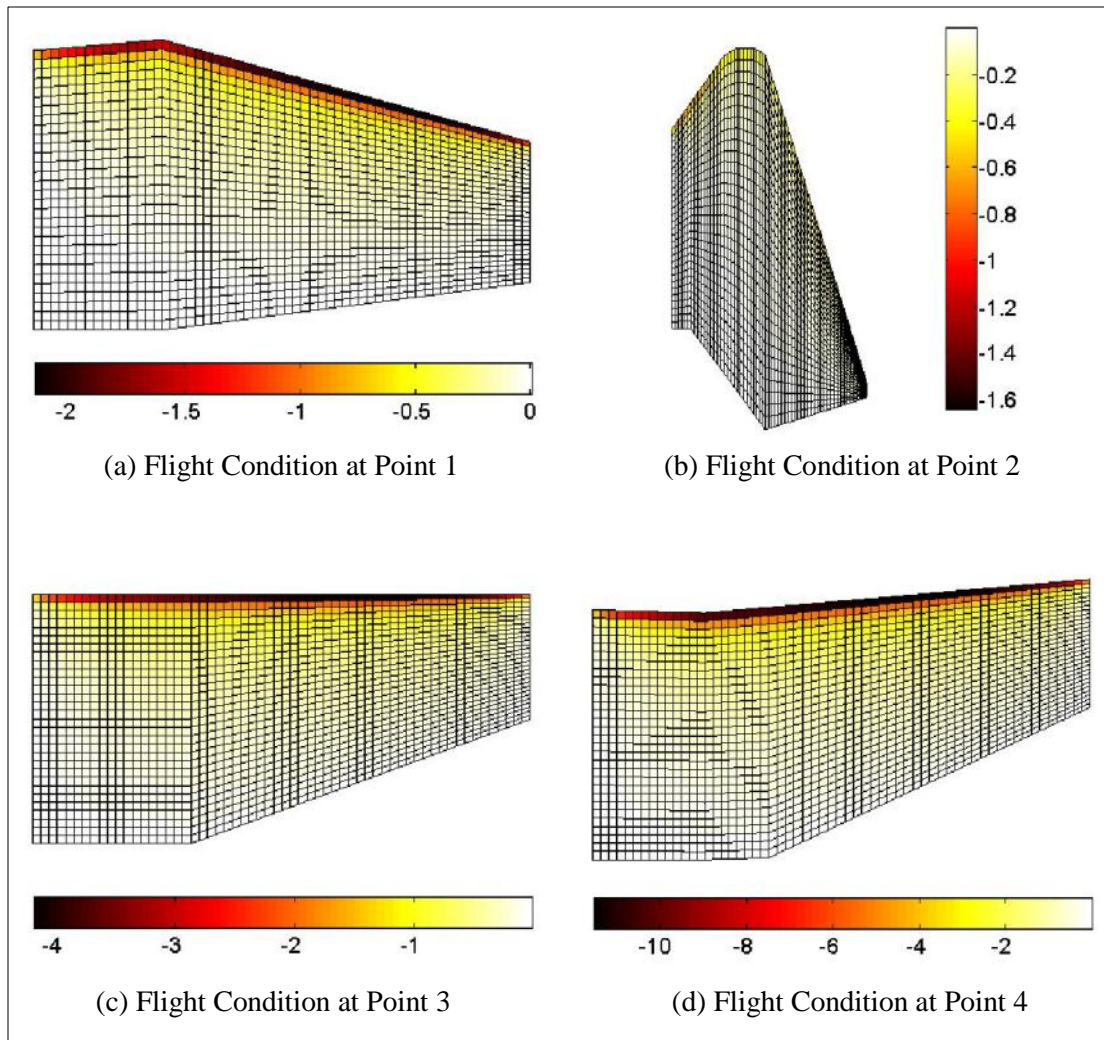


Figure 38: C_p for Birdwing Geometries along Perching Trajectory

The distribution of the force components and magnitudes is shown for each configuration of the birdwing in Figure 39 through Figure 42. The forces shown include the addition of the viscous drag estimates to the body forces. The viscous drag is split into a normal and axial component due to the angle of attack. The positive x-axis extends towards the tip of the wing in the spanwise direction, and the y-axis extends towards the leading edge in the chordwise direction.

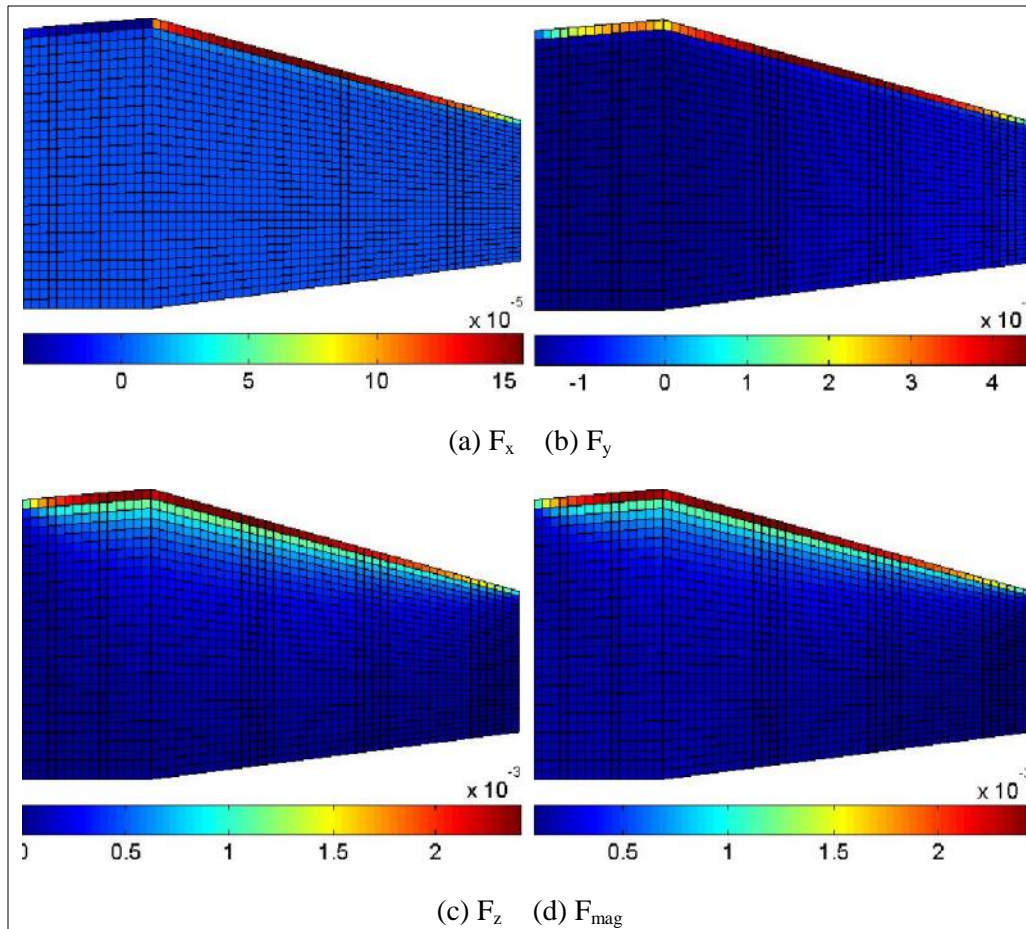


Figure 39: Force [N] for Birdwing in Swept Back Configuration at Point 1

At each point in the maneuver, the side forces (F_x) are relatively negligible and not expected to influence the structural layout much. The axial forces stimulate interest because, at the leading edge, the forces act in the positive y-direction, whereas everywhere else on the wing, the axial forces act in the negative y-direction (as intuition suggests). The fact that the leading edge is seemingly being pulled forward is due to the domination of the axial component of the lift over the axial component of the drag. The lift calculated by Tornado at each panel over the surface of the whole wing dominated the drag in the axial direction; however, the added viscous drag reversed the net force over the all of the wing except the leading edge. Hence the structure is being stretched in both axial directions.

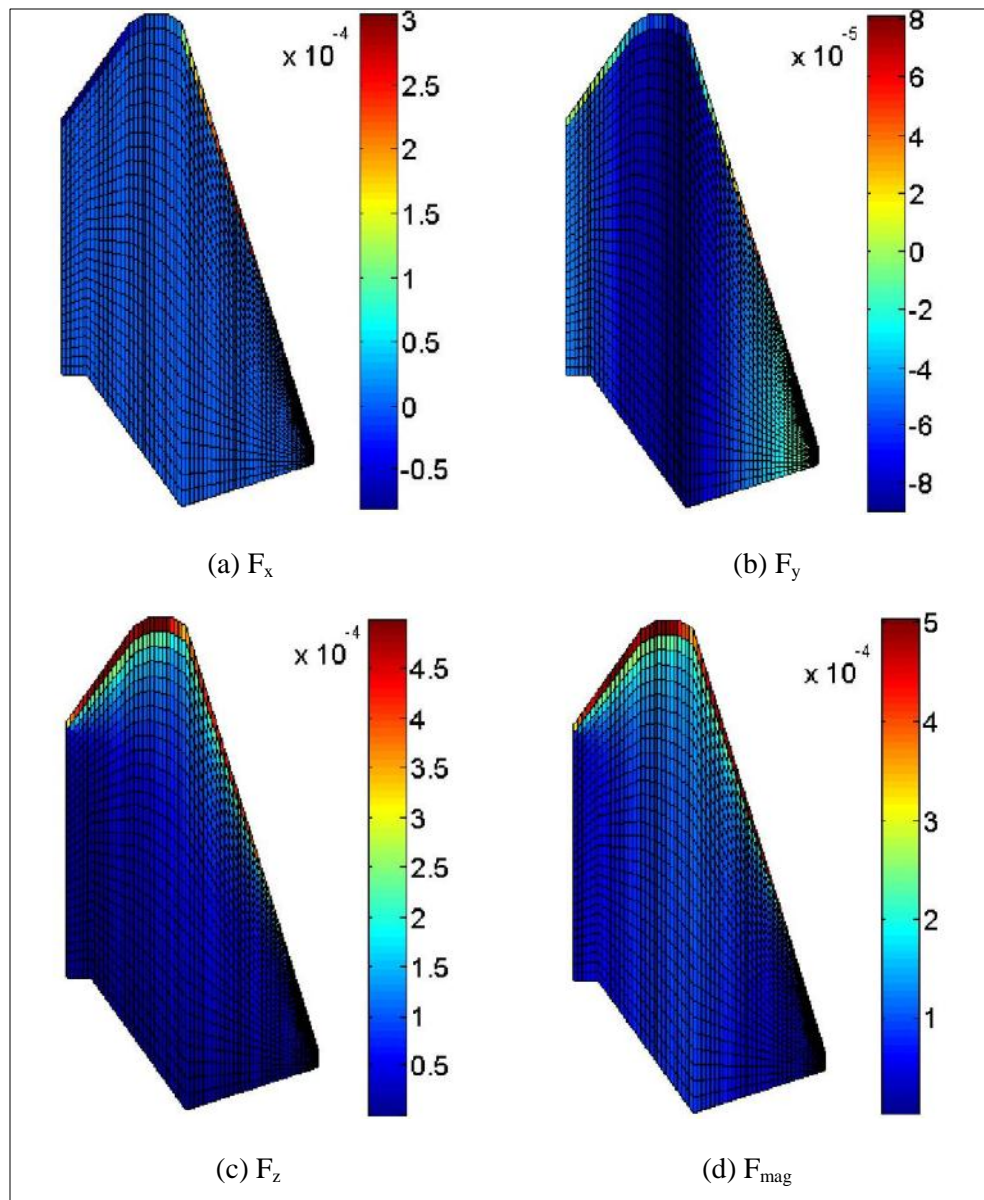


Figure 40: Force [N] for Birdwing in Dive Configuration at Point 2

The loads for the dive configuration are on the order of 10^{-4} , whereas the loads for the other cases are on the order of 10^{-3} ; thus, the dive configuration is probably not a good design point since ultimately the loads at each configuration will have to be withstood by a single structure.

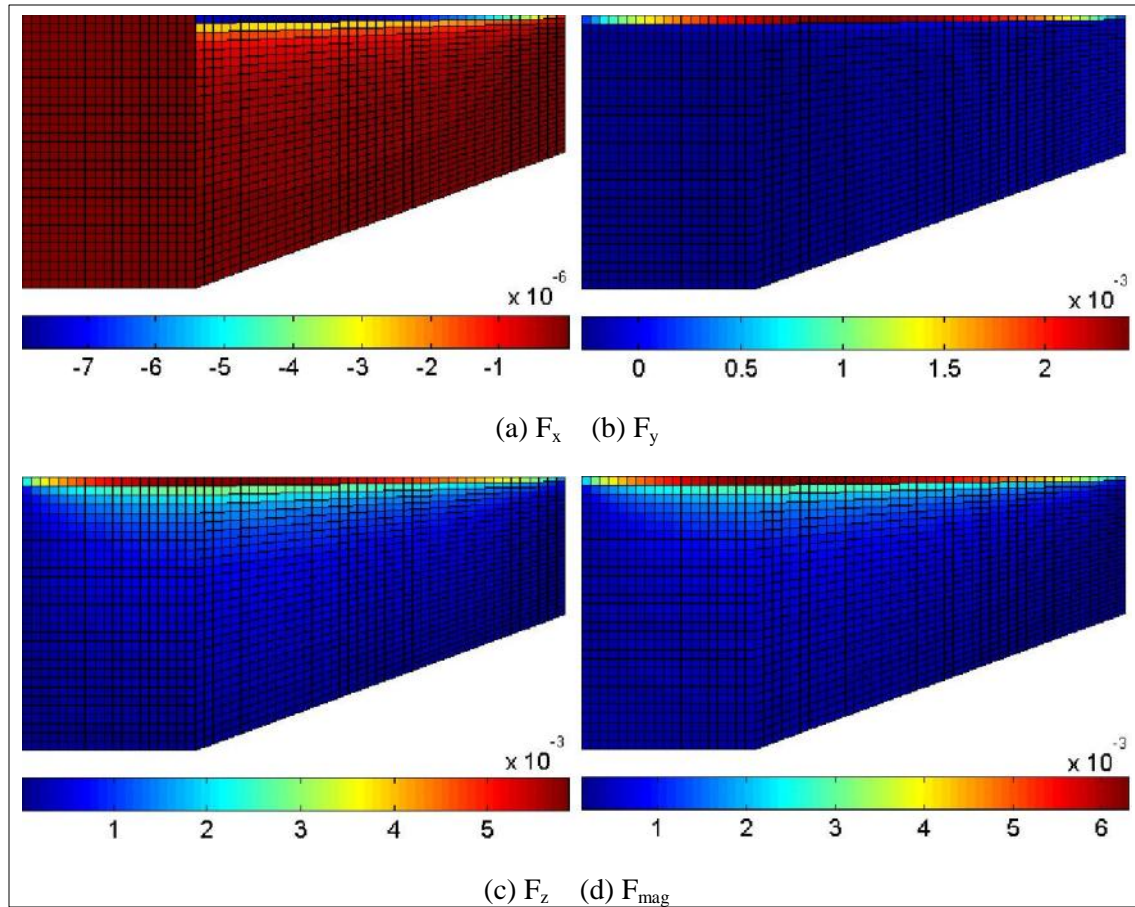


Figure 41: Force [N] for Birdwing in Zero Sweep Configuration at Point 3

Clearly the load on each of the configurations is leading edge dominated. Thus a good baseline comparison for resulting structures could be constructed by simply distributing a load over the leading edge of a similar geometry. Also, resultant magnitude contours of each point in the maneuver, except the last, match the contours of the normal component F_z , indicating that the bending loads are the dominant loads. The flaring of the wings at the end of the maneuver should be bending dominated as well, but Point 4 that was selected occurs when only a fraction of the peak velocity remains. Therefore, the corresponding drag loads are low, and the bending dominance is not captured. In all cases (except perhaps in the case of the dive), the trailing edge of the tip of the wing experiences essentially no load and suggests that corresponding structures may clip the lower tip of the wing.

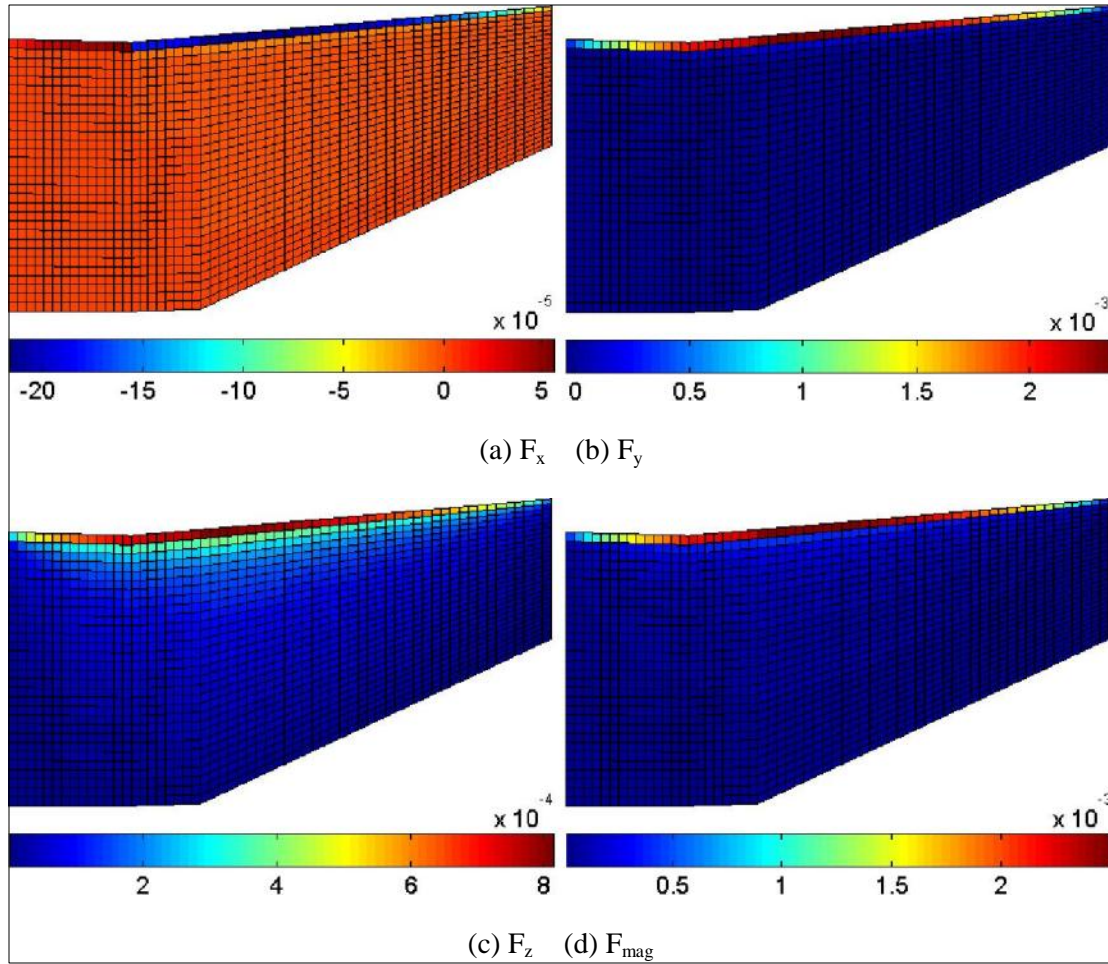


Figure 42: Force [N] for Birdwing in Forward Swept Configuration at Point 4

Though the magnitudes of the body forces of the birdwing in the perching trajectory is very low, the relative magnitudes are of greater importance to the optimization process. The majority of the relative magnitudes of lift and drag seem acceptable, but the most unreasonably captured aerodynamic extreme is the drag at the end of the maneuver which should be a bending-dominated load. The beginning of the maneuver is also dominated by bending loads, but due to the lift and not the drag. If the optimization process determines any hybrid membrane-bending structures, it is anticipated that the Point 3 flight condition would produce this effect.

3.2 Optimized Static Structural Layouts

For each point along the perching maneuver, three sets of loading scenarios were performed. The first set consisted of only the membrane forces (F_x and F_y), the second set considered the bending forces (F_z) only, and the third set was the combined membrane-bending loading scenarios. Each set consisted of four cases with volume fractions ranging from 0.2 to 0.5. Unless convergence issues arose, each case had a penalization of 3, a filter radius of 1.5, and was run with a move limit of 0.2 and a damping of 0.5. All the runs were minimized until the solution converged within a 0.01 maximum thickness change.

The results of the compliance minimization for the birdwing at Point 1 in the perching maneuver is shown in Figure 43 through Figure 45. Considering first the purely membrane solution of Figure 43, the

predominate structural features are the two members extending from the root of the wing in the form of a wishbone, and at the tip of the wing, a second wishbone forms. Even though the predominate membrane forces occur along the leading edge, the leading edge is not built up across the whole span like it is for the topologies of Section 3.1. This is due to the force along the remainder of the wing pulling the wing in the opposing negative chordwise direction. The “wishbone” is a natural structure to resist a spreading motion (the converse motion of squeezing a pair of pliers). It can be thought of as antipodal to two joined buttresses. Had all of the force in the chordwise direction been directed towards the trailing edge, the structures would be expected to have a fully supported leading edge. The second main members are those along the leading and trailing edges. As evidence that the two wishbones and the leading and trailing edge members comprise the main structure, each time material is added to the wing domain, these members are thickened.

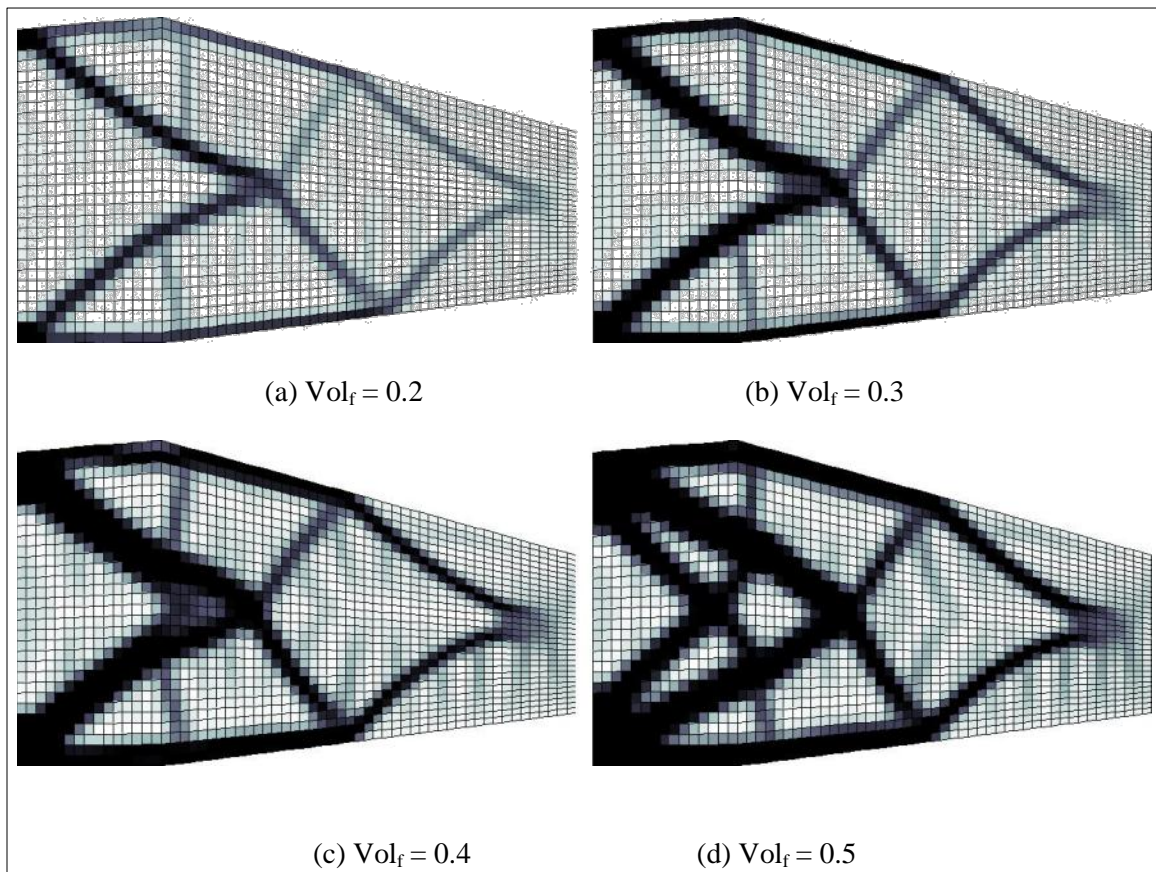


Figure 43: Membrane Structure for Birdwing at Point 1

The wishbone structure and the intermediate members form a scissor-like structure, and consequently the voided areas are predominately quadrilateral in shape. This is in contrast to the usual triangular voids in trusses.

Another striking feature of the structure is the straight protrusions of intermediate thickness. These battens or rods point towards the center of a voided area, and towards the unsupported perimeter of the wing domain. Thus they are comparable to spokes on a wheel. This feature is a result of a distributed load covering the en-tire surface of the wing, and is absent in an over-simplified point load model. At a fifty

percent volume fraction, the topology finally adds new members in the form of another smaller wishbone inscribed within the main wishbone.

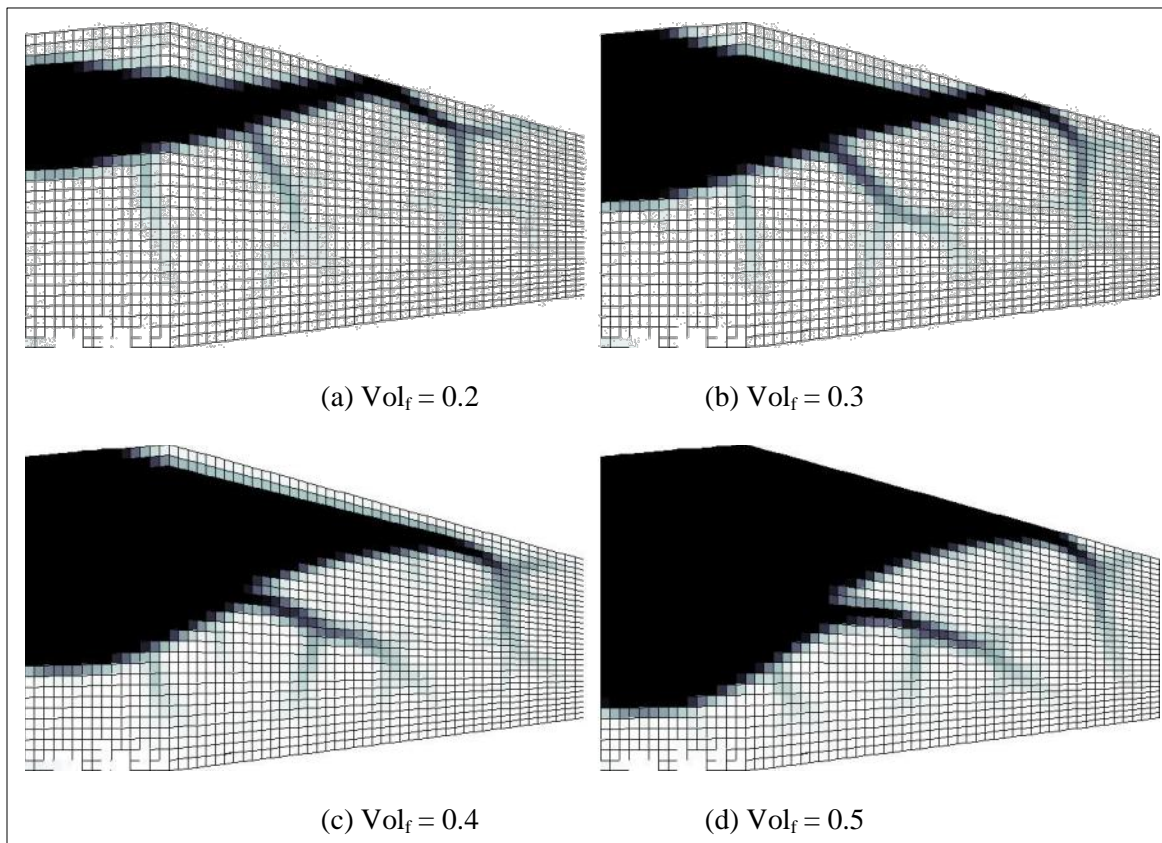


Figure 44: Bending Structure for Birdwing at Point 1

The bending structures of Figure 44 reveal that the basic form of the bending-resistant structure is not a truss, but rather a conglomeration in the form of a beam. The importance of exploring a range of volume fractions for a given wing shape and loading scenario is evident in the progression from Figure 44(a) to Figure 44(d). The impression of the 50 percent volume fraction case is that the bending structure primarily supports the leading edge, where the bending forces are highest. But Figure 44(a) shows this is clearly not the case. The most basic or crucial structure is a beam that is situated near the quarter chord of the wing. For the flat plate birdwing, the quarter chord is also approximately the center of pressure and the aerodynamic center of the wing, where the aerodynamic moment is zero. As the volume fraction increases, material is added along the sides of the original beam of Figure 44(a). The developing shape of the beam is similar to the shape of a wishbone (i.e., like A-arms in a suspension system), or in a more crude sense, the shape of a delta.

Like the rods or battens in the membrane structure, the bending structure also develops a secondary feature captured by the intermediate thicknesses. Rather than straight rods with a regular arrangement, branches stem from the central beam structure in arbitrary directions, and then further divide into smaller networks that attempt to cover as extensive a region as possible. The branches resemble veins in the wings of insects, and as the high density of nerves in bats attest, are a very effective method of stiffening a membrane skin.

The combined membrane and bending structure for the first point in the maneuver is shown in Figure 45, revealing an identical structure to the membrane case. However, when the viscous drag is removed, the result is that of Figure 46, which reveals a hybrid solution of the two isolated membrane and bending cases.

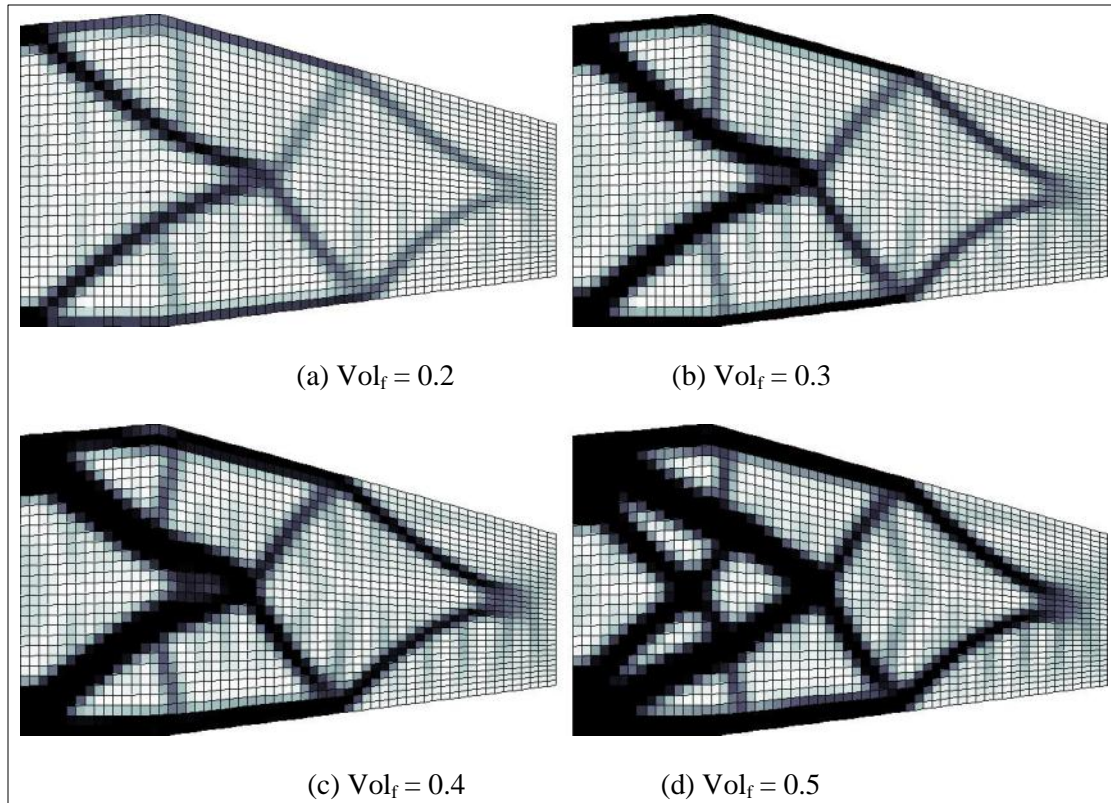


Figure 45: Combined Structure for Birdwing at Point 1

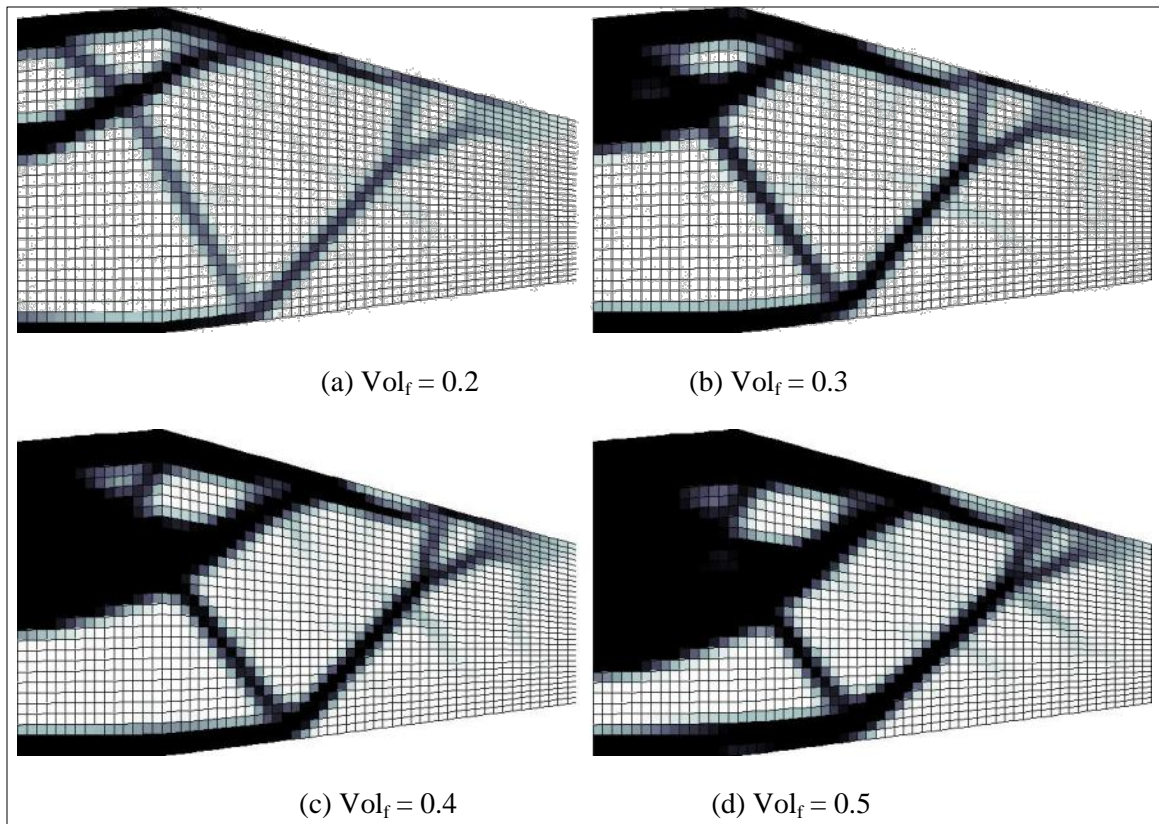


Figure 46: Combined Structure for Birdwing at Point 1 without Viscous Drag

This is not immediately evident in Figure 46(a), but the higher volume fraction solutions all have a delta-shaped “beam” on the front half of the wing. All of the solutions have supporting truss structure along the trailing edge of the wing that then connects to the leading edge near the tip of the wing. As material is added, the general topology remains unchanged, however the beam portion of the structure shifts in the chordwise direction, such that at fifty percent volume fraction, it is centered mid-chord. Both the scissor pattern from the membrane solution and the beam extending most of the way in the spanwise direction are attenuated, and the emerging structure better resembles a perimetric truss structure with spokes protruding inward to a hub covering the upper left corner of the wing. The vein-like stiffeners are absent, and only a few rods are present. While the hybrid solution is interesting, in actuality a completely membrane structure supports the combined loading according to the compliance results. The larger lifting loads and smaller drag loads at the relatively small angle of attack of Point 1 would suggest a more bending-dominated solution, but the effect of the distributed viscous drag load drives the solution towards a membrane structure.

As previously mentioned, the diving portion of the perching maneuver is perhaps not a good design point when the magnitude of the loads experienced throughout the entire maneuver is considered. However, the wing shape is quite distinct from the other three configurations and thus yields unique structures worthy of investigation. The resulting structures are presented in Figure 47 through Figure 49.

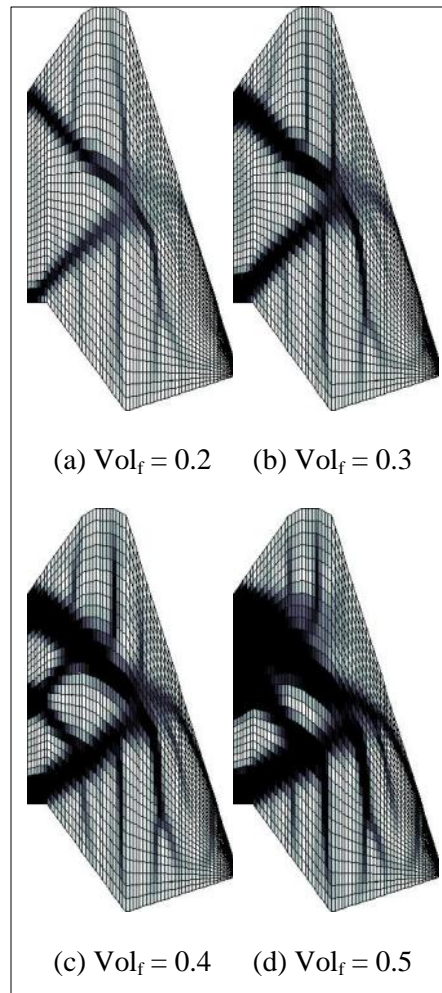


Figure 47: Membrane Structure for Birdwing at Point 2

If obscured by other truss members in the back swept wing configuration, there is no overlooking the prominent wishbone of Figure 47. In fact, it is the only truss structures present in Figure 47(a) and (b). In Figure 47(c), a smaller wishbone facing opposite of the main wishbone is inscribed within the main wishbone again producing a quadrilateral void and a scissor-like structure. Aside from this small amount of “truss” structure, the remainder of the structure consists of very long and definitive battens, in comparison with those in the back swept wing structure. In fact, the battens are not of intermediate value, but are maximum thickness. As shown in Figure 40(b), the maximum axial load occurs at the leading edge near the tip of the wing, and accordingly a batten extends to the tip of the wing. The region is not just darkened because of the overly refined mesh. In light of the poor finite element mesh of the dive wing shape, an instructive structure develops.

The compliance minimization of the bending structures shown in Figure 48 was troublesome, and only the forty and fifty percent volume fraction runs yielded results that were not explicitly erroneous. The twenty and thirty percent volume fraction cases were never close to converging, even for a number of different damping and move limit settings. Instead, they repeatedly violated the volume constraint, and the maximum thickness change diverged as the iterations progressed.

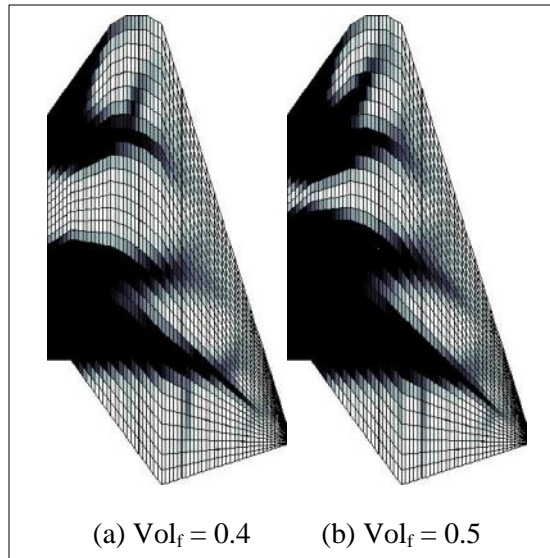


Figure 48: Bending Structure for Birdwing at Point 2

The maximum thickness change between iterations of the two solutions that were obtained oscillated in very high increments and eventually did drop beneath the 0.01 threshold. However, such unsteadiness in the tracking data is indicative of results that can hardly be said to have converged. In light of the poor solution, Figure 48 reveals two separate beam structures at the leading and trailing edge of the wing. The proportion and location of the “stiffeners” at the end of the beam extending towards the tip of the wing, when viewed as a whole, perhaps resemble feather-like protrusions.

As in the combined loading case of Point 1, the distributed viscous drag again leads to combined structures identical to the isolated membrane structures, and is shown in Figure 49. When the viscous drag is again removed, the combined loading case for Point 2 results in Figure 50. In this case, Point 2 elicits a clearly bending-dominated structure. Even though the lifting load is significantly diminished, the induced drag loads are extremely low and hence show virtually no influence in the structure, save a few faint battens. Instead the structure is mainly comprised of relatively equally sized and spaced branches extending from the root chord to the tip chord, like tines on a fork. The structure bypasses the trailing edge entirely.

As the birdwing in the perching maneuver begins its ascent, it is transitioning from bending loads due to lift to bending loads due to drag. At this transitional stage, axial and normal body forces are the same order of magnitude, and, more so than at the other points, a hybrid membrane-bending solution is anticipated. The results of the compliance minimization for Point 3 are shown in Figure 51 through Figure 53.

The layout and features of the membrane solution in Figure 51 are very similar to that of Figure 43, with one major distinction. The trailing edge is better supported than the leading edge. This could in part be due to the forward sweep of the trailing edge (unlike the relatively symmetrical planform of the swept back configuration). However, Figure 51(a) is particularly perplexing, as the leading edge is very faintly supported by a very long leg of a wishbone. One explanation may lie in the fact that there is less positive axial force than that of the back swept configuration, and hence the trailing half of the wing is being pushed relatively more in the negative axial direction compared to how much the leading edge is being

pushed in the positive axial direction. At any rate, the disparity between the support along the leading and trailing edges vanishes with higher volume fractions.

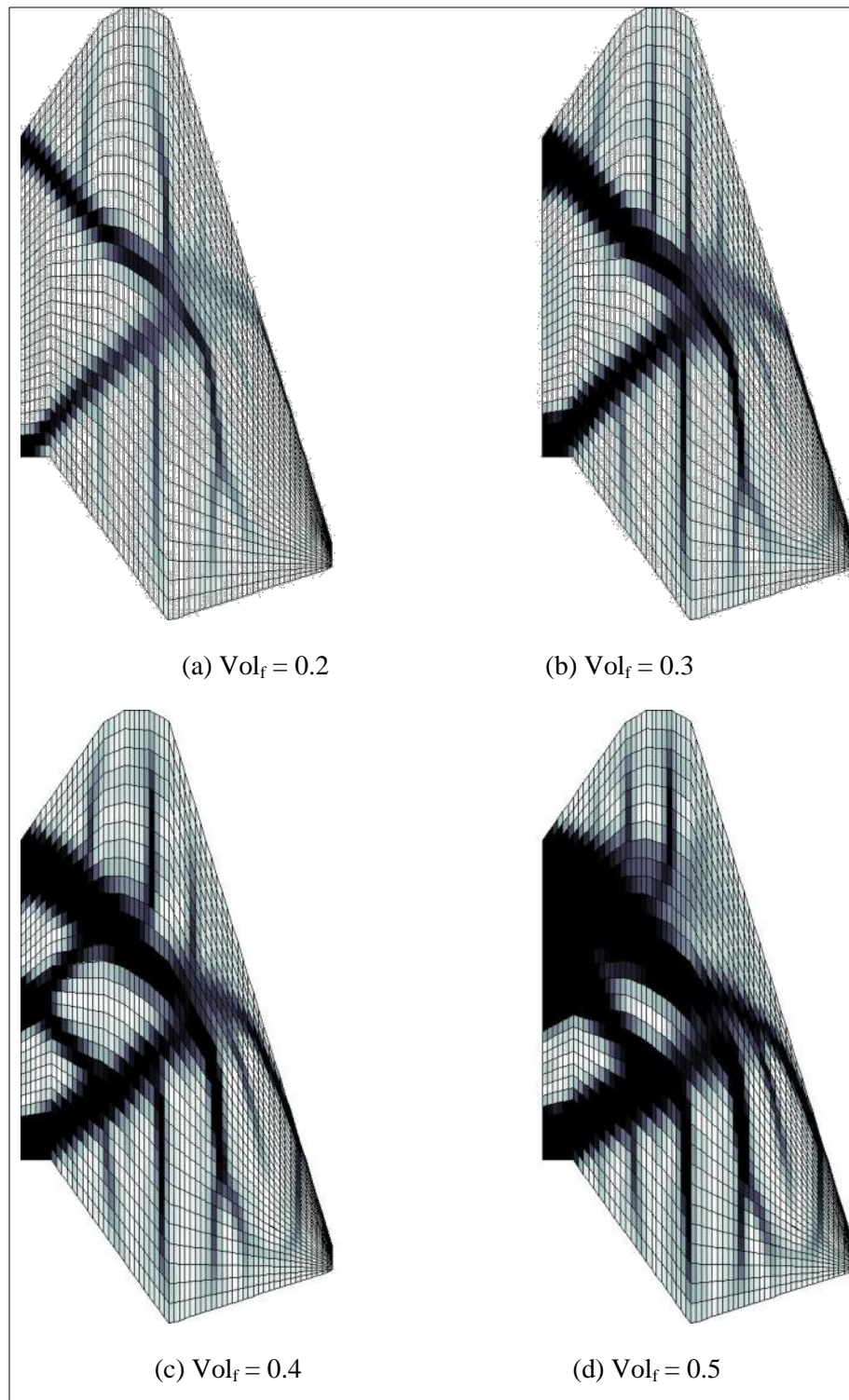


Figure 49: Combined Structure for Birdwing at Point 2

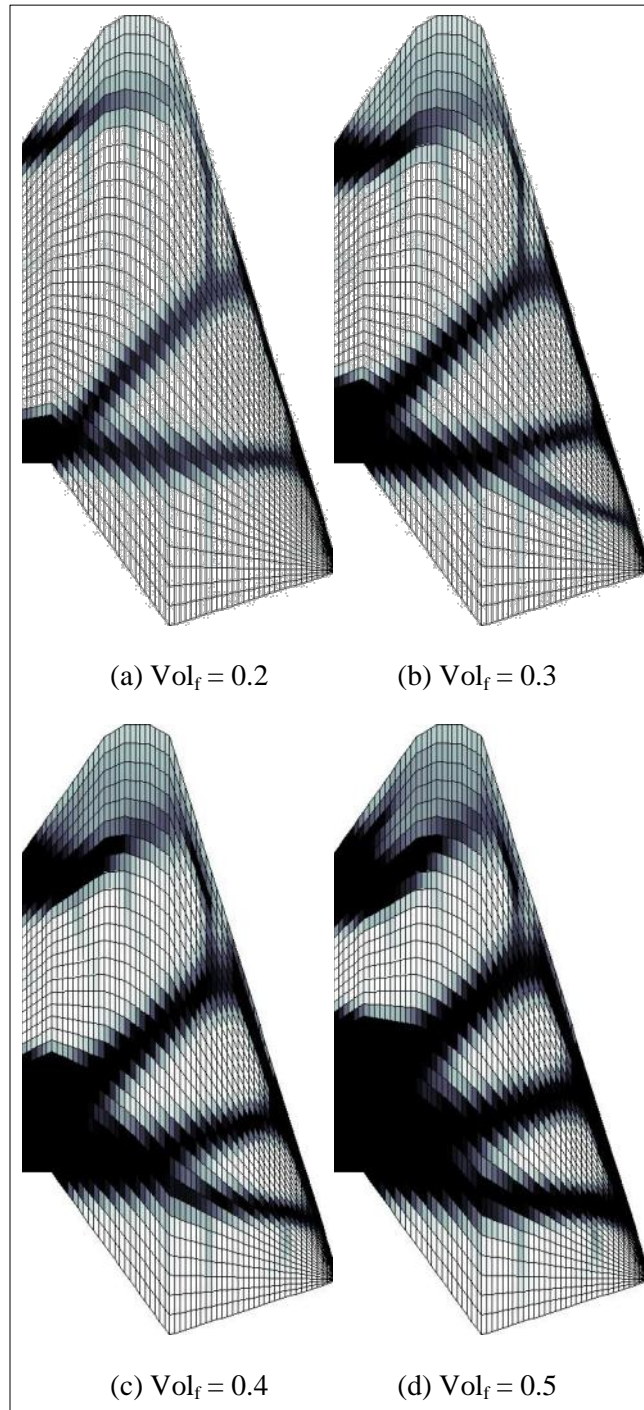


Figure 50: Combined Structure for Birdwing at Point 2 without Viscous Drag

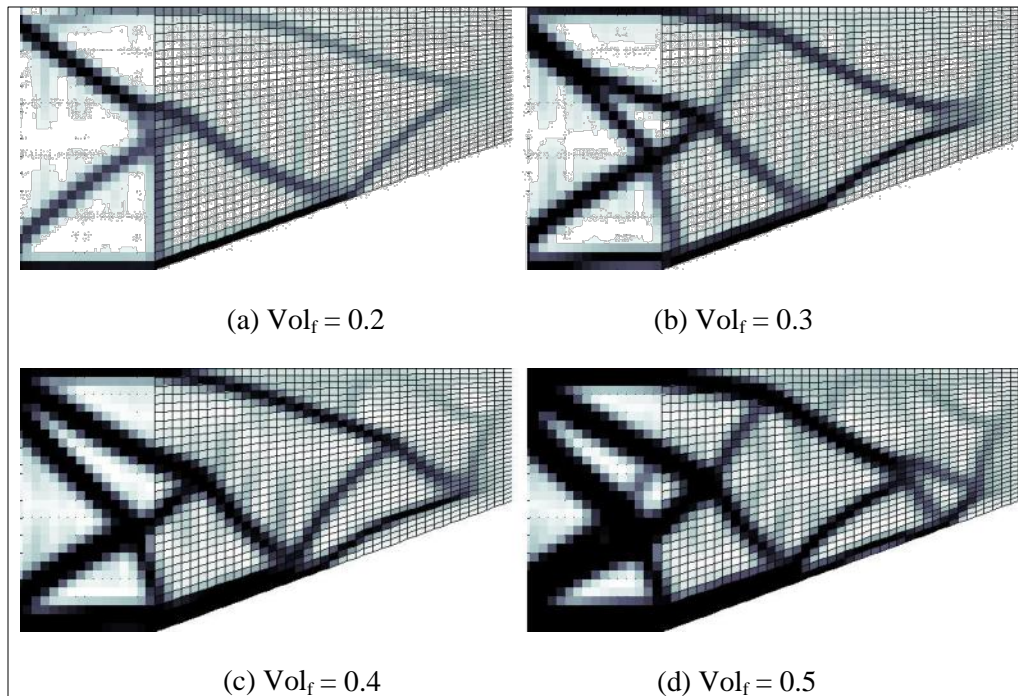


Figure 51: Membrane Structure for Birdwing at Point 3

The bending structures are very similar to those of the back swept configuration at Point 1. A single beam extends from the root chord most of the way to the tip of the wing. Also, the same types of stiffeners appear. However, the beam in this instance is clearly building up the leading edge, and is not centered near the quarter chord.

Figure 53 does not reveal a hybridization of membrane and bending elements as anticipated. The solution again favors a membrane structure, both with and without the presence of the viscous drag. However, in the absence of viscous drag (Figure 54) a thicker leading edge emerges, and mass starts to cluster around the upper left corner of the wing, as it does slightly in Figure 53(d).

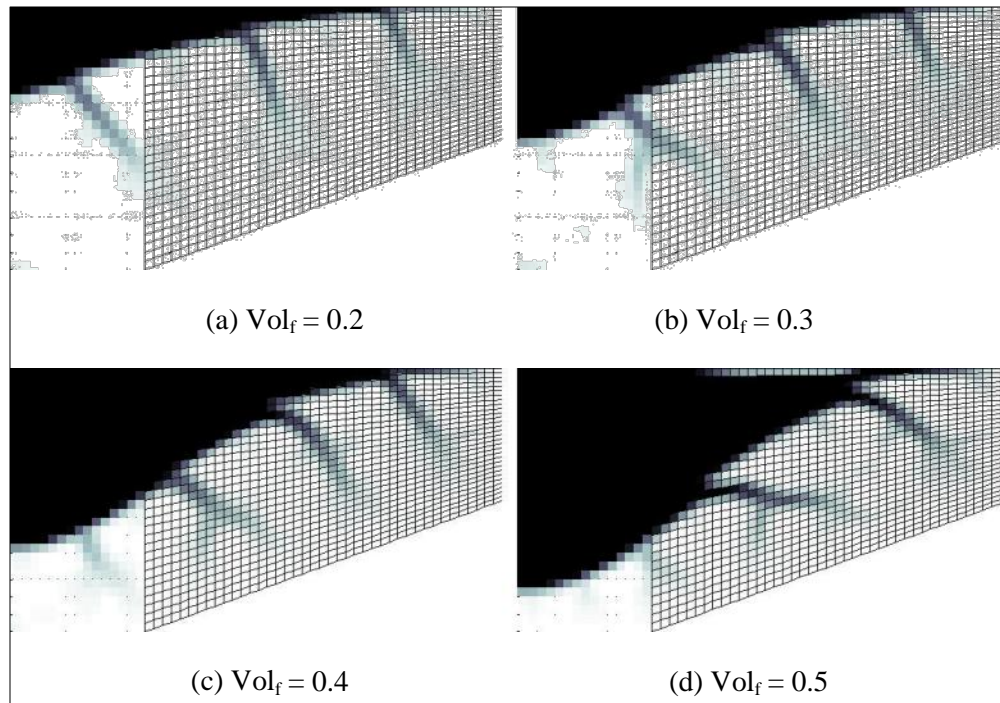


Figure 52: Bending Structure for Birdwing at Point 3

When this happens, the cluster assumes the role of a hub, where separate chains of truss members revolve around the hub and are connected to the hub by “spokes”. The structure essentially forms a polar grid, and consequently little material is left to form battens. The fact that both the induced drag and viscous drag are at peak values accounts for greater membrane influence and dominance over bending.

The forward swept flaring configuration of the wing is shown in Figure 55 through Figure 57 for the final point in the perching maneuver. As mentioned in the previous section, the intent of Point 4 was to capture the high braking drag loads that ultimately deflect the wings out-of-plane, but the point was selected when only twenty percent of the velocity remained. Therefore the drag that should have produced a highly bending-dominated structure was lacking, and instead, the selected Point 4 is actually the only point where the axial forces (in this case, due to lift) exceed the normal body forces.

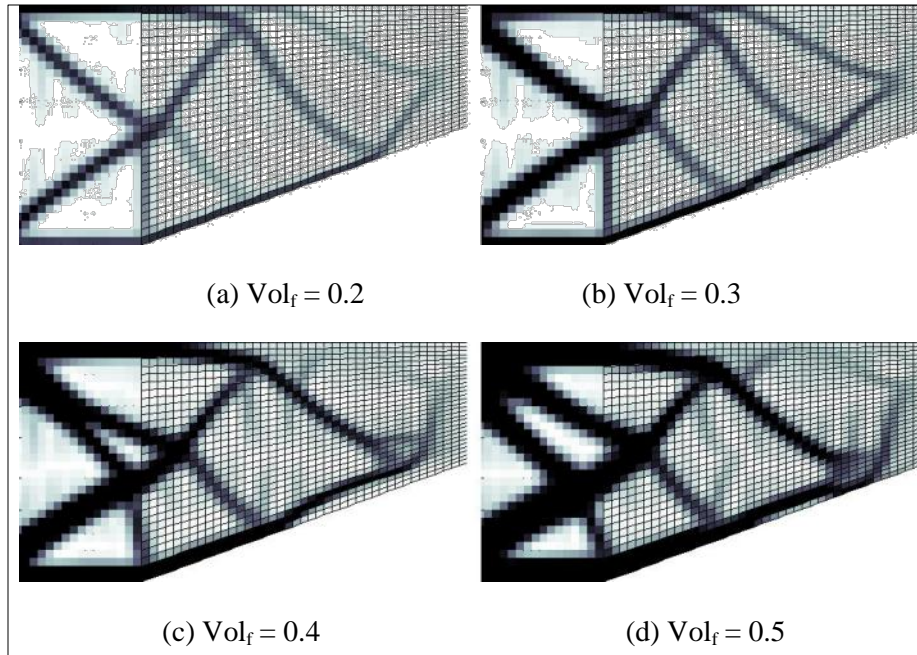


Figure 53: Combined Structure for Birdwing at Point 3

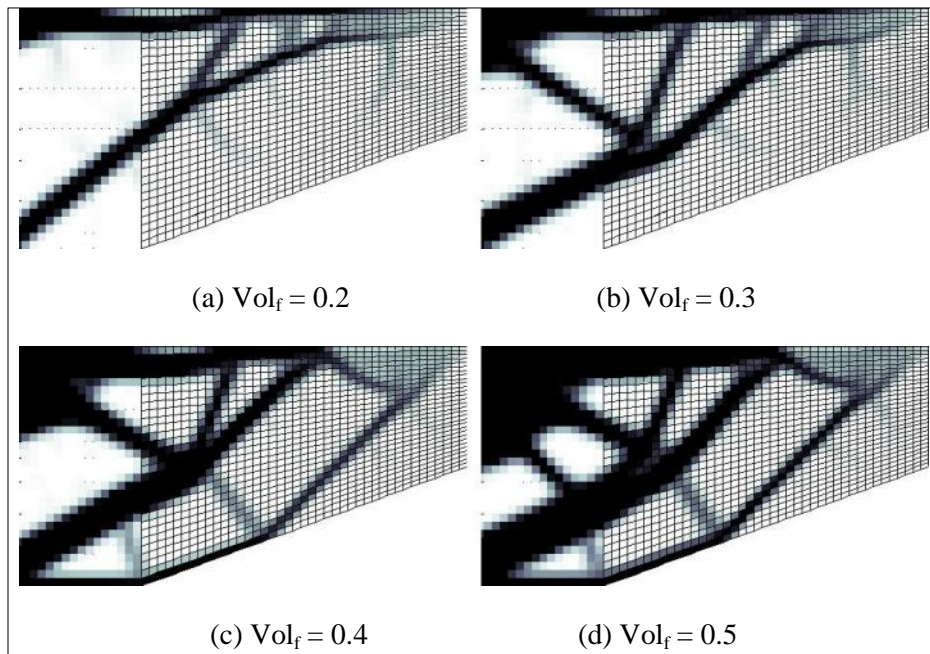


Figure 54: Combined Structure for Birdwing at Point 3 without Viscous Drag

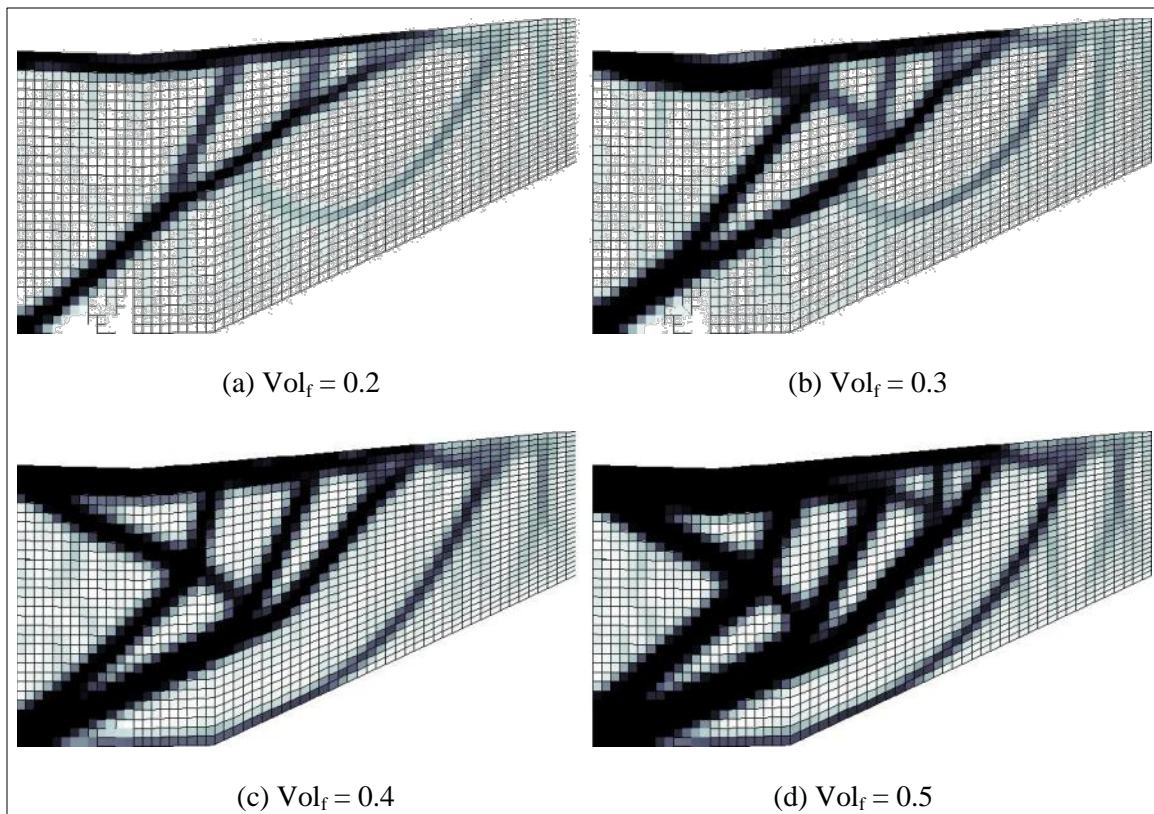


Figure 55: Membrane Structure for Birdwing at Point 4

In the membrane solution at Point 4, the fundamental wishbone structure, while not completely absent, does not best describe the layout. Rather, three main fingers (for volume fractions of 0.4 and 0.5) and one thinner finger emanating from the trailing edge support the leading edge. The three fingers have the appearance of three arms branching out on a candelabra. They could alternatively be likened to the three fingers found in bat wings. Many battens are again present. Additionally, some intermediate thicknesses are hung like tinsel, covering the bottom half of the wing, in the twenty and thirty percent volume fractions.

The bending topologies do not present any new features and are very similar to those occurring at Point 1 and Point 3.

In the absence of significant drag loading, the combined structure is completely membrane-dominated. The combined structure is again virtually indistinguishable from the membrane case, and thus the combined structure with no viscous drag is shown in Figure 57. In the absence of viscous drag, a slightly different membrane structure emerges. Though there is no “hub” resulting from a beam, the members are again arranged in the fashion of a web. This is fundamentally distinct from a typical truss structure which uses the inherent stiffness in triangulation. The solution is very clean and virtually no battens or stiffeners are present.

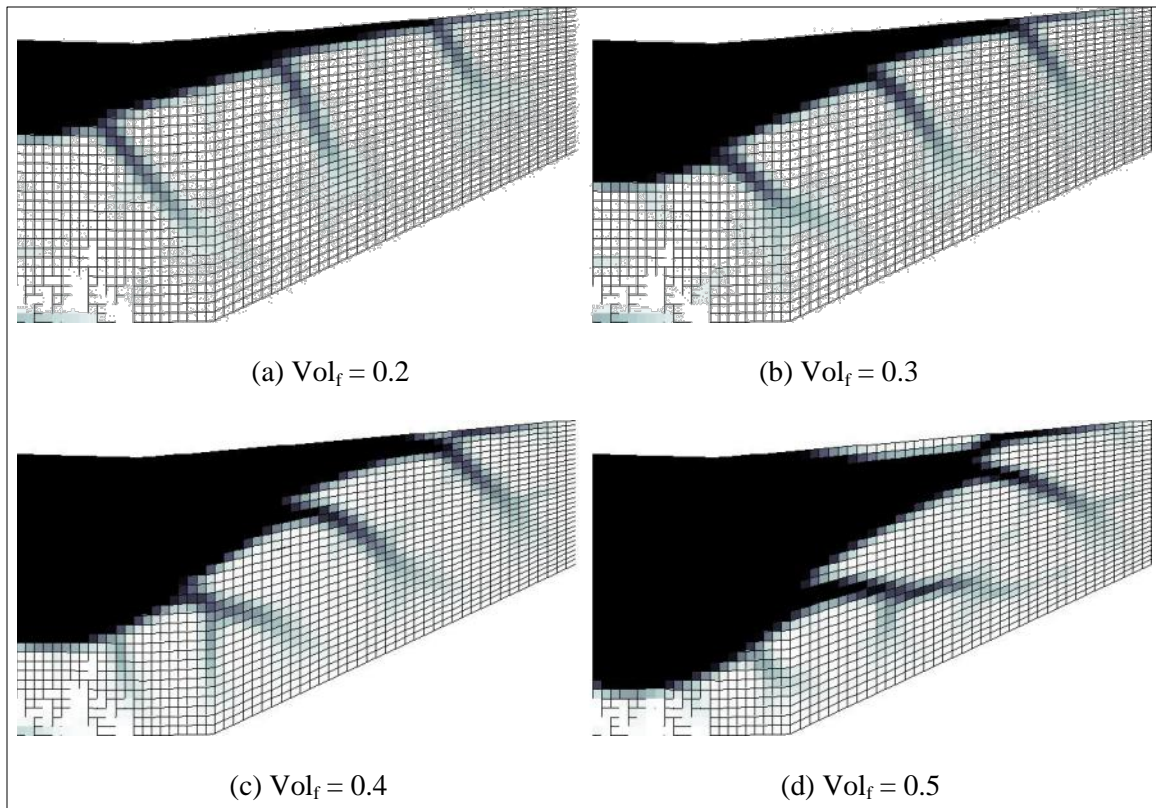


Figure 56: Bending Structure for Birdwing at Point 4

In this section, both the structural layout due to membrane loads and bending loads were studied independently, such that in the actual combined loading, one could identify whether the structure assumed an arrangement in the membrane or bending fashion. The bending loads can produce significantly more stress in a structure than membrane loads of the same magnitude. Yet, the combined loading optimization continually yielded membrane layouts.

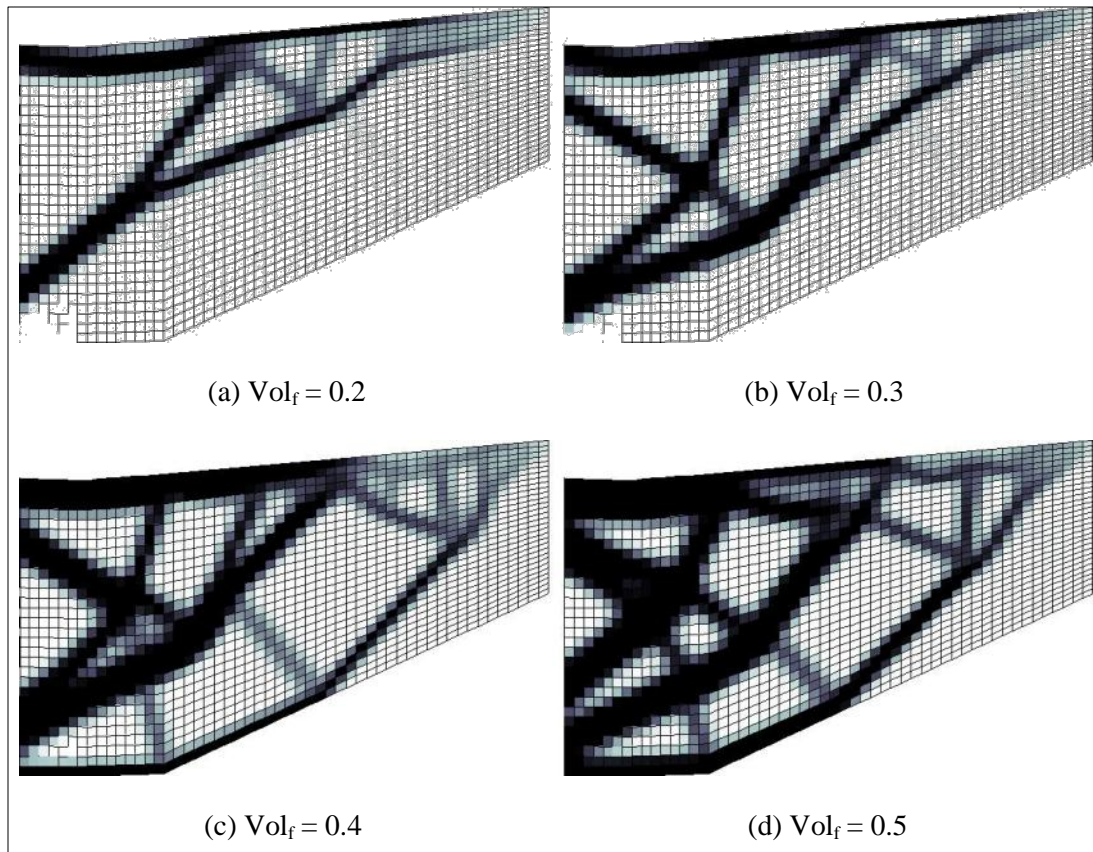


Figure 57: Combined Structure for Birdwing at Point 4 without Viscous Drag

When the viscous drag was removed, the effect was a structure that was a hybrid between the truss-like membrane structures and the beam-like bending structures. Thus, the viscous drag forces drove the solutions. Of course, the normal loads are still supported, albeit they were greater in magnitude than the axial loads. So the implication is that the membrane structure with discrete elements is also adequate to support out-of-plane loads. Thus the discrete members function like spars in resisting bending, but, rather than being arranged parallel to the leading edge and evenly spaced, they are aligned in a manner that also resists in-plane stretching. The implication of using a structure with discrete members for wing design is that the mechanism designed to achieve a planform shape change should be suitable to support out-of-plane loads provided that the members have bending stiffness. In this case, the actual layout of the members would be determined by a mechanism design and not by compliance minimization. However, if compliance minimization is used to suggest structural configurations, the general layout of Points 1 and 3 (which are very similar to each other) would probably be the best design point, since the MAV would spend the majority of its flight time in those configurations, and because these points experience the highest loads. Whether a shape-changing mechanism or a compliance minimization is used to design wing structure, the topologies explored here demonstrate that the leading edge must be predominately supported. Having a larger member extend across the leading edge may integrate well with a mechanism design where the leading edge is simply swept during a planform area change.

3.3 Grid Independence

In Section 1.2, it was mentioned that the discretization scheme for a distributed parameter system will affect the solution, and thus grid quality may be a concern. To briefly address this concern, a quick grid-independence study is undertaken here. In a first attempt, the mesh of the 0° sweep wing configuration was refined by a factor of 1.5 and then 1.25, but both refinements failed in Tornado. It may be that the corresponding cells were physically too small for successful computation by the vortex lattice method. However, a coarse 40 x 20 mesh was created and the compliance optimization was performed for the combined loading case without viscous drag, shown in Figure 54 for the 60 x 30 mesh. The results are shown in Figure 58.

For the twenty percent volume fraction, little to no difference is observed. The thirty percent volume fraction case produced the same basic layout, but the coarse mesh lacked one of the “spoke-like” members present in the finer mesh. In the forty percent volume fraction case, the entire outer radius of truss members is missing, and is not present until the fifty percent volume fraction case. Though the overall layouts are of the same essence, a finer mesh allows material to divide into smaller members, which is a similar effect as simply increasing the volume fraction. Convergence data is also provided in Figure 59.

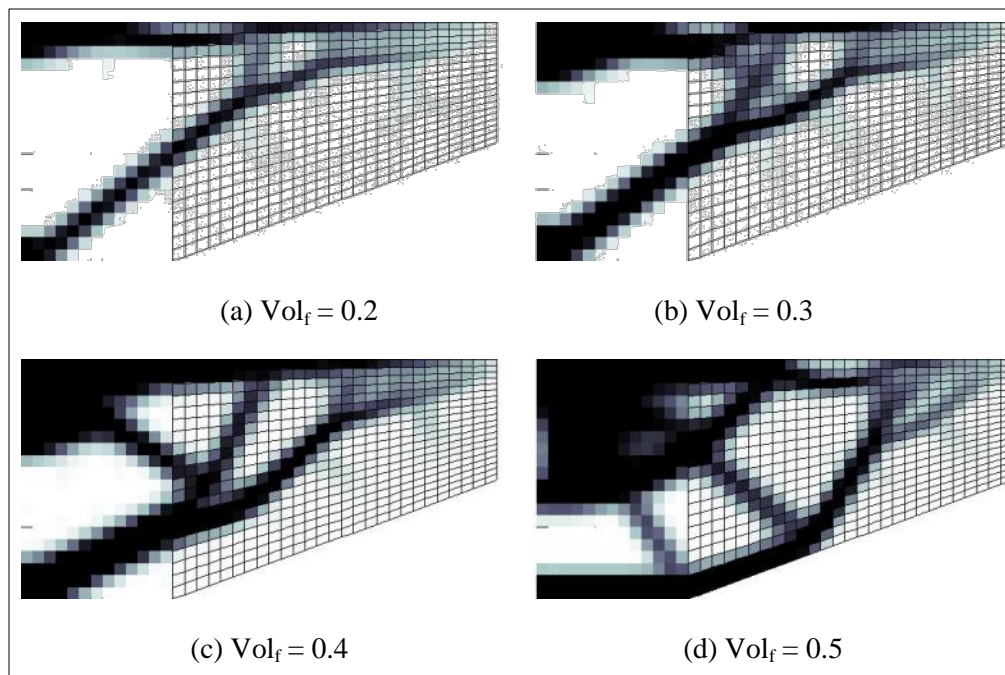


Figure 58: Combined Structure for Birdwing at Point 3 with Coarse Mesh

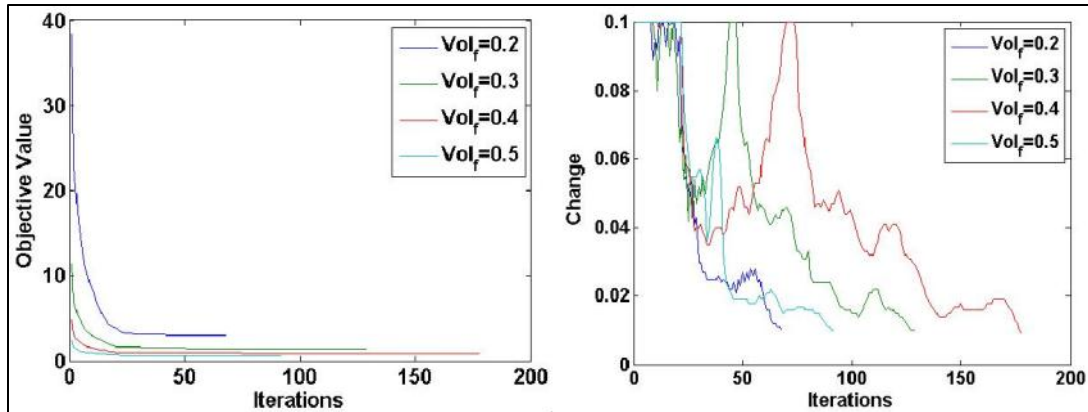


Figure 59: Convergence Data for Figure 58

3.4 Optimized Actuation System

Figure 60 presents results of a wing that morphs into two different configurations while minimizing the amount of actuation required. It is important to note that the membrane element was not yet implemented. This explains the perceived disconnect in some of the load paths. Notice how the optimizer develops the main spar along the leading edge to support most of the load and then places various revolute joints and telescoping members to provide the shape change actuation. In Figure 60 the red members denote a “pull” actuator whereas the blue members denote a “push actuator.”

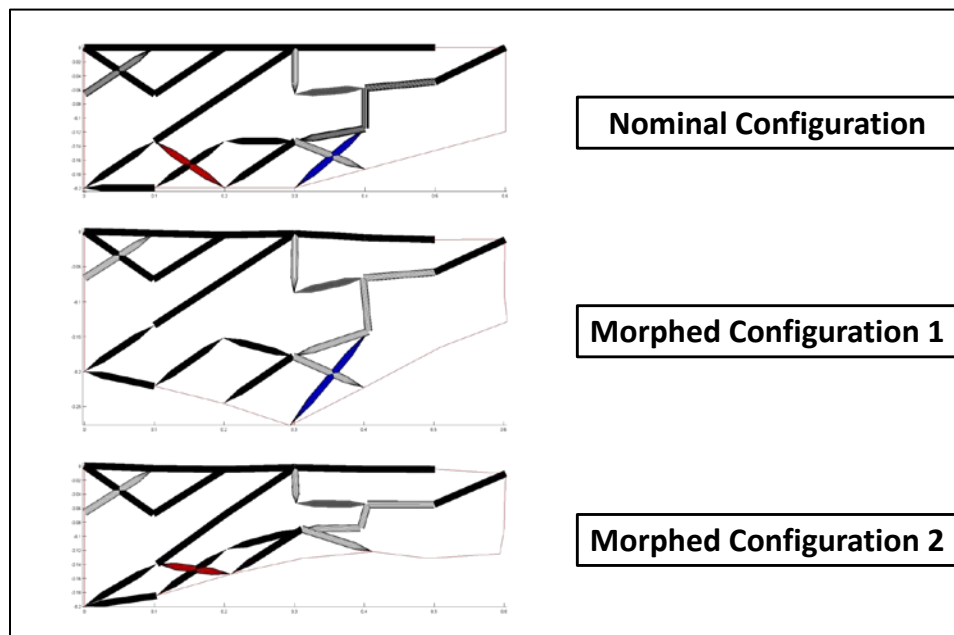


Figure 60: Results without Membrane Elements

Figure 61 presents results with the membrane element added. Notice the increase in structure to support the internal resistance of the pre-strained membrane. Also the optimizer designs scissoring mechanisms to achieve the desired morphed shape.

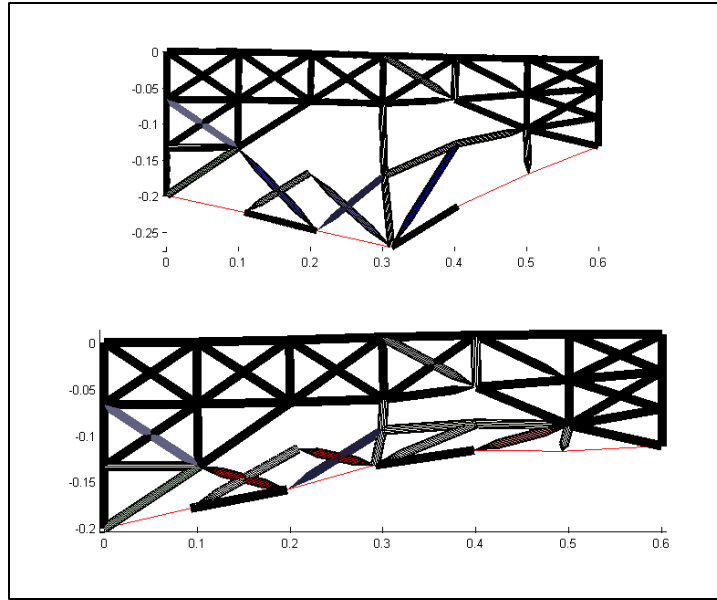


Figure 61: Results with Membrane Elements

Section 4. CONCLUSIONS

4.1 Summary

In 2003, DARPA began the MAS program with the aim of developing morphing aircraft structures that can substantially change shape to adapt to changing mission environments. Morphing wings with planform capabilities of telescoping, chord extension, and variable sweep will enable a multi-role platform far superior to both that of conventional fixed-wing aircraft, and even to aircraft with the capacity to modify their airfoil shape. Achieving radical shape change will require design that integrates innovative technology, including advanced flexible skin materials, efficient actuators and power systems, and mechanisms and structures with the facility to execute shape change.

Because morphing wing design is a multidisciplinary challenge, new design methods and processes must be synthesized that consider the holistic problem. The developing field of topology optimization promises to be an effective tool that can simultaneously optimize the arrangement and connectivity of the load-bearing structure, target shape-matching mechanism, and flexible skin elements, for any number of design objectives. Therefore, two objectives were established to advance previous efforts. The first objective was to develop a six degree-of-freedom finite element model comprised of continuous elements. This model would then be capable of supporting out-of-plane loading and could be used to represent the flexible skin of the wing. It was important to implement the model in MATLAB to be able to easily integrate it with optimization routines. The second objective was to consider realistic aerodynamic loading that MAV wings might experience through a changing mission environment. The perching maneuver common to birds was selected as an interesting miniature of a multi-role mission in which a bird undergoes several planform transformations.

By constructing a compliance minimization optimization objective (equivalent to a stiffness maximization objective), conceptual wing structure layouts of a MAV at various points throughout a perching maneuver were investigated. Both the structure corresponding to the isolated cases of membrane and bending loading, as well as the combined loading, was optimized. The results revealed some distinctive features of wing structure when only membrane loads or when only bending loads were considered. The structures formed by membrane loads were comprised of many discrete truss-like members that generally supported the leading edge of the wing. Rather than predominantly relying on triangulation for inherent strength, the members were typically arranged in cobweb formations with quadrilateral voids. Straight rods or battens protruded from the truss members pointing towards the center of a voided region or towards the outskirts of the wing. Contrary to the membrane structures, the bending loads elicited a principal beam-like structure situated anywhere between the leading edge and the quarter-chord, and extending from the root chord to the tip of the wing. With additional material, the shape of the beam evolved into a wishbone or delta conglomeration. Contrary to the battens that formed in the membrane case, chutes with endings that branched in arbitrary directions emanated from the central beam. These chutes act like stiffeners similar to the neural structures found in the flat wings of insects. The full three-dimensional loading typically favored the membrane structural formation over that of the bending. However, in the absence of the viscous drag distributed over the surface of the wing, a structure formed that is a hybrid of the typical membrane and bending structures. Thus the truss-like structure corresponding to the combined loading is thought to be driven by the distributed viscous forces. However, the discrete members must also behave

like spars that can resist the bending loads, which ultimately contribute the most to the total magnitude of the forces on the wing.

4.2 Recommendations

Though the resulting structures studied in Section 3 revealed distinctive features that parallel many formations with inherent strength found in nature, the methodology developed in Section 2 can certainly undergo improvements. First of all, the discretization scheme of the geometry for the finite element model was chosen to be structured meshing. Though the structured mesh was much easier to implement and also allowed a common mesh to be used for both the finite element method and the aerodynamic vortex lattice method, an unstructured mesh is more versatile in accurately modeling complex geometries. The inability of the structured mesh to model highly non-rectangular geometries was observed with the dive configuration, and merits greater consideration of using an unstructured mesh. However, if an unstructured mesh is to be employed, the advantage of easily discretizing a geometry with triangles is lost, since the element geometries derived were quadrilaterals.

The finite element itself could, of course, be selected differently. For example, rather than using Kirchhoff plate theory, Mindlin-Reissner plate theory could be used to couple the in-plane and out-of-plane effects. This would result in a five degree-of-freedom element that would avoid the need for superimposing two separate membranes and bending elements together. Such an element should also avoid the small displacement assumption of the combined membrane-bending element. Also, higher-order, nonlinear shape functions could be used, rather than the simple bilinear shape functions used here. Higher-order shape functions should increase the accuracy of the finite element model, particularly for cambered geometry.

The MATLAB implementations were very simple and the routines ran very efficiently. Both the membrane and bending models were validated with classical solutions, and their accuracy was verified. The superimposed membrane and bending element, while not validated with an analytical solution, did match the individual solutions of the membrane and bending models. The three dimensional six degree-of-freedom model, however, still lacks validation and successful integration with the SIMP model of the compliance optimization. If a full three dimensional analysis is not easily obtainable for comparison and validation of the model, the three dimensional FE model can be validated with a commercial finite element code, such as NASTRAN.

The aerodynamic force estimations can afford much improvement, though the extent to which improvement would influence the optimized thickness distributions may not be substantial. Effort should be spent to ensure that the outputted forces from Tornado do in fact act through the centroid of each panel. Post-stall aerodynamic models can also be employed to improve the aerodynamic calculations at the end of the maneuver. Also, a more ideal selection of Point 4 in the perching maneuver would capture the high angle of attack, and high angle-of-attack and pitch rates, while the aircraft still has most of its velocity. This should in turn capture the high bending loads that the drag exerts on the aircraft as it begins to slow down into a vertical landing.

In general, the Optimality Criteria method performed very efficiently, usually completing a minimization in less than five minutes with a couple seconds at most between iterations. The Method of Moving Asymptotes (MMA) is often employed for large scale optimization problems and may reduce

computation time. If larger problems are undertaken, such as would be produced from mesh refinement, the MMA solver may be worthy of investigation. However, for the problem sizes explored in Section 3, the OC method executed very well.

4.3 Future Work

With the insight gleaned from structural layouts, some experimentation is probably in order to test the stiffness of the structures. For instance, a study could be done to determine how much rigidity battens add to a structure in two-dimensional stress, or how much rigidity veins or branches add to a beam undergoing bending stress. Also, the inherent strength of a wishbone structure to resist being spread apart could be explored. A final pattern observed in the results had a layout similar to a cobweb. To aid the investigation, these structural formations could be more directly correlated to the wings of birds and insects.

LIST OF ACRONYMS, ABBRECIATIONS, AND SYMBOLS

AFRL	Air Force Research Laboratory
AIC	Aerodynamic Influence Coefficient
DARPA	Defense Advanced Research Projects Agency
DOF	Degree of Freedom
FE	Finite Element
GUI	Graphical User Interface
KKT	Karush-Kuhn Tucker
MAS	Morphing Aircraft Structure
MAV	Micro Air Vehicle
MMA	Method of Moving Asymptotes
OC	Optimality Criteria
SIMP	Solid Isotropic Material with Penalization
SMP	Shape Memory Polymer
UAV	Unmanned Aerial Vehicle
VLM	Vortex Lattice Method

Section 5. REFERENCES

- [1] J. Wilson, "Morphing UAVs change the shape of warfare," *Aerospace America - American Institute of Aeronautics and Astronautics*, vol. 29, 2004.
- [2] January 2012. [Online]. Available: <http://chrismillerfalconry.weebly.com/>.
- [3] January 2012. [Online]. Available: http://kevwlewis.deviantart.com/art/Eagle_Owl-Flyby-148980524.
- [4] January 2012. [Online]. Available: <http://albertan1956.blogspot.com/2011/08/owl-rescue-stops-traffic-in-germany.html>.
- [5] S. P. Joshi, Z. Tidwell, W. A. Crossley and S. Ramakrishnan, "Comparison of Morphing Wing Strategies Based Upon Aircraft Performance Impacts," in *52nd AIAA/ASME/ASCE/AHS/ASC Structures, Structural Dynamics, and Materials Conference*, 2004.
- [6] L. Maryann and R. K. Ackerman, "The Shape of Wings to Come," Armed Forces Communications and Electronics Association, 2006.
- [7] J. R. Elgersma, "Conceptual Layout of Wing Structure Using Topology Optimization for Morphing Micro Air Vehicles in a Perching Maneuver," Air Force Institute of Technology, Dayton, OH, 2012.
- [8] J. Joo, G. W. Reich and J. T. Westfall, "Flexible Skin Design for Morphing Aircraft Applications via Topology Optimization," *Journal of Intelligent Material Systems and Structures*, vol. 20, pp. 1969-1985, 2009.
- [9] J. J. Joo and B. Sanders, "Simultaneous Structure and Mechanism Design for an Adaptive Wing Using Topology Optimization," in *ASME International Mechanical Engineering Congress and Exposition*, 2005.
- [10] D. Inoyama, B. P. Sanders and J. J. Joo, "Conceptual Design and Multidisciplinary Optimization of In-plane Morphing Wing Structures," *Smart Structures and Materials: Modeling, Signal Processing, and Control*, vol. 6166, pp. 1-11, 2006.
- [11] D. Inoyama, B. P. Sanders and J. J. Joo, "Topology Synthesis of Distributed Actuation Systems for Morphing Wing Structures," *Journal of Aircraft*, vol. 44, pp. 1205-1213, 2007.
- [12] D. Inoyama, B. P. Sanders and J. J. Joo, "Topology Optimization Approach for the Determination of the Multiple-Configuration Morphing Wing Structure," *Journal of Aircraft*, vol. 45, no. 6, pp. 1853-1862, 2008.
- [13] D. L. Logan, *A First Course in the Finite Element Method*, 4th Edition, 2007.

- [14] B. G. Thomas and R. L. Finney, *Calculus and Analytic Geometry*, Addison-Wesley, 1984.
- [15] R. D. Cook, D. S. Malkus and M. E. Plesha, *Concepts and Applications of Finite Element Analysis*, John Wiley & Sons, 1989.
- [16] S. S. Rao, *The Finite Element Method in Engineering*, 4th Edition, Elsevier Butterworth-Heinemann, 2005.
- [17] Y. W. Kwon and H. Bang, *The Finite Element Method Using MATLAB*, 2nd Edition, CRC Mechanical Engineering Series, CRC Press, 2000.
- [18] J. M. Gere, *Mechanics of Materials*, 6th Edition, Thomson-Brooks/Cole, 2004.
- [19] R. L. Norton, *Machine Design: An Integrated Approach*, 3rd Edition, Pearson Prentice Hall, 2006.
- [20] D. K. Robertson, J. J. Joo and G. W. Reich, "Vortex Particle Aerodynamic Modeling of Perching Maneuvers with Micro Air Vehicles," in *51st AIAA/ASME/ASCE/AHS/ASC Structures, Structural Dynamics, and Materials Conference*, 2010.
- [21] T. Melin, "Tornado: A Vortex Lattice Program for Conceptual Aircraft Design, version 135, released March 20, 2010".
- [22] T. Melin, "A Vortex Lattice MATLAB Implementation for Linear Aerodynamic Wing Applications," Royal Institute of Technology (KTH), 2000.
- [23] M. P. Bendsoe and S. O, *Topology Optimization: Theory Methods and Applications*, 2nd Edition, Springer, 2004.
- [24] P. W. Christensen and A. Klarbring, *An Introduction to Structural Optimization*, vol. 153 of *Solid Mechanics and Its Applications*, Springer, 2010.
- [25] J. S. Aurora, *Introduction to Optimum Design*, 2nd Edition, Elsevier Academic Press, 2004.
- [26] K. Svanberg, "The Method of Moving Asymptotes - A New Method for Structural Optimization," *International Journal for Numerical Methods in Engineering*, vol. 24, pp. 359-373, 1987.
- [27] W. McGuire, R. H. Gallagher and R. D. Ziemian, *Matrix Structural Analysis*, New York: Wiley, 2000.
- [28] J. Katz and A. Plotkin, *Low Speed Aerodynamics*, Cambridge, UK: Cambridge UP, 2001.